Hydrodynamic Modelling of Port Foster (Deception Island, Antarctica)

Implementation of a two-dimensional tidal model and an approach on the three-dimensional model as well as generation of internal waves

Daniel Martins Figueiredo

Thesis to obtain the Master of Science Degree in

Engenharia do Ambiente

Supervisors: Prof. Dr. Aires José Pinto dos Santos and Prof. Dr. Marcos Duarte Mateus

Examination Committee

Chairperson: Professor Doutor Ramiro Joaquim de Jesus Neves

Supervisor: Professor Doutor Aires José Pinto dos Santos

Members of the Committee: Doutor Luís Quaresma dos Santos

October 2015

Abstract

In recent years the Antarctic continent has been the place of many different studies and findings, not only for its study potential but also for its conservation. Ongoing studies by Portuguese colleagues concluded that mercury concentration is rising in Deception Island, Antarctic Peninsula. One of the main problems they faced was not knowing how it would disperse inside the island, therefore giving rise to this research.

The island, where research in its bay hydrodynamics is scarce, has a semi-enclosed basin, presence of hydrothermal activity and sudden variations in topography.

Using a numerical hydrological model named MOHID, a validated tidal model was achieved and an approach to the three-dimensional model was started. Water level variations, tidal circulation and residence time were also obtained. The study of the effect of stratification in the water column for both seasons (winter and summer) was performed. The recognition of internal tides generation in summer and winter was achieved and the tidal components related to it were obtained. Using lagrangean tracers, the particles circulation was depicted and the main areas of accumulation were found.

The scarcity of radiation data and the unreliability of wind data were a big challenge to this work since they both have a significant impact in the water column. For future works that involve predictions, and not only the studies of processes, such data is essential in 3D model simulations. It is recognized that the results of the 3D model are associated with a non-negligible uncertainty that can only be reduced with an ongoing commitment to monitoring.

In this study, out of many findings, it is proved that Port Foster (Deception Island's bay) is a propitious place for mercury accumulation, therefore being a rising threat to the local ecosystem, as concentrations only tend to increase.

Keywords:

Antarctica; deception island; hydrodynamic modelling; stratification; internal waves; mercury.

Resumo

Nos últimos anos o continente antártico tem sido lugar de muitos estudos, não só pelo seu potencial, mas também com vista à sua conservação. Estudos efectuados por colegas portugueses levaram à conclusão que a concentração de mercúrio está a aumentar na Ilha Deception, localizada na Península Antártica. Um dos principais problemas que enfrentaram era o facto de não saberem como é que o metal se dispersava no interior da ilha, dando, por isso, origem a este estudo.

A ilha, na qual poucos são os estudos de hidrodinâmica publicados, apresenta uma bacia semi-fechada, presença de atividade hidrotermal e variações bruscas de topografia.

Usando um modelo numérico hidrodinâmico denominado MOHID, a validação do modelo de maré foi feita e uma aproximação ao modelo tridimensional foi iniciada. Variações do nível da água, a circulação das correntes de maré e o tempo de residência foram obtidos. O estudo do efeito da estratificação na coluna de água para ambas as estações do ano (inverno e verão) foi realizado. Confirmou-se a geração de marés internas no verão e inverno e obtiveram-se as componentes de maré relacionadas com a sua geração. Fazendo uso de traçadores lagrangeanos, conseguiu-se simular a circulação das partículas e as principais zonas de acumulação.

A escassez de dados de radiação e falta de fiabilidade dos dados de vento foram um grande desafio para este trabalho uma vez que ambos têm um impacto significativo na coluna de água. Para trabalhos futuros que envolvam previsões e não apenas estudos de processos, estes dois factores são essenciais na modelação hidrodinâmica. Reconhece-se que os resultados do modelo 3D estão associados a uma incerteza não negligenciável, a qual pode ser reduzida com um compromisso contínuo de monitorização.

Neste estudo, provou-se que Port Foster (baía da Ilha Deception) é um bom lugar para a acumulação de mercúrio, sendo este metal uma ameaça crescente para o ecossistema local, uma vez que tende a aumentar a sua concentração.

Palavras-Chave:

Antártida; ilha da decepção; modelação hidrodinâmica; estratificação; ondas Internas; mercúrio.

Agradecimentos

No decorrer deste trabalho, destacam-se muitas pessoas que, de uma forma ou de outra, contribuíram para a sua concretização e às quais gostaria de agradecer.

Em primeiro lugar, estou profundamente agradecido ao Prof. Dr. Aires dos Santos, pela orientação prestada, pelos ensinamentos, pela exigência e acima de tudo pela sua disponibilidade desde o início do desenvolvimento da dissertação. Quero agradecer ao meu coorientador, Prof. Dr. Marcos Mateus, pela ajuda prestada nas dúvidas que iam surgindo relacionadas com a implementação do modelo, bem como a sua boa disposição quando eu trabalhava no gabinete.

Agradeço ao professor João Canário as dúvidas tiradas relacionadas com a área da química, bem como material fornecido durante o decorrer deste estudo.

Quero agradecer também à Lígia, ao Guilherme e ao João da MARETEC – Instituto Superior Técnico, pela disponibilidade e pela ajuda prestada, que por vezes foi vital para a implementação do modelo.

A todos os meus amigos pelo apoio e boa disposição que me deram ao longo deste trabalho, bem como o reconhecimento da minha falta de tempo. À Sandra, pelas reuniões semanais, que trouxeram um grande sentido de responsabilidade e foram um factor relevante no desenvolver da dissertação.

Quero agradecer à minha namorada o apoio, carinho e incentivo que ela me deu no decorrer deste processo, que sempre me deu motivos para sorrir, erguer a cabeça e continuar.

Finalmente, aos meus pais e ao meu irmão, pelo apoio em todos os níveis, e pelos incentivos e motivação constantes durante a concretização deste trabalho, e ao longo dos últimos cinco anos.

Este trabalho foi indirectamente motivado pela iniciativa coordenada do Programa Polar Português. Agradeço também ao Comité Polar Espanhol o apoio a projectos que contribuiram com informação para o desenvolvimento deste estudo.

A participação neste projecto foi um verdadeiro privilégio.

Table of Contents

Index of Figures

Index of Tables

Annex

List of Abbreviations

4K1	Forth-diurnal component
MOHID	Hydrodynamic model
Q1	Large lunar elliptic diurnal
N2	Larger lunar elliptic semidiurnal
MSqm	Long period tidal component
K1	Lunar diurnal
O1	Lunar diurnal
2N2	Lunar elliptical semidiurnal
Mf	Lunisolar fortnightly
Mm	Lunar monthly
Mtm	Lunar third-monthly
K2	Lunisolar semidiurnal
NOAA	National Oceanic and Atmospheric Administration
NE	Northeast
NW	Northwest
M2	Principal lunar semidiurnal
S2	Principal solar semidiurnal
M4	Shallow water overtides of principal lunar
P1	Solar diurnal
SW	Southwest
SK3	Third-diurnal component
3D	Three-dimensional
2D	Two-dimensional
W	West

List of Symbols

p_{atm}	Atmospheric Pressure
ρ_0	Reference Density
f	Coriolis frequency
ρ	Density
z	Vertical Coordinate
Ω	Earth’s rotational vector
η	Free Surface Level
k_H	Horizontal turbulent diffusivity
v_H	Horizontal turbulent viscosity
u	Horizontal Velocity in x
v	Horizontal Velocity in y
p	Pressure
φ	Property
S	Salinity
S_i	Sinks
S_0	Sources
T	Temperature
k_V	Vertical turbulent diffusivity
v_V	Vertical turbulent viscosity
w	Vertical Velocity in z

1. Introduction

1.1 Motivation

The subject for this thesis started off from the need of a hydrodynamic model capable of explaining how different elements, such as Hg and MeHg, would disperse in Port Foster, Deception Island, Antarctica. Deception has great interest for researchers, since it's located in Bransfield Strait, a region of deep water formation, where one can monitor it to study climate changes. The semi-enclosed nature of the basin, the presence of hydrothermal activity, the sudden variations in topography and the fact that is located in the most remote continent on Earth in a region with severe weather conditions, are some of the challenging features that make this study worthwhile.

1.2 Context

The paucity of taxa in Port Foster can be related with the existence of trace metals, and some concentrations of those metals, such as mercury, are 10 times bigger than those found in the Southern Atlantic Ocean. Little is known about mercury biogeochemistry in Antarctica, and an integrated study is needed, that takes into account the sources, fluxes, pathways and bioavailability of mercury in Port Foster's ecosystem. This work, made possible through a mathematical model named MOHID, will contribute to that study and also to a better understanding of the bay hydrodynamics.

1.3 Objectives

The ultimate goal is to have a three-dimensional baroclinic model that will help to understand the role of Port Foster's hydrodynamics on the dispersion of elements such as mercury, taking into account the role of tides, bathymetry, the stratification of the water column and the forcing due to the wind.
To achieve this goal, the following tasks must be performed:

- Define the islands Coastline;
- Create the bathymetry for the inside and the surroundings of the Island;
- Validate the barotropic model forced only with tides;
- Determine the residence time;
- Apply different temperature-salinity (T-S) profiles for Port Foster and the surrounding area;
- Study the seasonal impact of water stratification;
- Study the tidal influence in Port Foster water column mixing;
- Study the possibility of internal tides generation;
- Use Lagrangian Tracers to see the influence of tides in contaminants dispersion.

2. Literature Review

2.1 Description of Deception Island

2.1.1 Overview

Deception Island (lat. 62º57'S., long. 60º38'W) belongs to the archipelago of South Shetland Islands. It is located in Bransfield Strait (Galindo-Zaldívar et al. 1996; Gonzalez-Casado et al. 2000), which separates the cluster of Islands from Antarctic Peninsula (Baraldo et al. 2000) (Figure 1).

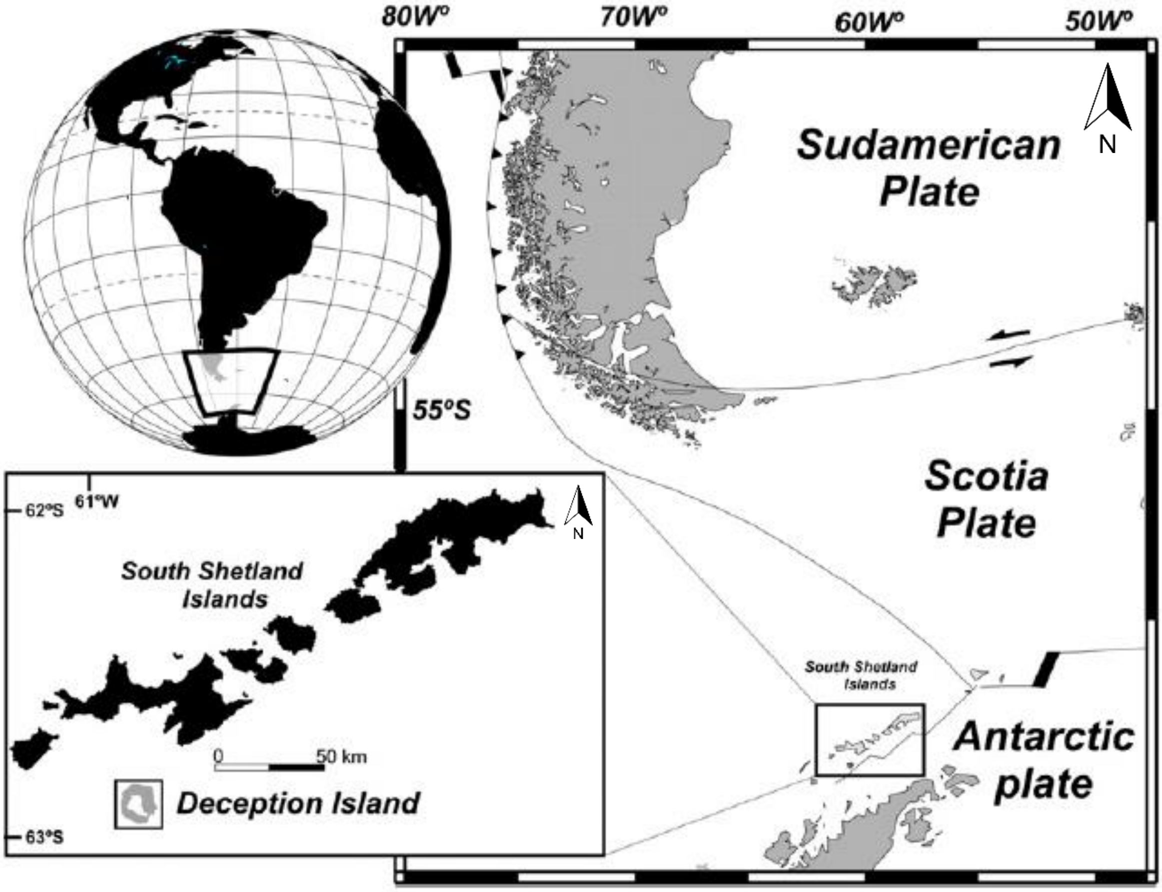

Figure 1 - Location of Deception Island (Pérez-López et al. 2007).

The Island, with a horseshoe-shaped morphology, is an active volcano, with approximately 12 km diameter and maximum altitude in Pond Mount (539 m) (Molina et al. 2013). It has an inner bay, called Port Foster, resulting from the collapse of a volcanic chimney, which allows access by the sea (Hawkes et al. 1961). Port Foster has an almost elliptical shape, with an approximate perimeter of 32 km and maximum mid-bay depth around 160 m (Pérez-López et al. 2007), being that the length and width are 9.8 e 5.7 km, respectively (Kaufmann et al., 2003; Smith et al., 2003b). The narrow connection existing between the bay and the sea is known as Neptune's Bellows, located southeast of the island, which presents minimum depths of 10 meters. More than half of the Island (around 57%) is covered by permanent glaciers, some with almost 100 meters height (López-Martínez & Serrano 2002). The ring of mountains that involve the bay is the island's main drainage system, occurring drainage to both inner and outer coasts (Mão de Ferro 2012). The inner coast consists mostly of sand, in contrast with the outer coast, which is mainly composed by rock gorges (J.L Smellie 2001). The island's climate is maritime polar and temperatures vary between – 28ºC and 11ºC, with an average annual temperature of -3ºC. The average annual rainfall is 500 mm and the prevailing winds are from the Northeast and Southwest. Due to hydrothermal activity, some places within the bay present an extreme microclimate, where water temperatures close to 70ºC were detected (Deception Island Management Package).

2.1.2 Human History

It was between 1772 and 1775, that James Cook circumnavigated the grounds in the Southern Ocean, reporting abundance of seals, therefore capturing the attention of the seal hunting communities. Intensified sealing throughout the years and the evolution of the industry may have led to the killing of more than one million fur seals, according to James Weddell's estimates. Around 1820 there were few seals left. The South Shetland Islands, where Deception Island is located, were discovered in 1819, and along with this discovery came more sealing. The first authenticated sighting of Deception Island was by the British sealers William Smith and Edward Bransfield from the brig *Williams* in January 1820 (Basberg and Headland 2008).

With this early 19th century hunting of Antarctic fur seals, Deception was the site of some of the earliest commercial activity. This Island was also the site of the only successful land based commercial activity in Antarctic history and by later part of the twentieth century had become a regular stop for the growing Antarctic tourist cruise industry, as well to many researchers of different areas of interest (Dibbern 2009).

Whaling was another strong activity starting around 1906-1907. The Hektor Whaling Company with factory in Whalers Bay, started business in 1912, contracting 150 people to work during the austral summer, producing over 140,000 barrels of whale oil. The remains of Hektor whaling station, an whalers cemetery (the largest cemetery in Antarctica) and Base B, partially destroyed by a volcanic eruption in 1969, are now protected as Antarctic Treaty Historic Site and Monument (HSM) Number 71 (Deception Island Management Package).

During the 1940's and 1950's, overlapping territorial claims of the Antarctic Peninsula region were upheld by Argentina, Chile and the UK, and were the source of political tension. Deception Island played a central and important role in the international affairs of Antarctica (Deception Island Management Package).

2.1.3 Volcanism

Deception Island is located between two major tectonic structures: the southwestern end of Bransfield Strait and the southern prolongation of the Hero Fracture (Rey et al. 1995). Some researchers suggest the bay was formed during a continuous process of expansion caused by the tectonic structures (Rey et al. 1995; Baraldo et al. 2000), however the more consensus theory is that the formation of the bay was a result of a catastrophic collapse and consequent submergence of the volcanic cone (Baker et al.1975). Deception Island is a volcano of the Quaternary age (less than 780 ka) (Valencio et al. 1979; Smellie 2002; Baraldo et al. 2003) and it shows the most recent active volcanism of the South Shetland Islands (Smellie 1988). The first historical eruption was in 1842, producing cinder cones and associated lava flows over a distance of 4km (Martí and Baraldo 1990). Following this eruption other historic eruptions occurred in 1912, 1917, 1967, 1969 and 1970, producing significant volumetric changes of the coastline (Torrecillas et al. 2012). In 1967 the eruption happened northwards the inner bay, close to Telefon Bay (Figure 2). This eruption, originated a small island (known as Yelcho or Marinero Suárez) and it also partially destroyed the Chilean Antarctic Station “Pedro Aguirre Cerdá”, already abandoned at the time (Clapperton, 1969). In 1969, one eruption arise east of the bay (Pendulum Cove) (Figure2), in a place that was covered by a glacier. This Strombolian eruption destroyed the British Antarctic Station “John Biscoe” in Whalers Bay, Southeast of the island (Roobol, 1982; Torrecillas et al. 2012). The eruption of 1970 happened in the same spot as 1967 (Vila et al. 1992). Currently, the volcanism in Deception is manifested through large hydrothermal activity, intense seismic activity, fumaroles and other abnormal thermal manifestations.

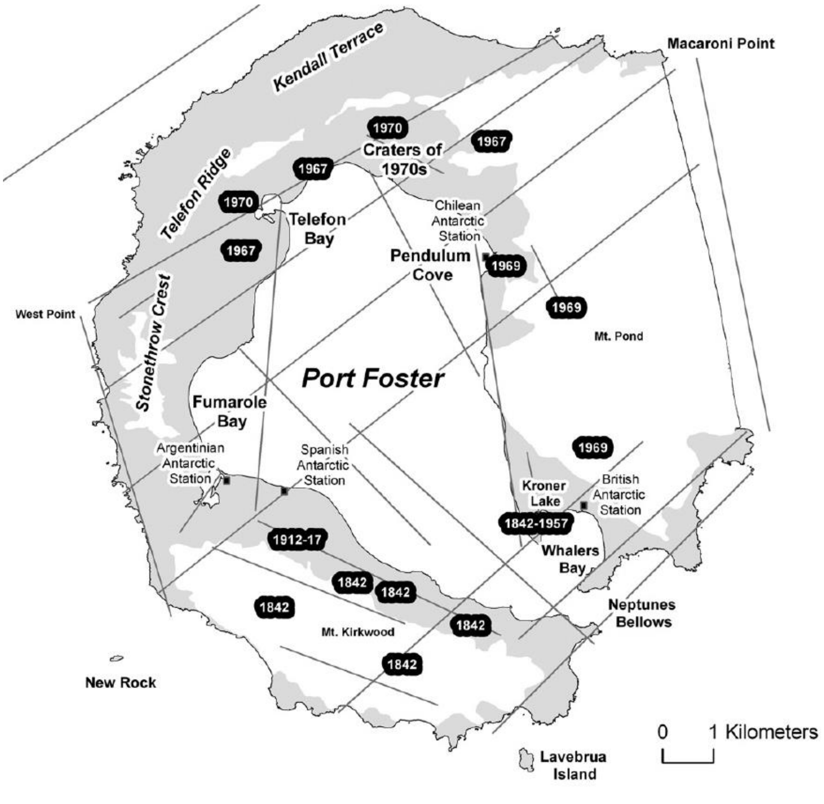

Figure 2 - Toponyms of research and historical eruption sites on Deception Island. Solid lines represent regional morphological lineations. (C. Torrecillas et al. / Geomorphology 136 (2012) 6–14).

2.1.4 Geology

The evolution of Deception through volcanic-tectonic dynamics makes the volcanic deposits in the Island to split in two major groups, both associated with the collapse of the caldera: the pre-caldera deposits and post-caldera deposits (Smellie 1988, 1989). The former consist mainly in lavas, pyroclastic rocks and mass flow deposits, while the later appear in early cone deposits, fissure-erupted strombolian scoria and lavas, late tuff and maar deposits.

Around the shores of Port Foster, plains of stream-deposited gravelly-sandy sediments are predominant and there are some ash-covered areas, mainly at steeper slopes (Smellie 2001). Permafrost is present at low elevations, with typical depths of 60-96 cm to the top of the frozen layer (Smellie et al. 1997). The more abundant volcanic products are basic and intermediary rocks, with a wide compositional range, varying from basalt to dacite, but basalts and basaltic andesites are volumetrically dominant (Smellie 2001).

There are not many studies about seafloor composition or its topography, however “the uneven glacier surface at lower elevations suggests that the underlying bedrock topography is very rough, resembling a jumble of displaced large bedrock blocks.” (Cited by Smellie 2001). The caldera floor of Port Foster is covered with a layer of yellowish-brown volcanoclastic sandy mud composed primarily of basaltic-andesitic lithic fragments and volcanic glass. Minimum sediment accumulation rate was estimated to be at least 5 mm/yr. (Gray et al. 2003).

2.1.5 Biology and Chemistry

Both these study areas are addressed in this subchapter because they have a strong relation, therefore making sense to present them together.

Richness and abundance of species have increased at Deception Island with time since the 1969–1970 eruptions (Gallardo & Castillo 1968, 1970, Gallardo et al. 1975, 1977, Retamal et al. 1982, Arnaud et al. 1998, Cranmer et al. 2003, Lovell & Trego 2003), but on shorter time scales Cranmer et al. (2003) and Lovell & Trego (2003) found relatively little monthly or seasonal variability in species presence and abundance, meaning that although there is an increase in number of species, it is a gradual and slow increase. This small increase of taxa along time can be explained by different factors such as volcanism, current extreme sedimentation and temperature regimes, acidity, trace metals and rarity of three-dimensional structures provided by suspension feeding communities (Cranmer et al. 2003 recorded just a few sponges) (Barnes et al. 2008).

By estimates presented in Barnes et al. (2008), there is a minimum of 213 aquatic species found to date in Port Foster, being Neptune’s Bellows a place with a relatively rich community (Dayton 1990, Arntz et al. 1994, Barnes 2000). Barnes et al. 2008 also suggests a strong decline of species richness from Neptune’s Bellows into the caldera at subtidal depth.

Through the studies conducted so far on the Island an overview of the Biota can be summarized as follows: (i) the overall abundances of fishes observed in Port Foster shows maximum in November 1999 that range from 0.05 to 0.10 fish/m^2, similar to those found over a larger region and depth range in the Weddell Sea. (Ruhl et al. 2003); (ii) many of bird species are most likely visitors of Deception Island, using the protected areas of Port Foster as resting and foraging grounds along migratory routes within the Antarctic Peninsula region or from Antarctica to points north such as South America (Kendall et al. 2003); (iii) the population of one of the most common types of penguin specie's existing in Deception, Chinstrap penguins, has decreased 36% from 1991 to 2008 (Barbosa et al. 2012).

As mentioned in Barnes et al. (2008), one factor that can be related with the paucity of taxa, is the existence of trace metals. Enhanced biological availability of trace metals have been reported in the marine community (Ag, Se, Al, Fe, Mn, Sr, Ti and Zn) (Deheyn et al. 2005) and penguin feathers (Pb) (Jerez et al. 2011) collected in Deception Island, however the sources and transport processes of all those contaminants have not been deeply studied yet.
One problem for aquatic organisms is that the low adsorption capability of sediment increases the concentration of dissolved elements in solution, consequently being available to uptake (Mão de Ferro et al. 2013).

Concentration values for Cd in saline water samples collected in Port Foster were consistently high when compared with published values for the Southern Ocean. (Silvia Jerez et al. 2013; Mão de Ferro et al. 2013). Also high concentrations of Pb were detected in the nearby King George's Island (Lim et al. 2009) and Bargagli et al. (2000) argued that the biogeochemical cycle of Pb is probably the only one that has been significantly influenced by local and remote anthropogenic input. High concentrations of MeHg dissolved in the waters of Port Foster were detected (Mão de Ferro 2012).

The decrease in some populations and the abnormal presence of some concentrations of chemical elements creates a question: does any of these facts come from anthropogenic activities?
There's no consensus in the scientific community, several authors have studied soil samples, sediments, water and invertebrates in the proximity of scientific basis in Deception Island. Some of them have described an insignificant influence of human activities on the presence of environmental contamination (e.g. Ahn et al., 1996; Guerra et al., 2011), whereas others have proved a low to moderate anthropogenic influence (e.g. Bícego et al., 2009; Curtosi et al., 2007; Lu et al., 2012; Ribeiro et al., 2011; Santos et al., 2005; Silvia Jerez et al. 2013).

2.2 Deception Island Previous Studies

Some authors after the ERUPT program (March 1999 to November 2000) were the first developing a more deep ecosystem study about Deception Island, with a very detailed analysis of different variables. This series of studies were presented in Deep-Sea Research Part II: Topical Studies in

Oceanography, and had the contributions of Dr. Yueng-Djern Lenn*, Dr.* Kenneth L. Smith, Jr. and many others. The primary goal was to monitor the seasonal changes in the marine ecosystem within Port Foster using remote sensing instruments for continuous sampling combined with seasonal sampling on cruises. During ERUPT program a lot of data was collected, through different instruments such as: a meteorological Terrestrial Station; thermistor arrays; CTD/rosette and others (Glatts et al. 2003), which allowed a deeper understanding of the physical, chemical, biological and geological oceanography of Port Foster (Smith et al. 2003b).

The first observations of the sea levels at Deceptions Island were made in 1991 (Dragani et al. 2004). There are more recent studies (Vidal et al. 2010; Vidal et al. 2012; Jigena et al. 2014; Jigena-Antelo et al. 2015) that present important results related to the mean tidal level's in Port Foster, the total volume exchange during the flood and ebb tides, velocities of the most important harmonic components, as well as *insitu* observations.

More recently, in 2012, under the project INTERCEPTION, during the 31st Antarctica Operation of Proantar, a large meteo-oceanographic buoy was launched and docked in the bay of Port Foster. New studies on the interactions between the ocean, the coastal zone and the atmosphere in the region of Deception Island will benefit from the data collected by the new equipment of the National Institute for Space Research (INPE) (Santini et al. 2012). Analysis of other data collected during the expedition is presented in Coelho & Souza (2011).

Several studies regarding thermodynamic parameters and the use of WRF (Weather Research and Forecasting) Model in Deception Island were developed by the Brazilian research community, mainly from UFSM (Universidade Federal de Santa Maria) and INPE (Comin et al. 2012, Cardoso et al 2013.)

2.2.1 Tide

The tide is responsible for the variability of diurnal and semidiurnal currents. The most important tidal components are the M2 (0.0805 cph), K1 (0.0418 cph), O1 (0.0387 cph), S2 (0.0833 cph), with the M2 being the most relevant, with amplitude of 0.4 m, and the other components with amplitudes in the order of 0.28 m. The amplitudes of the velocities are very low (less than 5cm/s) within Port Foster, and the maximum tidal currents are observed in Neptune's Bellows, with speeds between 0.64 and 0.76 ms^{-1} and elevation around 3 meters during the period of spring tides (Lenn et al. 2003), being also the region where most of the tidal energy is dissipated (Vidal et al. 2011), since it changes from a barotropic regime to a baroclinic one. The mean tidal level is 1.2 m, which means that 1.10% of the total volume of Port Foster is swapped with the Bransfield Strait in each tidal cycle. For the case of spring tides, this amount is approximately 2.8% of the total volume (Vidal et al. 2011). Under ERUPT project Lenn et. al. (2003) appraised the current spectra (Figure 3) in site B (Figure 4) in the months of stratified water (Summer-Autumn) and well mixed water (Winter-Spring), confirming the importance of the tidal flow.

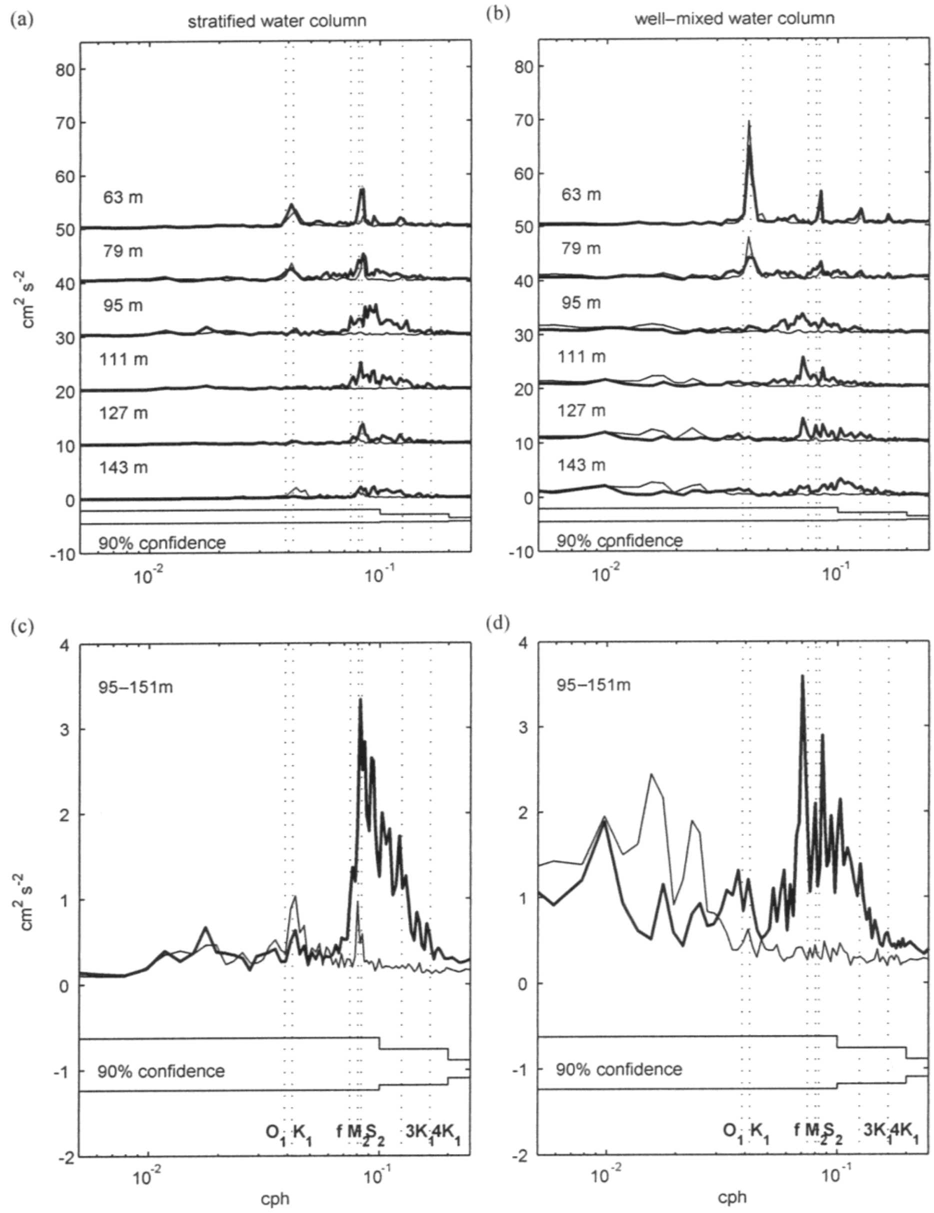

Figure 3 - Variance-preserving rotary spectra of currents at six depth bins when water temperature is stratified (a) and well-mixed (b); spectra for each depth shown are offset by 2 $cm^2\ s^{-2}$ and anti-clockwise spectra are plotted in bold, while clockwise spectra are plotted as thin lines. Average spectra for the bottom eight depth bins (95-151 m) for the same periods are shown in (c) and (d). Tidal frequencies for the O_1, K_1, M_2, S_2, third-diurnal ($3K_1$) and forth-diurnal (4K1) components are plotted as dotted lines. (Lenn et al. / Deep-Sea Res. II, 50, 1665-1684).

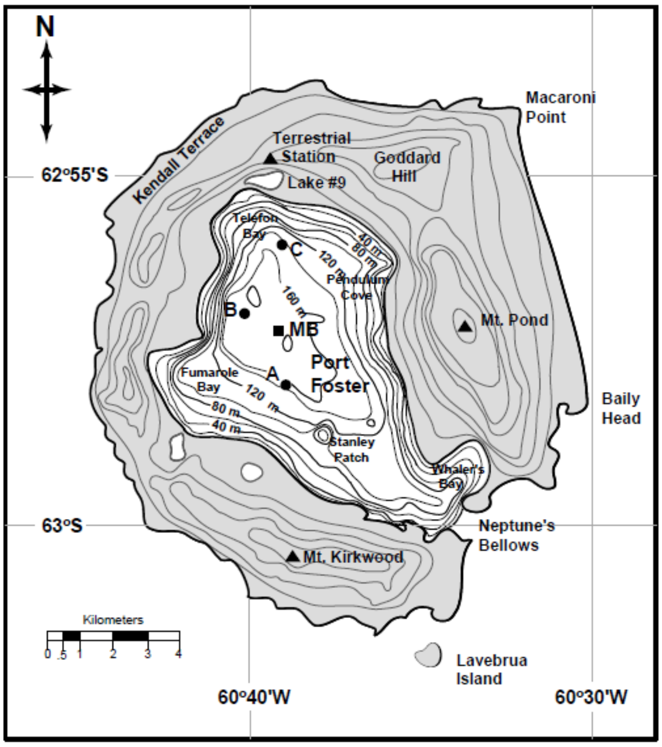

Figure 4 - Detailed map of Deception Island, adapted from Smith Jr. et al. (2003b). The thermistor moorings A, B and C are indicated with a circle; the mid-bay (MB) site for CTD casts is indicated by a rectangle (Lenn et al. / Deep-Sea Res. II, 50, 1667).

In the months of stratified waters, the counterclockwise circulation is much more intense than the clockwise one. For the former, a maximum energy in S2 frequency and minor surges in K1, 3K1 and 4K1 frequencies were observed**,** while for the clockwise circulation there are two equal intensity maximums, corresponding to K1 and M2 frequencies. During the months of well mixed water, the counterclockwise movement continues to be predominant, except in the region of low frequencies (values lower than 0.03 cph) where the flow is mainly driven by the wind. For counterclockwise circulation the influence of the tide is evident, with energy surges in K1, S2 and 3K1 frequencies.

2.2.2 Wind

According to Smith et al. (2003a) wind speeds measured in 1999, in the Terrestrial Station, are quite variable, with daily average values between $0.6\mathrm{ms}^{-1}$, on 18th of April, and $47.1\mathrm{ms}^{-1}$, on the 4th of June. During 2000, the values observed in the same location ranged from $0.2\mathrm{ms}^{-1}$, on the 18st of October, to 47.4 ms^{-1} on the 28st of June. The maximum speed achieved is not known but the measurement limit of the apparatus was reached (65 ms^{-1}). In general, the maximum velocities occur in June, with more frequent daily mean values between 4 and $10\mathrm{ms}^{-1}$, where the prevailing direction is SW, NE also being observed (Figure 5). Comparing the measured winds in Terrestrial Station and Bellingshausen Station (located next King George Island), it appears that in the first station, there is a bigger incidence of daily average wind's with speed equal to or less than 4 ms^{-1} and a lower incidence in the range from 6 to $10\mathrm{ms}^{-1}$, being the most frequent wind speeds above $10\mathrm{ms}^{-1}$.

Another important difference is the wind direction: W and NW predominant in Bellingshausen Station, instead of the NE and SW winds for the Terrestrial Station (Figure 5).

Comparing the location of the two stations, it appears that the Terrestrial Station is located in a region that substantially determines the wind direction. The Terrestrial Station is located at an altitude of 200 m, approximately equidistant between sea level and the top of a mountain whose rocky wall is oriented to the south. This mountain and the surrounding terrain, contribute to guiding the wind in the SW-NE direction, while the Bellingshausen station is located at an altitude of 16 m above sea level, in an open plain without orographic constraints. Comparing the histograms of these two stations with historical data from Whalers Bay (United Kingdom Hydrographic Office, 1944-1963), one concludes that the NW winds observed in Whalers Bay and Bellingshausen are similar in direction. However, NE winds at Whalers Bay are similar in direction to those measured in the Terrestrial Station, suggesting that the absence of NW winds in this station results from orographic constraints (Figure 5).

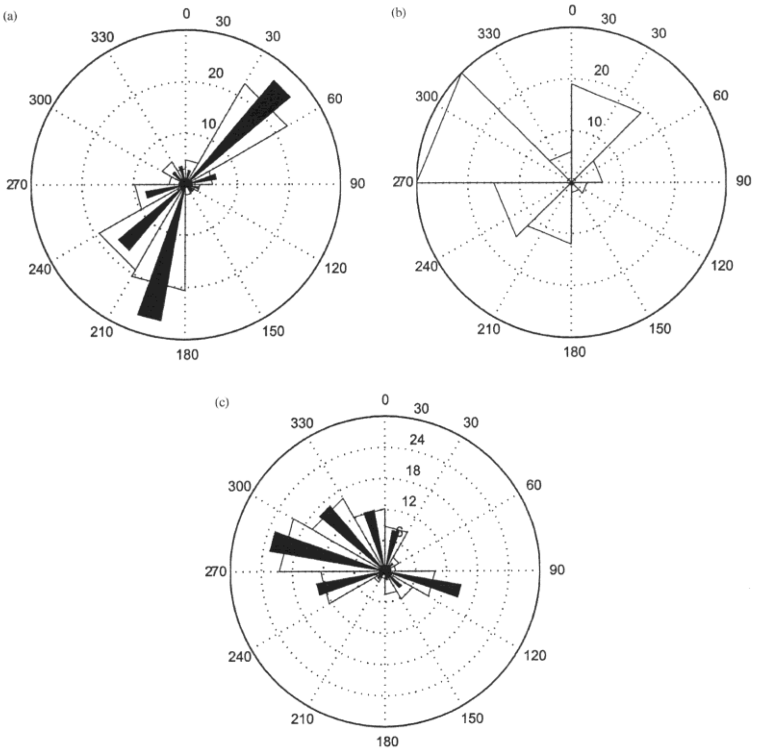

Figure 5 – Histograms of daily averaged wind speed and wind direction shown in degrees true as a wind rose (a) Deception Island Terrestrial station, (b) Deception Island, Whalers Bay historical data (UK, Hydrographic Office between 1944 and 1963), and (c) Bellingshausen Station. The radius of the outermost, open wedges is the relative frequency of each of the 12 directions for the Terrestrial station (a) and Bellingshausen (c) data, 8 directions for the historical Whalers Bay, Deception Island (b) data, normalized to percent. The inner filled wedges (a) and (c) are the percent frequency times the average wind speed in that direction, normalized to percent (wind speed was not available for the historical Whalers Bay, Deception Island data). The Bellingshausen Station time series was sampled for the 287 days when the Terrestrial station also measured wind velocity. Direction is in degrees true and is the position from which the wind blows. (Smith et al. / Deep-Sea Research II 50 (2003) 1649–1664).

More recently, Comin et al. (2012) presented one month results based in a Local WRF and a comparison with data of wind stress and wind direction collected by Almirante Maximiano Polar Ship in February 2011, however the data indicates that the predominant winds are NW and SE, confirming that the orography is a very big constrain in wind direction.

Unlike the tidal forcing that introduces diurnal and semidiurnal variability in the flow, forcing due to wind stress gives rise to seasonal variations. Returning to Figure 3d (Winter-Spring), in the region of low frequencies (values below 0.03 cph) there are energy surges corresponding to the wind forcing. The same figure shows a maximum near the inertial frequency, which is absent in the Summer-Autumn period (Figure 3c), when the wind is less intense. In the large time scale associated with the wind, average speeds are not zero, with values in the range 0.01 to $0.04\mathrm{ms}^{-1}$.

2.2.3 Stratification

In The observation period of the ERUPT program, the water temperature was minimal in September 1999, but subsequently increased with the increasing of solar radiation, from November until mid-March. From there on the summer stratification slowly disappeared, leaving the water column thoroughly mixed in the following three months. Even during summer, the temperature in the water column was between -2 ºC and +2 ºC. Salinity also contributed, but to a lesser extent, to the stratification, with maximum salinity differences of 0.25 psu being observed between the bottom and the surface. As already mentioned, the low depth of Neptune's Bellows influences the exchanges with the outside, which explains that the waters of Port Foster, below 30 m depth, have different characteristics from those found in Bransfield Strait. Above 200 m the stratification in the Strait is mainly due to salinity, while in Port Foster is dominated by temperature, especially during the summer.

The vertical density gradients are related to the wind and solar radiation. In the Summer-Autumn period, the wind speed decreases, the intensity of solar radiation increases and the water becomes more thermally stratified. This phenomenon is accompanied by the decrease of the mixed layer thickness. In the Winter-Spring period the opposite happens. As the tidal signal also appears in the temperature spectra, we can state that there are three types of variability in the currents within Port Foster: semidiurnal (tidal and solar radiation), diurnal (tide) and seasonal (wind and solar radiation). There is another component of the diurnal (and seasonal) variability associated with the vertical migration of zooplankton. Besides temporal variability, there is an important spatial variability associated with irregular topography.

Looking at the temperature spectra (Figure 6) it is observed that below 90 m, during the stratified water period (Summer-Autumn), there's a strong signature of the K1 diurnal tide component, and less intense semidiurnal components M2 and S2. Solar radiation can give rise to diurnal fluctuations of the thermocline with frequencies close to K1, which does not explain the energy peaks near the bottom, presumably related to baroclinic tides due to the combination of stratification, irregular topography and barotropic tides. Despite the clear evidence of these tides the component K1 cannot be the cause of this phenomenon. Indeed, given that the period of the baroclinic tides is always less than the inertial period (T=13:42 h), and the K1 period is T=23.92 h, the baroclinic tides are most likely associated with components such as 3K1 (T=7.98 h) and 4K1 (T=5.98 h). The complex bathymetry of Port Foster, with steep gradients of bathymetry, plays a key role in the generation of baroclinic tides, which occur mainly during the spring/summer when the thermal stratification is more pronounced, occurring also during the period of mixed waters due to saline stratification.

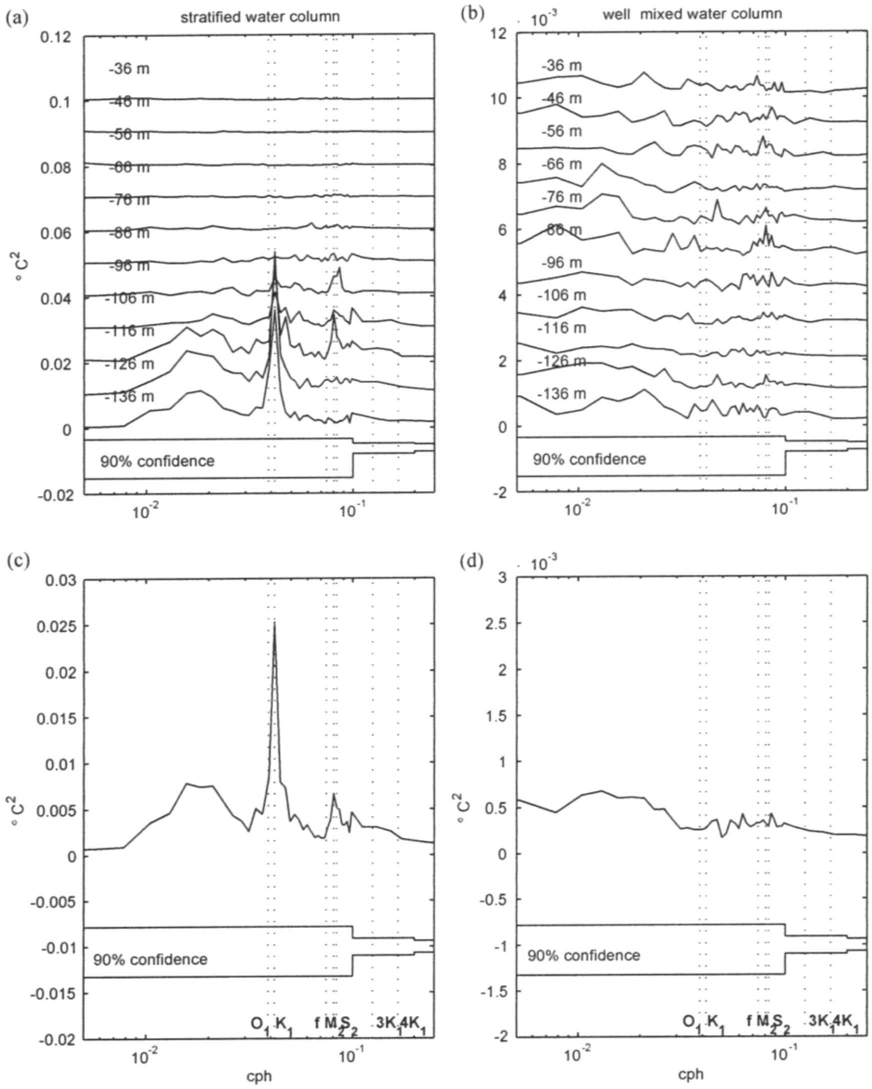

Figure 6 - Variance-preserving frequency spectra of temperature during summer stratification ((a) and (b)) and deep winter-mixed layers ((b) and (d)). In (c) and (d), the spectra show are averaged over 96-136 m. Note that the scales for the well-mixed layer spectra are an order of magnitude smaller than for the stratified temperature spectra; the spectra for each depth in (a) are offset by 0.01°C^2 and in (b) the offset is 0.001°C^2. (Lenn et al. / Deep-Sea Res. II, 50, 1665-1684).

2.2.4 Baroclinic Tide

Baroclinic tides, namely internal waves of tidal period, were first observed in the ocean by Helland-Hansen and Nansen (1909) in the Norwegian Sea by means of hydrographic observations, using Nansen bottles, repeated at short intervals (Baines 1973). Baroclinic tides are internal waves in stratified fluids that result from the interaction of barotropic tides (generated by astronomical forcing) with topography (Levine & Padman et al. 1997).

Tides and related processes can strongly influence the hydrography, mean circulation, and water mass exchanges in ice-covered seas (Foster et al., 1987; Padman et al., 1992; Padman, 1995). According to Lenn et al (2003), internal tides are generated in Neptune's Bellows, and the study of these tides is an important issue in understanding water column mixing processes inside Port Foster.

Unlike the regularity of the barotropic tide, the amplitude and phase of internal tides are variable in time, which implies that there is no universal model for their prediction. Many authors mention that the frequency band for freely propagating internal waves (called internal wave "continuum") is $f < \omega < N$, $f = 2\Omega sin\emptyset$ being the Coriolis Frequency (equal to twice the earth rotation rate about the vertical axis) and N the Brunt-Väisälä frequency (parameter that expresses the strength of stratification, $N^2 = -\frac{g}{\rho_0}\frac{\partial\rho}{\partial z}$) (Baines 1973; Levine & Padman et al. 1997; Kundo & Cohen 2004). According to Cushman-Roisin (1996) this domain can be broader, if one takes into account the vertical component of the Coriolis acceleration.

2.3. The Mathematical Model

The model used during this work was MOHID water 3D (Braunschweig et al. 2002), which since its creation has been applied to various locations, different conditions and for different purposes (Vaz et al. 2005; Trancoso et al. 2005; Coelho et al. 1999). This numerical tool is responsible for the modelling of hydrodynamic processes, the simulation of dispersion phenomena, wave propagation, sediment transport, biogeochemical processes in the water column and exchanges with the bottom.

This model is built through an interconnected set of models using object-oriented programming in FORTRAN 95, as described in Decyk (Decyk et al. 1997), each module being responsible for the management of a portion of the information, summing to a total of 39 modules developed over three decades of research work. This type of programming has proven to be a very useful methodology in the development of complex programs, especially the ones aiming to simulate real world problems (Fernandes 2005).

MOHID is extremely useful to this work, because it allows the study of fluid mechanics taking into account several important forcings. Nowadays it can be rated one of the most developed among existing systems of this type, with several choices of vertical coordinates, as well as a reliable programming (Fernandes 2005). MOHID was developed for a large range of scales and physical conditions, and this study will be a good test to its capabilities since no prior use was done in the Antarctic region.

2.3.1 Model Equations

MOHID uses an Arakawa type C grid (Purser & Leslie 1988) and a finite volume approach to calculate the velocities, the water level and several scalar properties. The water level and the properties of the water are calculated in the center of the grid cells and the velocities in the faces of each cell. The model solves the three-dimensional incompressible primitive equations. All the equations presented below have been derived taking into account the assumption of hydrostatic equilibrium as well as Boussinesq and Reynolds approximations. The horizontal momentum equations are, in Cartesian form:

$$\begin{aligned}\frac{\partial u}{\partial t} = &-\frac{\partial (uu)}{\partial x} - \frac{\partial (uv)}{\partial y} - \frac{\partial (uw)}{\partial z} + fv - \frac{1}{\rho_0}\frac{\partial p}{\partial y} \\ &+ \frac{\partial\left((v_H)\frac{\partial u}{\partial x}\right)}{\partial x} + \frac{\partial\left((v_H)\frac{\partial u}{\partial y}\right)}{\partial y} + \frac{\partial\left((v_V)\frac{\partial u}{\partial z}\right)}{\partial z}\end{aligned} \tag{1}$$

$$\begin{aligned}\frac{\partial v}{\partial t} = &-\frac{\partial (vu)}{\partial x} - \frac{\partial (vv)}{\partial y} - \frac{\partial (vw)}{\partial z} - fu - \frac{1}{\rho_0}\frac{\partial p}{\partial y} \\ &+ \frac{\partial\left((v_H)\frac{\partial v}{\partial x}\right)}{\partial x} + \frac{\partial\left((v_H)\frac{\partial v}{\partial y}\right)}{\partial y} + \frac{\partial\left((v_V)\frac{\partial v}{\partial z}\right)}{\partial z}\end{aligned} \tag{2}$$

Where u, v and w are the components of the velocity vector in the x, y and z directions respectively, f is the Coriolis parameter, v_H and v_V the turbulent viscosities in the horizontal and vertical directions and p is the pressure. The temporal evolution of velocities (term on the left hand side) is the balance of advective transports (first three terms on the right hand side), Coriolis force (fourth term), pressure gradient (fifth term) and turbulent diffusion (last three terms).

The vertical velocity is calculated from the incompressible continuity equation (mass balance equation):

(3)

$$\frac{\partial u}{\partial x}+\frac{\partial v}{\partial y}+\frac{\partial w}{\partial z}=0$$

The free surface equation is obtained by integrating the equation of continuity over the whole water column (between the free surface elevation z=η(x,y,t) and the bottomz=-h(x,y)):

$$\frac{\partial \eta}{\partial t}=-\frac{\partial \int_{-h}^{\eta} u dz}{\partial x}-\frac{\partial \int_{-h}^{\eta} v dz}{\partial y} \tag{4}$$

The equation of hydrostatic pressure is:

$$\frac{\partial p}{\partial z}+g\rho=0 \tag{5}$$

where g is gravity and ρ the density. Integrating this equation in the vertical and considering that $\rho=\rho_0+\rho'$ where ρ_0 is a constant reference density and ρ' a density perturbation, yields:

$$p(z)=p_{atm}+g\rho_0(\eta-z)+g\int_z^{\eta}\rho' dz \tag{6}$$

Eq. 6 relates the pressure at any depth with the atmospheric pressure at the sea surface, the sea level and the anomalous density integrated between that level and the sea surface. With this equation and the Leibnitz rule the pressure term in the horizontal momentum equations becomes:

$$\frac{1}{\rho_0}\frac{\partial p}{\partial x_i}=\frac{1}{\rho_0}\frac{\partial p_{atm}}{\partial x_i}+g\frac{\partial \eta}{\partial x_i}+\frac{g}{\rho_0}\int_z^{\eta}\frac{\partial \rho'}{\partial x_i}dz \tag{7}$$

The total pressure gradient is the sum of the gradients of atmospheric pressure, sea surface elevation (barotropic pressure gradient) and density distribution (baroclinic pressure gradient). Regarding the density, its value is obtained from the values of salinity and temperature, using the equation (Leendertsee & Liu, 1978):

$$\rho=\frac{(5890+38T-0.375T^2+3S)}{((1779.5+11.25T-0.0745T^2)-(3.8+0.01T)S+0.698(5890+38T-0.375T^2+3S))} \tag{8}$$

The Hydrodynamic Model computes the advective and diffusive fluxes, the discharges of water, sediment fluxes, oxygen and heat changes with the atmosphere and sedimentation fluxes. The transport of any property φ due to advection and diffusion can be described by the following equation:

$$\frac{\partial \varphi}{\partial t} = -\frac{\partial (u\varphi)}{\partial x} - \frac{\partial (v\varphi)}{\partial y} - \frac{\partial (w\varphi)}{\partial z} + \frac{\partial \left(k_H \frac{\partial \varphi}{\partial x}\right)}{\partial x} + \frac{\partial \left(k_H \frac{\partial \varphi}{\partial y}\right)}{\partial y} + \frac{\partial \left(k_V \frac{\partial \varphi}{\partial z}\right)}{\partial z} + (S_0 - S_i) \tag{9}$$

Where k_H and k_V are the horizontal and vertical turbulent diffusivities of that property. The first term on the left is the partial derivative of the property with respect to time, the next three terms represent the advective transport, the following three terms the diffusive transport, and $(S_0 - S_i)$ the sources minus the sinks. The temporal evolution of the property φ depends, therefore, on the balance between the advective and diffusive fluxes and the sources and sinks associated (MOHID Modelling System Description).

2.3.2 Initial and Boundary Conditions

The model requires initial conditions and boundary conditions in the earth, ocean and atmosphere interfaces in order to solve the differential equations. In the boundaries close to land (lateral closed boundaries), the cell faces in contact with land have null fluxes. At the free surface the model can take into account the wind surface stress, the energy fluxes and mass fluxes. At the bottom boundary advective fluxes are null and the diffusive flux of momentum is estimated by means of a bottom stress law that depends on the near-bottom velocity. One of the more complex boundaries is the open boundary since it is not a physical boundary. Open boundaries exist due to the computational domain chosen. They should allow the imposition of properties of the input field (e.g., a tidal wave) and, at the same time, be transparent with respect to all the waves generated within and exiting the computational domain. If this condition is not met, the open boundary behaves like a physical boundary where reflections occur due to numerical errors. The best way to impose this condition depends on the case of study. “Open boundary conditions is a “science” within hydrodynamic and transport modelling. An extensive overview on how this type of boundaries is handled in MOHID Water can be found in Leitão (2003)” (Cited by Bernardes 2007).

3. Methodology

In this chapter, it is described the model implementation. The numerical computation has been carried out on a spatial domain that represents Port Foster and the surroundings through a grid consisting of 80000 rectangular elements with a horizontal resolution of $\Delta x = \Delta y = 50$ m (Figure 7).

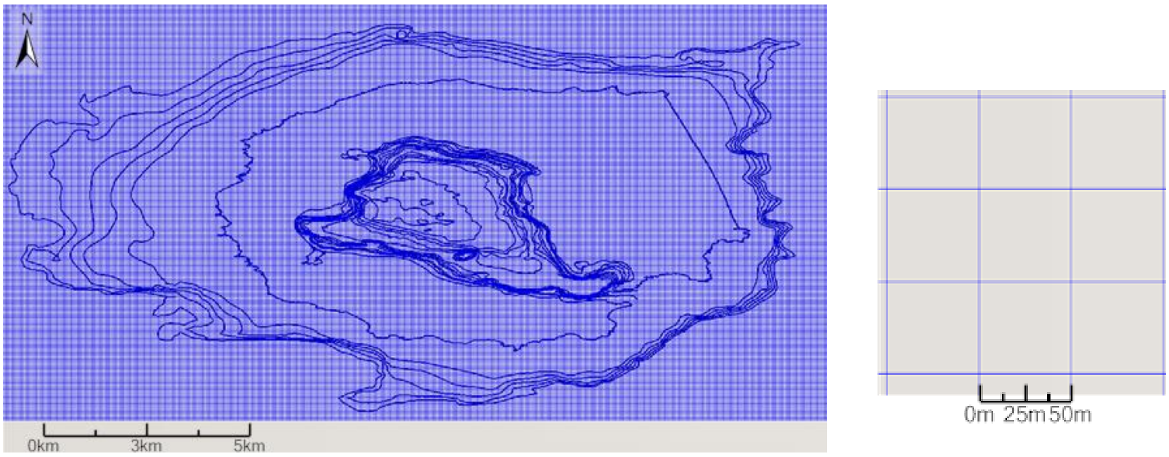

Figure 7 - Representation of the grid used in the computational domain.

3.1 The Model Parameterization

The parameters related with the hydrodynamics of the model are the bottom drag coefficient and the horizontal and vertical viscosities. The value assumed for bottom drag coefficient was 3×10^{-3}, and for horizontal viscosity 3 $m^2 s^{-1}$ (This values were chosen taken into account the previous study by Vidal et al. (2010)). The vertical viscosity was obtained using General Ocean Turbulence Model (GOTM).

3.3.1 2D Model

In the 2D Model, besides the general model parameterization presented above, the tide presented in annex (Annex A) was applied.

3.3.2 3D Model

The 3D Model is a continuation from the validated tidal model, where the T-S profiles where applied with the intuition to understand their role in the currents behavior. Since there was no reliable data for winds and radiation, the profiles were frozen in time, i.e, the third term on the right-hand side of equation (7) doesn´t change with time. The water properties file can be consulted in annex (Annex B).

3.2 Bathymetry

The bathymetry, known to be responsible for many problems associated with the model, greatly influences the water circulation and the transport of the properties simulated in the domain.

The bathymetry consists of three elements: The grid presented in Figure 7, the bathymetric points and the coastline that gives the closed border.

The Bathymetry of the bay and the coastline already existed and were created by the spatial data infrastructure of the Deception island (SIMAC-IDEDEC), maintained by the Laboratory of Astronomy, Geodesy and Cartography of the University of Cadiz, Spain. It was provided by Torrecillas et al, 2006, as represented in Figure 8.

The outline bathymetry (Figure 9) was based on a grid from the Autochart Bathymetric Map Production from NOAA. The information was processed using the software Arcgis and subsequently georeferenciated.

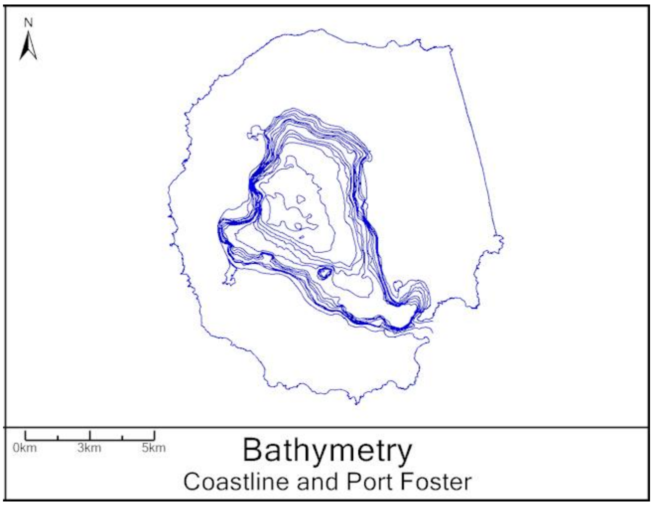

Figure 8 - Coastline and Port Foster Bathymetry.

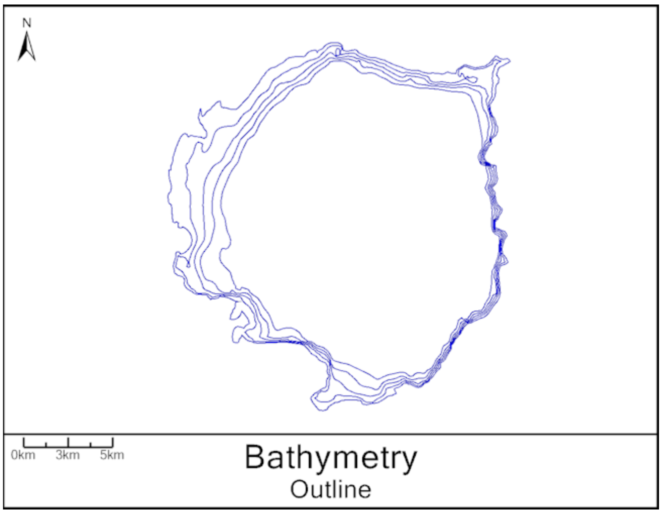

Figure 9 - Outline Bathymetry.

The first bathymetry used had some steep regions and lack of depth information near the coastline, therefore, after the first attempt simulations the conclusion was that in some regions the model was calculating wrong values due to sudden changes in depth. After adjustments near the coastline based on what the existing depth would be expected and also using the tool SmothBathymetry in order to eliminate some irregularities and to soften the bathymetry (creation of mid-points in regions of high-slope) through a series of interpolations, the final bathymetry was obtained (Figure 10). The resulting bathymetry was compared with the one presented in Barclay et al (2009) and the depths were similar for each zone (Figure 10).

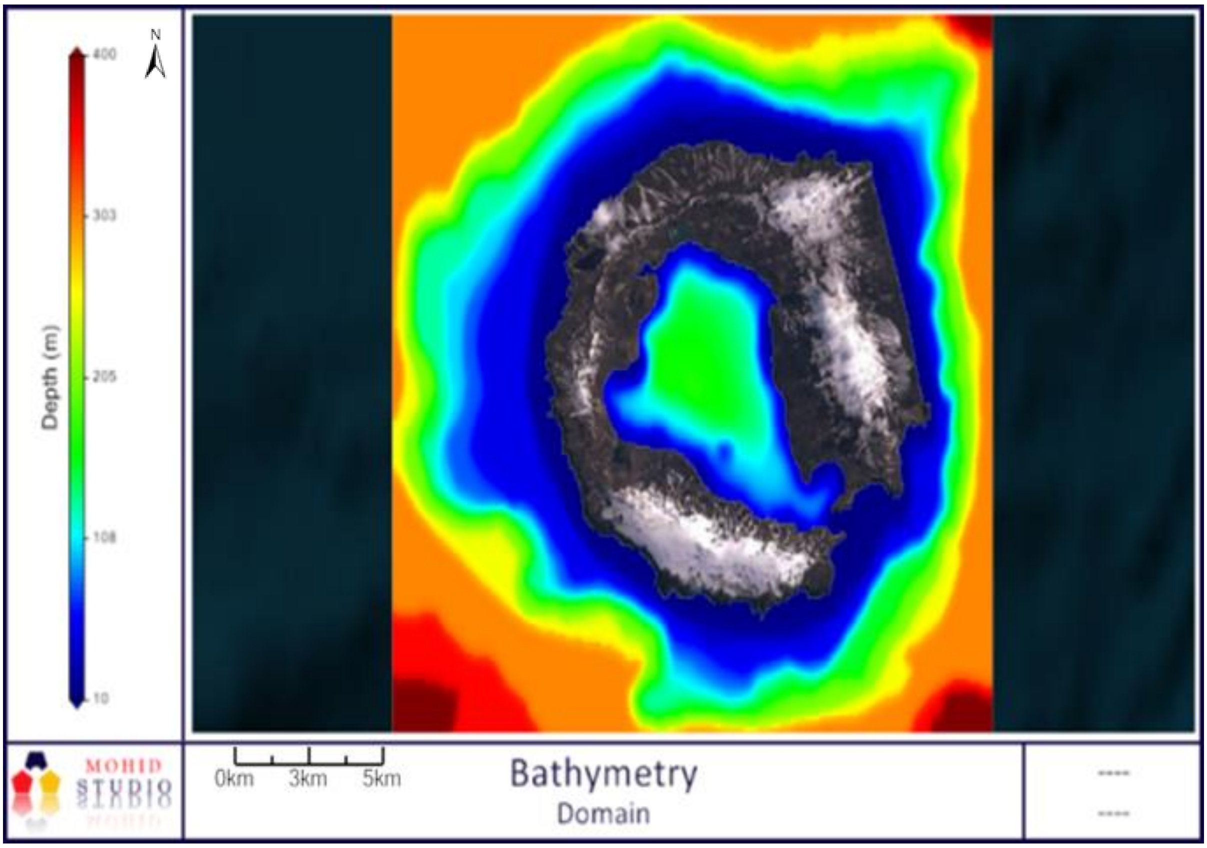

Figure 10 - Bathymetry used to run the MOHID Water model.

3.3 Vertical Mesh

The Vertical Mesh applied to the Model uses Cartesian Coordinates (Table 1) allowing the input of the T-S Profiles along the domain, since it doesn't vary depending on the bathymetry.

Table 1 - Cartesian Coordinates.

Cartesian Coordinates		
Mohid ID	Layers Tickness (m)	Depth(m)
18	2	2
17	3	5
16	4	9
15	5	14
14	6	20
13	10	30
12	11	41
11	12	53
10	13	66
9	14	80
8	15	95
7	20	115
6	25	140
5	30	170
4	40	210
3	50	260
2	60	320
1	80	400

3.4 Tide

The tide level and the phase of the components were forced in the boundary of the domain using FES2004, which is the tide level and harmonic predictor for tide of POC-LEGOS, inputting 14 harmonic components to the model (M2, S2, K1, K2, N2, 2N2, O1, Q1, P1, M4, Mf, Mm, Mtm and MSqm). In FES2004, 15 tidal constituents are distributed on 1/8° grids (amplitude and phase), 28 others constituents are taken into account by the means of a specific admittance method (a long period wave computation and ice on polar regions are taken into account).

3.5 Time Series

The locations for the time series used during this project were chosen taking into account the previous tidal data collected, the great interest to study Neptune’s Bellows and also the more relevant places inside Port Foster. Figure 11 shows the time series locations with the respective identification (Table 2). For the study of mercury circulation, the sites chosen to monitor were the ones where Mão de Ferro (2012) collected the more significant mercury samples and are marked with an asterisk on Table 2.

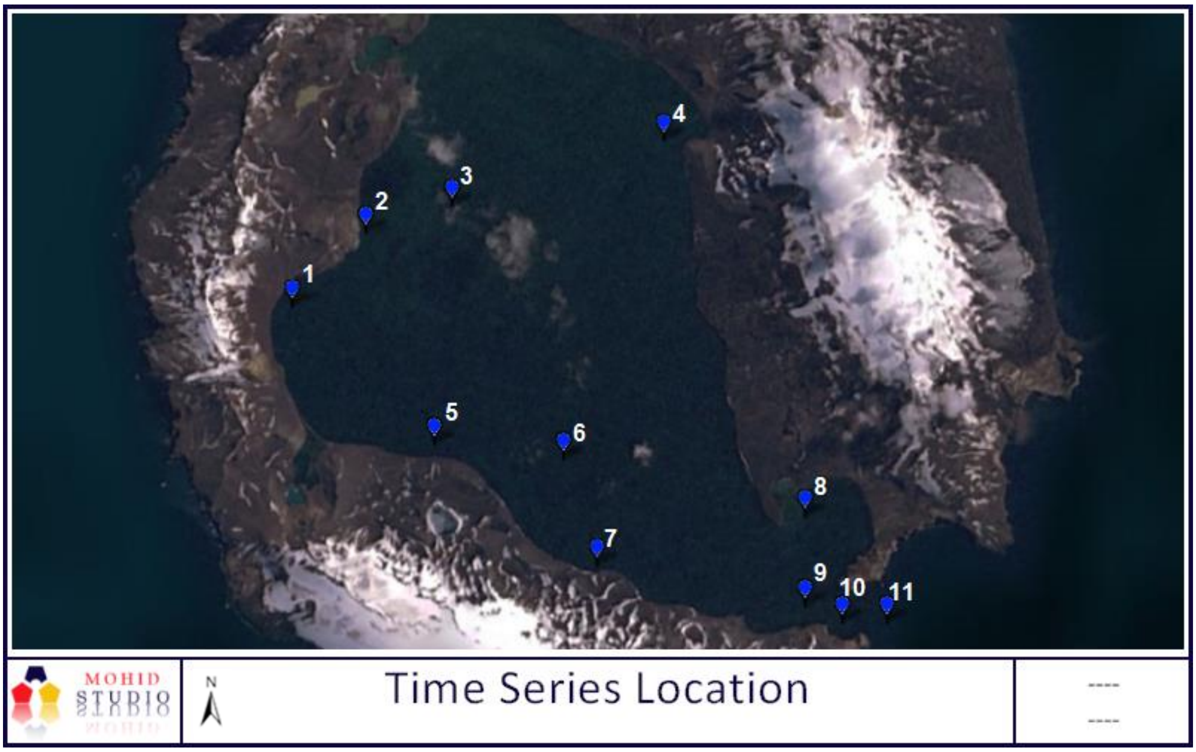

Figure 11 - Time Series Location.

Table 2 - Time Series Coordinates.

ID	Location	Latitude	Longitude
1	Near Fumaroles*	-62.9579	-60.7075
2	NW Coast*	-62.9489	-60.6877
3	Center Depth	-62.9456	-60.6645
4	Pendulum Cove	-62.9376	-60.6075
5	Between ColaFum*	-62.9748	-60.6693
6	Stanley Patch	-62.9766	-60.6345
7	Colatina*	-62.9896	-60.6255
8	Whaller’s Bay	-62.9836	-60.5695
9	Inside Bellow’s	-62.9946	-60.5695
10	Neptune’s Bellows	-62.9966	-60.5595
11	Outside Bellows	-62.9966	-60.5475

3.6 Salinity and Temperature

The salinity and temperature profiles applied in the model were obtained by a research group, led by chief scientist Smith et al. (2003b), during the ERUPT expeditions; the ones used were collected during ERUPT III and V, that occurred in the summer and winter of 2000, respectively. The profiles chosen (figure 12) are representative of the inside (right image for both seasons) and outside of the island (center image for summer and left image for winter). The ERUPT raw data was provided to me by Sturz et al. (2003).

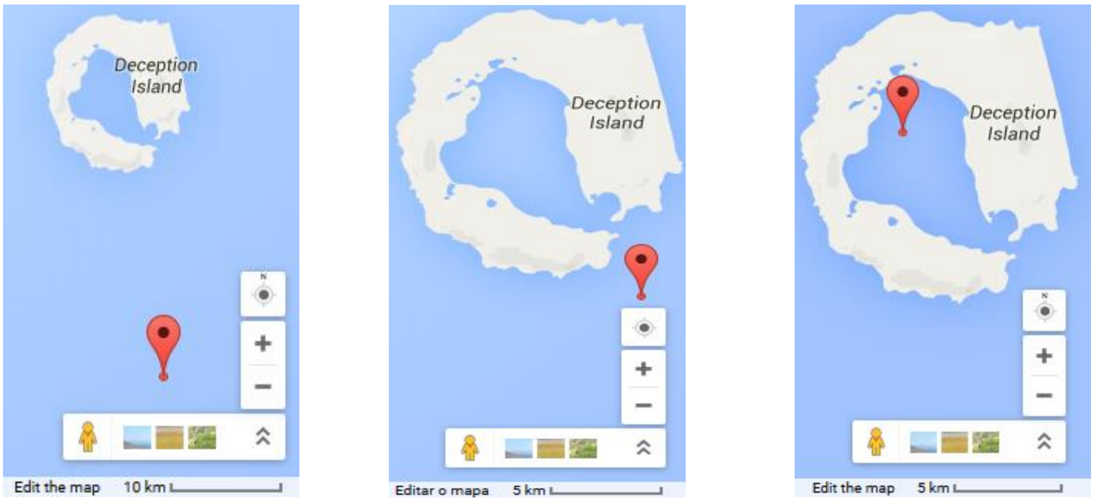

Figure 12 - Location of the T-S profiles applied in the model (Left Image: 63 º 11'S, 60 º 32.606’W; Center Image: 63º01.7'S, 60º32.0'W; Right Image: 62 º 56.7’S, 60 º 39.5’W).

The T-S profiles that represent winter and summer conditions inside and outside Port Foster can be seen in annex (Annex C). The final result after interpolation between the inside and the outside of Port Foster is the following for summer (figure 13) and for winter (figure 14) temperature profiles.

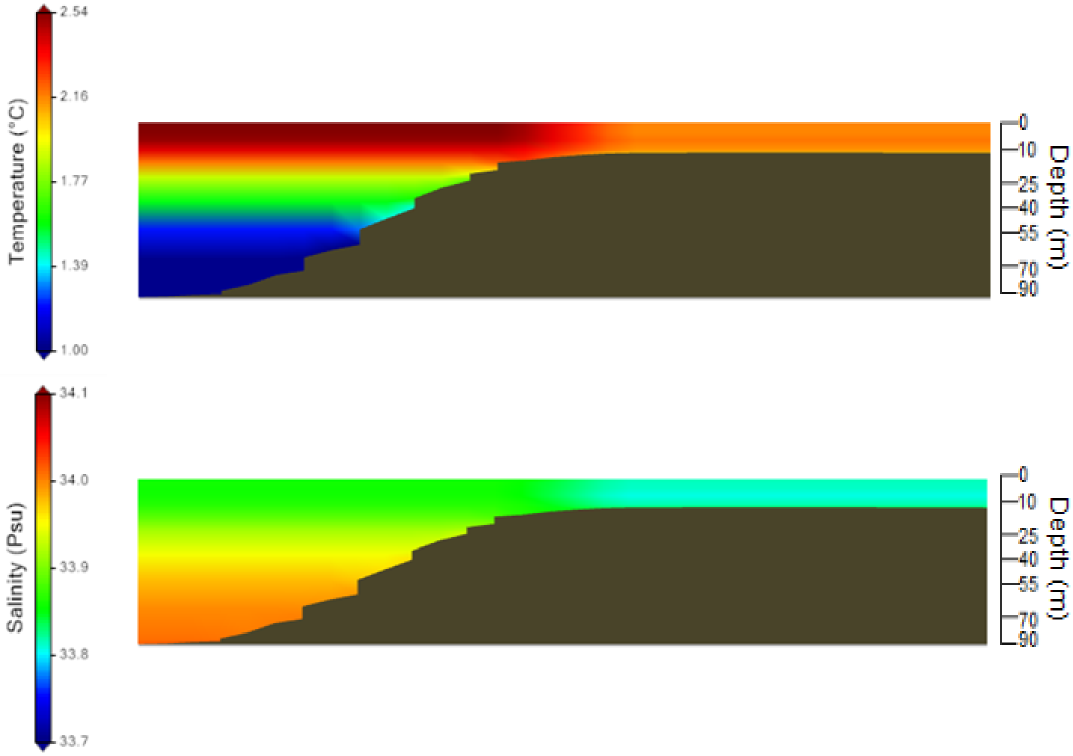

Figure 13 - Summer Temperature and Salinity Profiles – Vertical Cut in Neptune's Bellows.

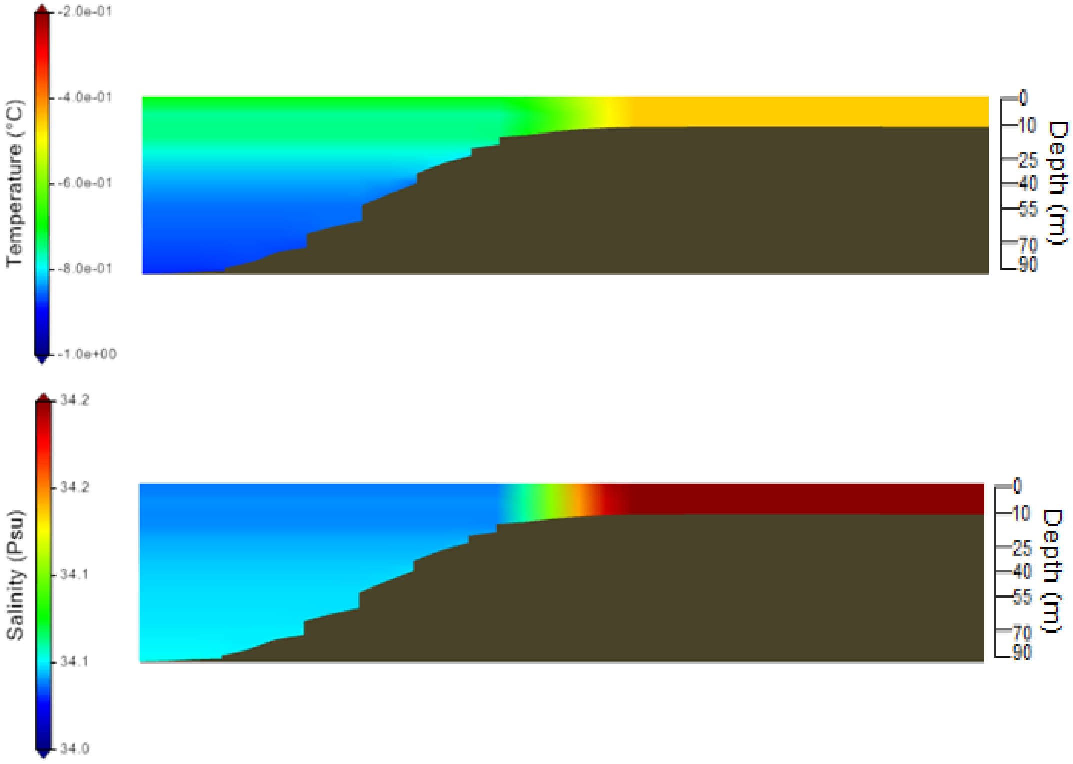

Figure 14 - Winter Temperature and Salinity Profiles – Vertical Cut in Neptune's Bellows.

3.7 Winds and Radiation

For both winds and radiation the data in Deception available was scarce. For radiation, the most reliable data was from monthly average insolation that already took into account the albedo (https://eosweb.larc.nasa.gov), although hourly data is necessary for the model. For winds, raw data that was collected from March of 2004, 2006, 2007, 2009, and analyzed with the aim of understanding the predominant directions of the winds and the average wind speed. This wind data (wind speed in meters per second) was collected by R/V Laurence M. Gould Cruise during different expeditions. Since the ship was not anchored from more than a few hours in the same place, a study of wind speed and direction was done for different eight zones of Port Foster (Figure 15). The wind speed data collected was divided between the coordinates of those zones, and for each, an event count and an average wind speed calculation were done to create the wind roses.

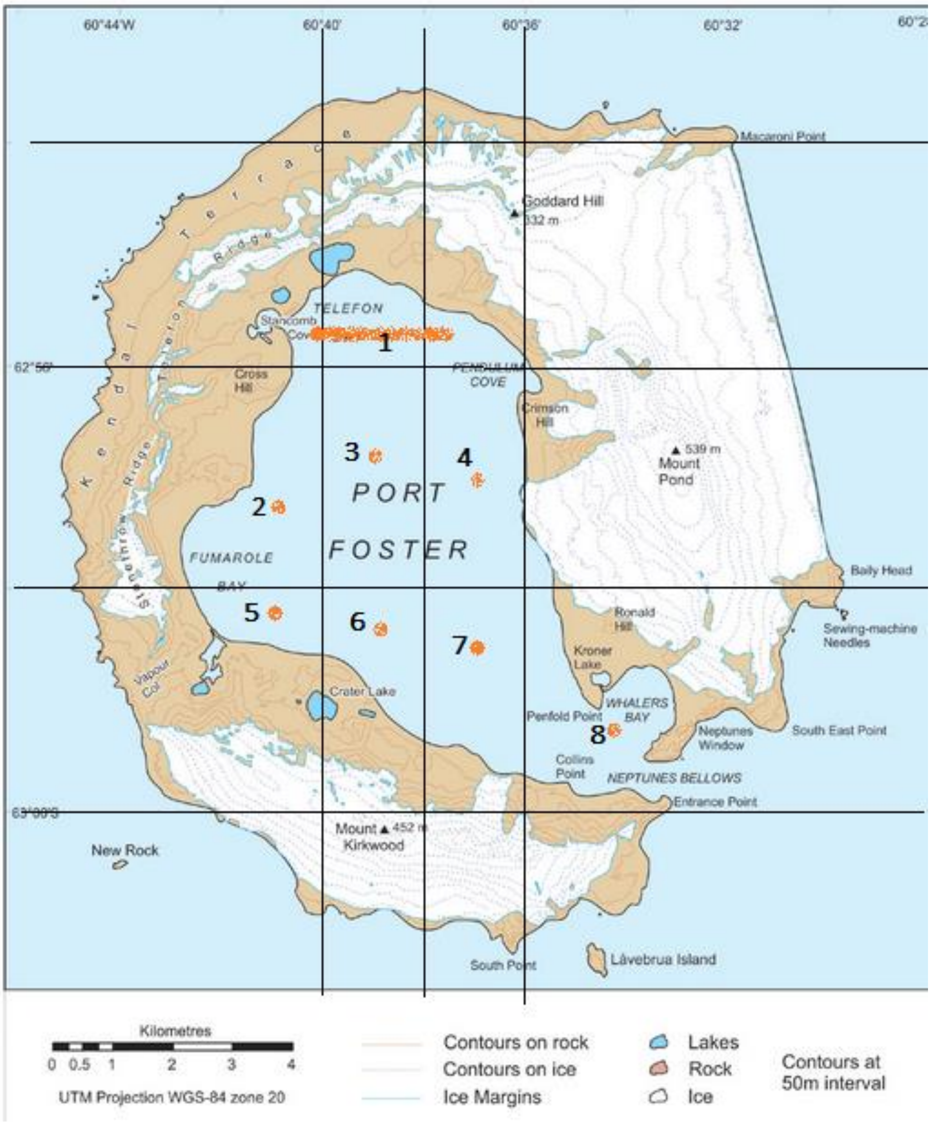

Figure 15 - Topographic map of Deception Island with the eight zones represented.

3.8 Lagrangean Tracers

The lagrangean tracers approach (Leitão, 1996) was used to simulate contaminants circulation in Port Foster. The lagrangean tracers are used to label the water and to monitor its location and movements, and can be expressed by:

$$\frac{dx_i}{dt} = u_i(x_i, t) \tag{10}$$

where x stands for the particle position and u for the mean velocity. The lagrangean module in MOHID was used to compute the tracers, the locations for the initial conditions were chosen taking into account the data collected by Mão de Ferro (2012) for Hg in sea water.

4. 2D Model

4.1 Tidal circulation and Water Level

To describe the tidal circulation, the model was run using the grid presented in chapter three and forced with tide. The model ran for one month (from 2011-07-01 to 2011-08-01), with a timestep of 5s. The following images represent the flood and ebb conditions in the island (figure 16).

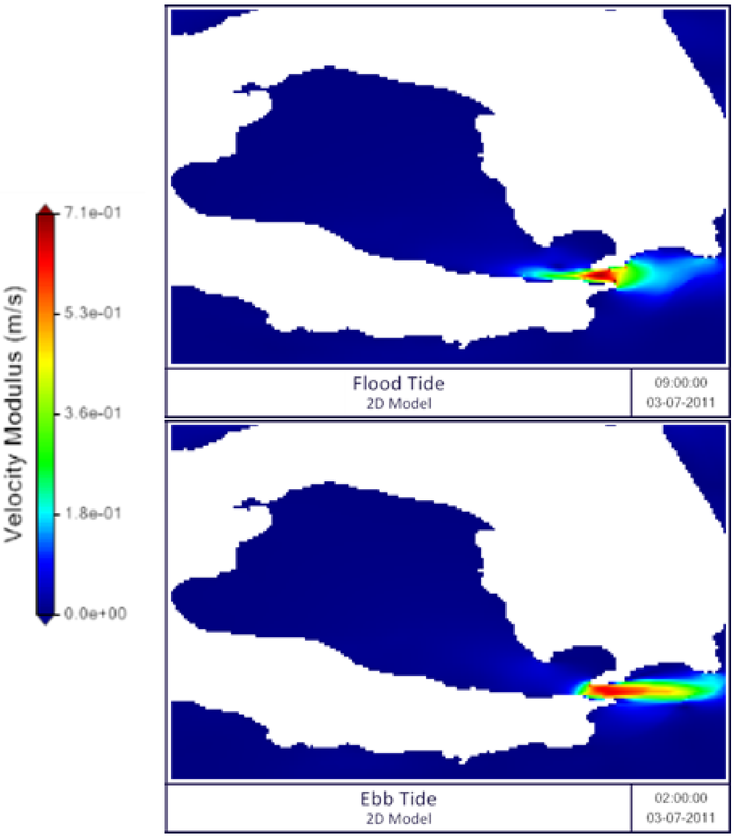

Figure 16 - 2D Model: Flood and Ebb Tide Representation.

Model results (figure 17) show that the amplitudes of the velocities in Neptune's Bellows can reach maximum speeds near 0.60m/s during spring tides. Currents obtained with the model are very small (less than 5 cm/s) within Port Foster. The velocities near the narrow channel of Neptune's Bellows show that the east-west direction is the more important, in agreement with the orientation of the passage.

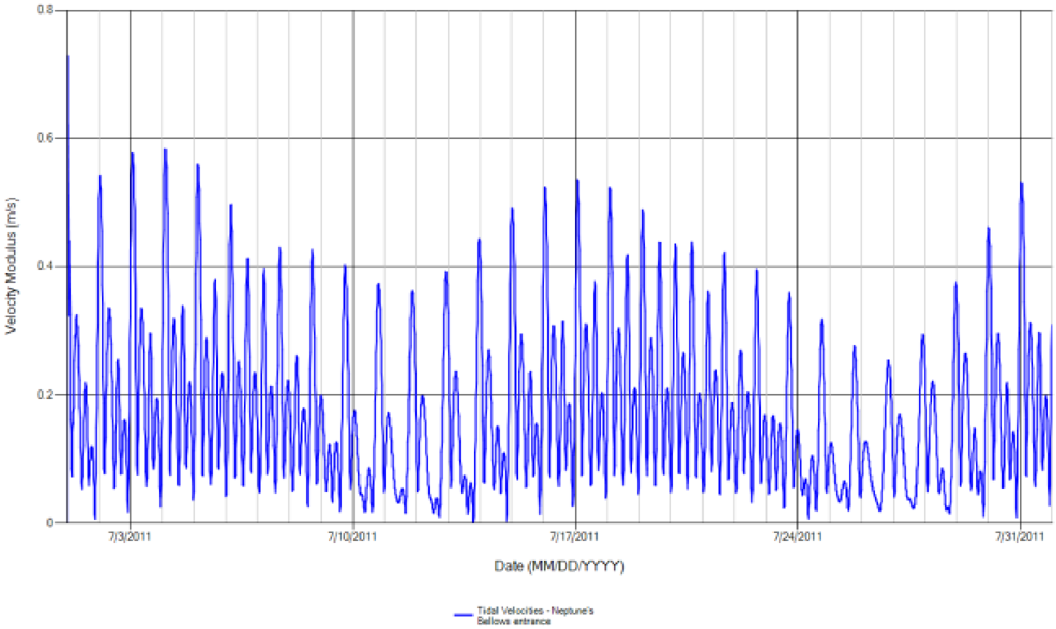

Figure 17 - Neptune's Bellows: Tidal Velocities.

The water level variation in Neptune's Bellows is showed below (figure 18), with an initial reference level of 1.864 meters.

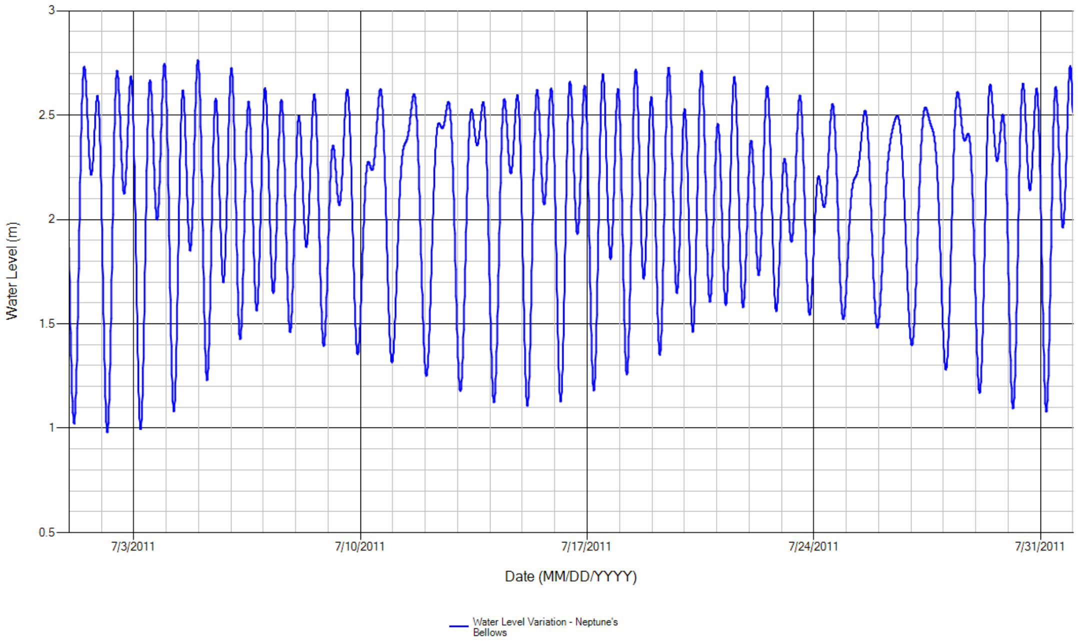

Figure 18 - Neptune's Bellows: Water Level Variation.

A mean tidal level variation is around 1.2 meters, and the largest difference in height is around 1.7 meters.

Looking to the tidal current velocities in the East and West direction along x, both results show a decrease of the velocities amplitude from the boundary layer to the inside of Port Foster (figure 19 and 20).

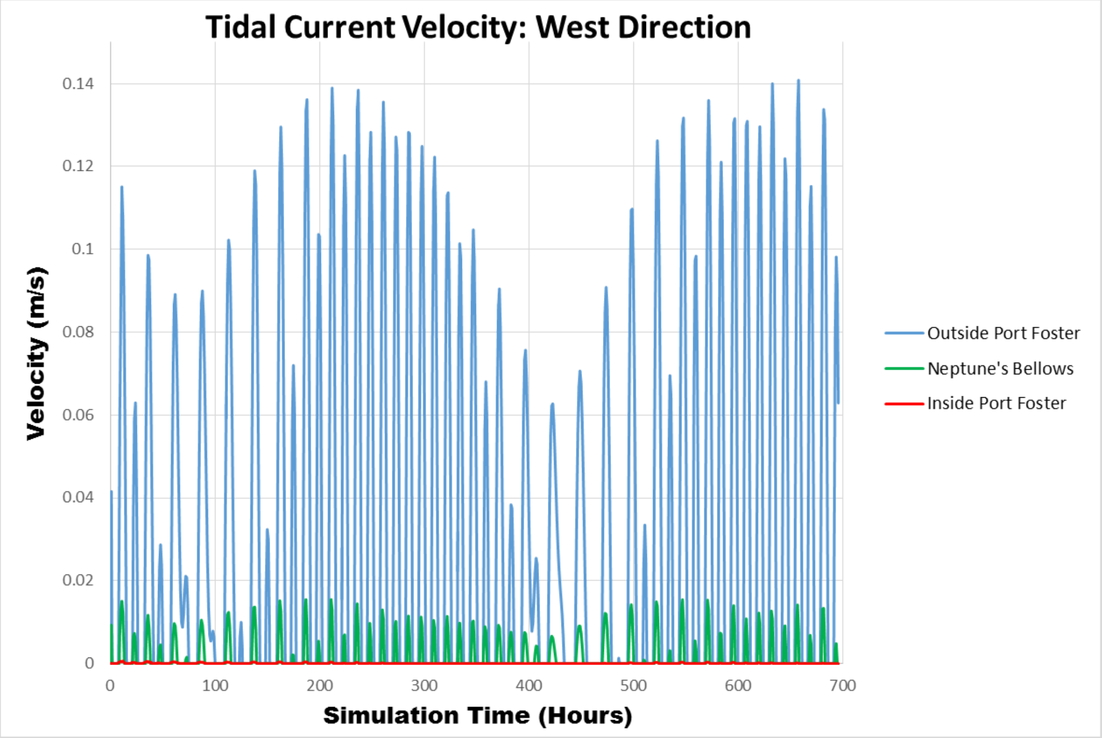

Figure 19 – Tidal Current Velocity: West Direction.

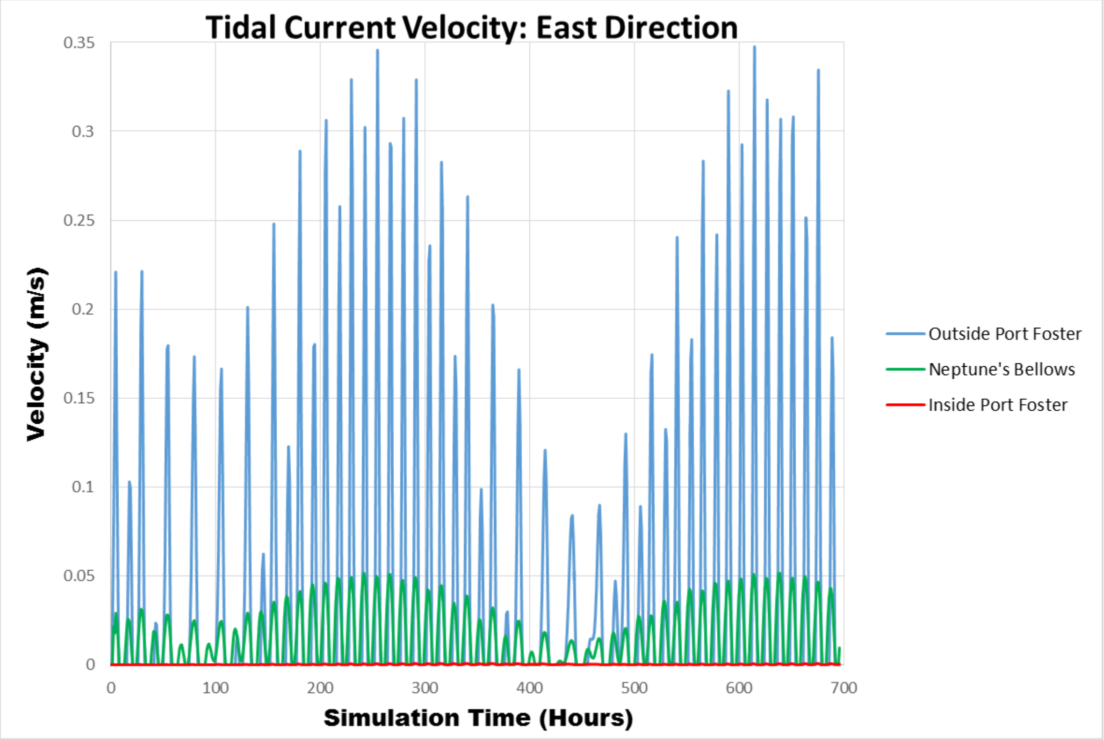

Figure 20 – Tidal Current Velocity: East Direction.

The tidal circulation as a clockwise movement during the flood tide and a counter-clockwise movement during ebb tide (Figures 21, 22, 23, 24).

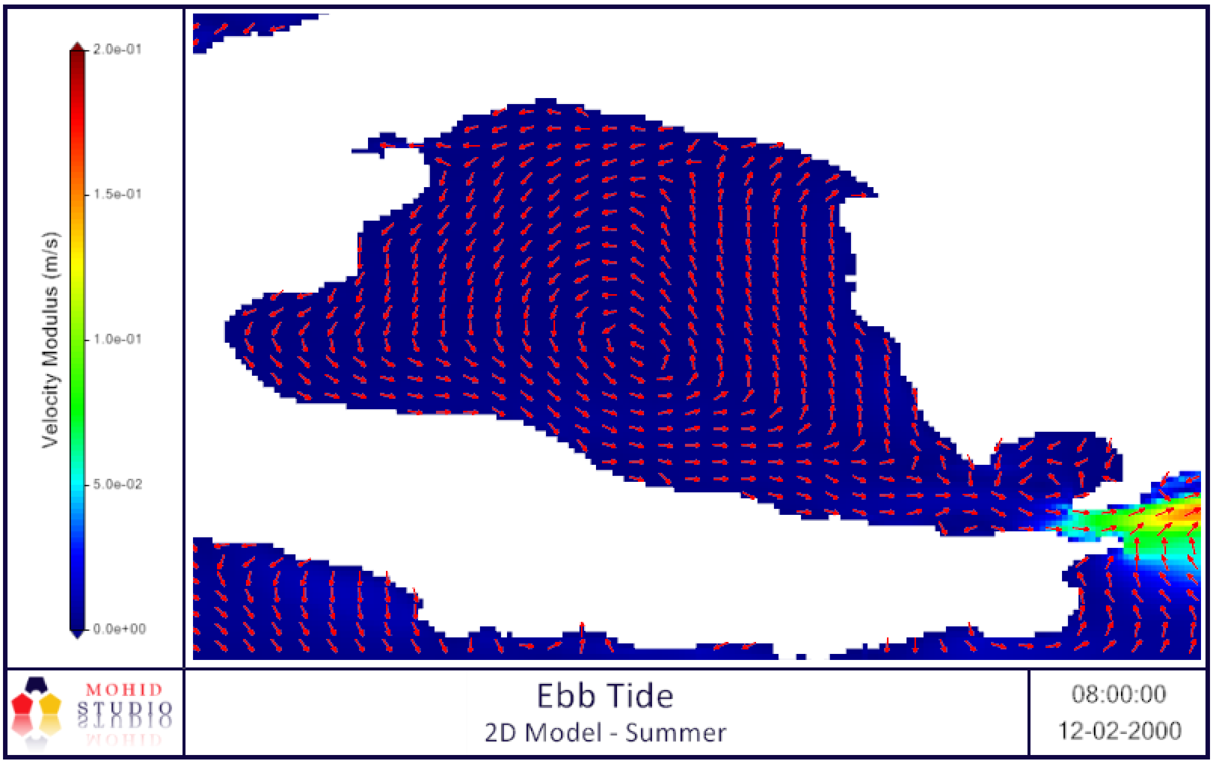

Figure 21 - 2D Model Ebb Tide representation for summer: Near Surface Velocities.

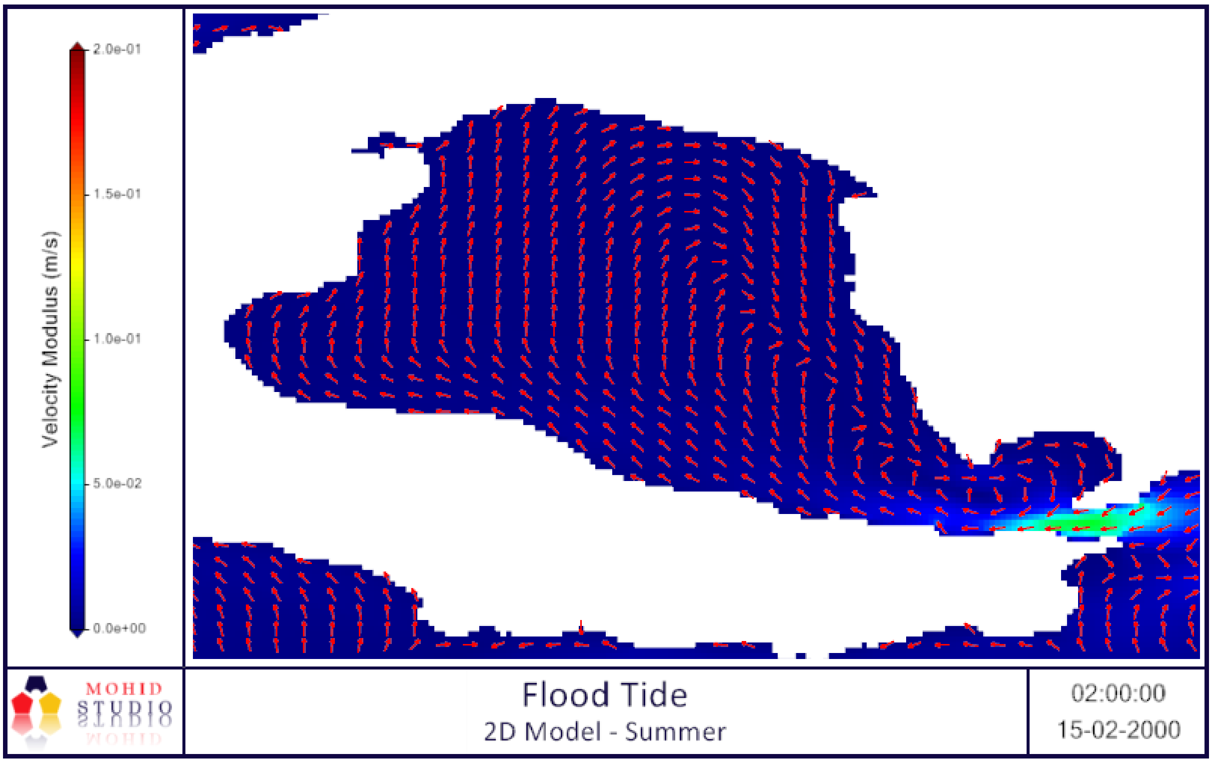

Figure 22 - 2D Model Flood Tide representation for summer: Near Surface Velocities.

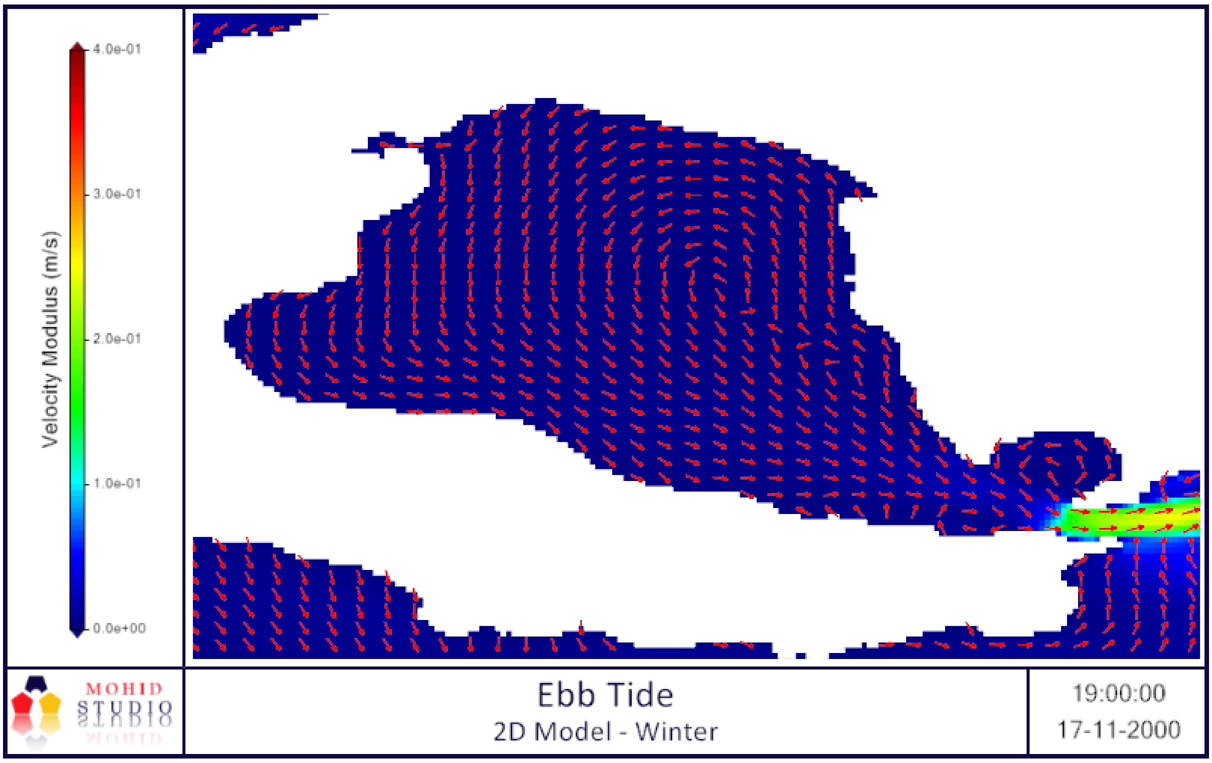

Figure 23 - 2D Model Ebb Tide representation for winter: Near Surface Velocities.

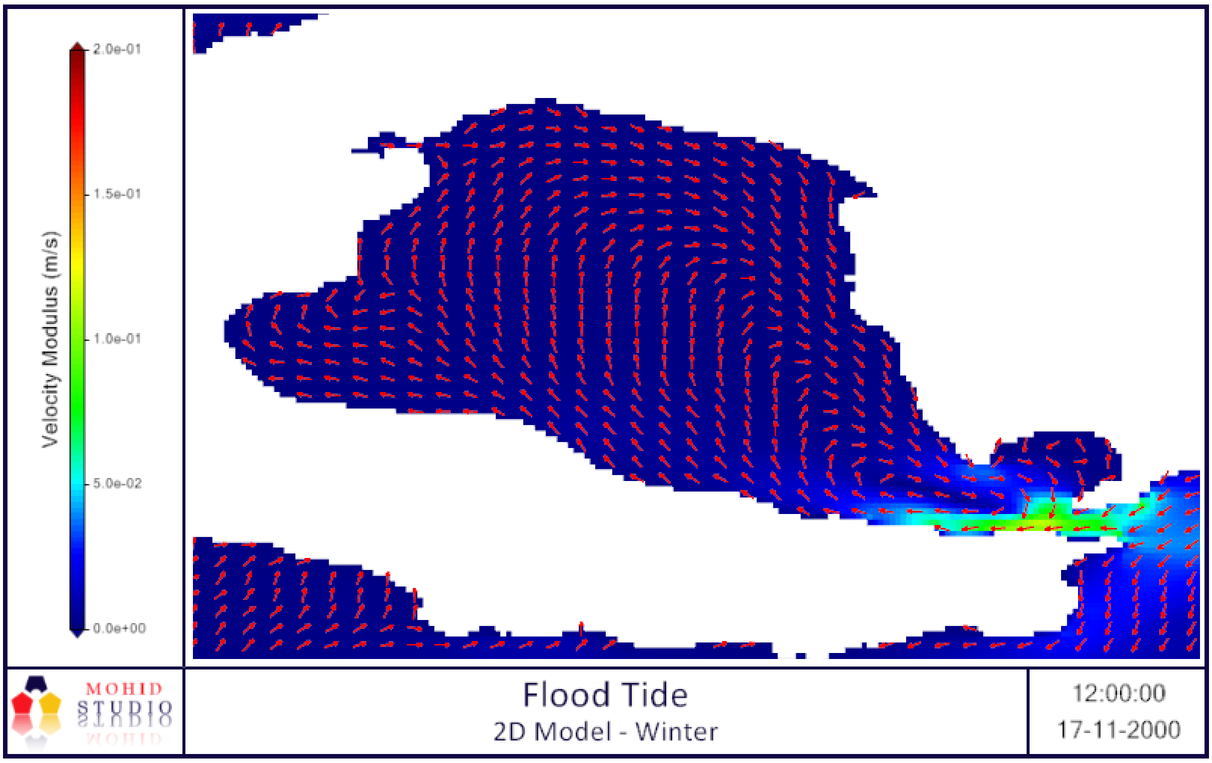

Figure 24 - 2D Model Flood Tide representation for winter: Near Surface Velocities.

4.2 Validation

A statistical analysis was made, comparing the amplitudes and phases of the major components generated with the data available. For the comparison of the model results with “measured” sea levels, the data used is presented in Vidal et al (2010) has a result of an harmonic analysis of the tide gauge data within the island. For each constituent of each simulation, the error in the amplitudes (e_A) and the error in the phases (e_P) were calculated using equations (11) and (12).

$$e_A = \sqrt{\frac{1}{N}\sum_i \frac{(Ao_i - Am_i)^2}{2}} \qquad \textbf{(11)}$$

$$e_P = \frac{1}{N}\sum_i \frac{A_{m_i}^2(\theta o_i - \theta m_i)}{\sum_i A_{m_i}^2} \qquad \textbf{(12)}$$

The error in the amplitudes was calculated from the difference between the observations (*Ao*) and the results (*Am*) of the model, and the error in the phases was calculated from their difference ($\theta o_i - \theta m_i$), but weighted with the values of the modeled amplitudes (*Am*). N is the number of components taken into account.

Tables 2 and 3 present the comparison of the harmonic constants observed (O) in three coastal stations (Balleneros in Whaller’s Bay, Pendulo in Pendulum Cove and Colatinas) with the analysis made to the model results (M).

Table 3 - Harmonic Analysis Results: Amplitude.

		Stations (amplitude presented in meters)		
Tidal Components		Balleneros	Pendulo	Colatinas
M2	M	**0.3723**	**0.3729**	**0.3728**
	O	0.4600	0.4400	0.4000
S2	M	**0.2061**	**0.2065**	**0.2064**
	O	0.2800	0.2900	0.2600
O1	M	**0.2738**	**0.2738**	**0.2738**
	O	0.2900	0.2900	0.2700
K1	M	**0.3113**	**0.3115**	**0.3114**
	O	0.2600	0.2600	0.3000
e_A		**0.04**	**0.04**	**0.02**

Table 4 - Harmonic Analysis Results: Phase.

		Stations (phase presented in degrees relative to local time)		
Tidal Components		Balleneros	Pendulo	Colatinas
M2	M	**281**	**281**	**281**
	O	280	281	283
S2	M	**360**	**360**	**360**
	O	Not Obs.	Not Obs.	351
O1	M	**49**	**49**	**49**
	O	48	55	53
K1	M	**68**	**68**	**68**
	O	66	73	74
e_P		**0.5**	**0.8**	**1.5**

The tide in Port Foster was adequately reproduced and the tidal model was validated, therefore it can be used with high confidence.

4.3 Residence Time

An important result is the residence time, because it gives the average amount of time a particle spends in the caldera and, therefore, its impacts. Using the following approach, the residence time was determined:

$$Tresidence = \frac{V}{Cs * Mf} \sim 1.7\ years$$

- Volume of Port Foster (V) = 3626 hm^3;
- Mean Flow entering Port Foster (Mf) = 1.2 cm/s;
- Cross-section at Neptune's Bellows (Cs) = 5500 m^2

This result it's close to what was expected, since Lenn et al. (2003) obtained for the residence time 2.4 years, based in a mean flow entering Port Foster of 1 cm/s. A residence time of 1.7 years is too large and explains the negative environmental impact resulting from the accumulation of metals, such as Hg. It is also important to stress that this result is strongly influenced by stratification, therefore easily varying with seasonal variations.

5. 3D Model

This chapter describes the 3D model as well as the possibility of internal tides formation. It also shows the movement of particles that represent Hg with the use of lagrangean tracers.

5.1 Hydrodynamics

5.1.1 Spatial Analysis

The following results describe the flood and ebb tide situations in the two seasons with focus on the circulation inside Port Foster (figures 25, 26, 27 and 28). Comparing the currents circulation between the 2D and 3D models, there’s no significant alteration in the same.

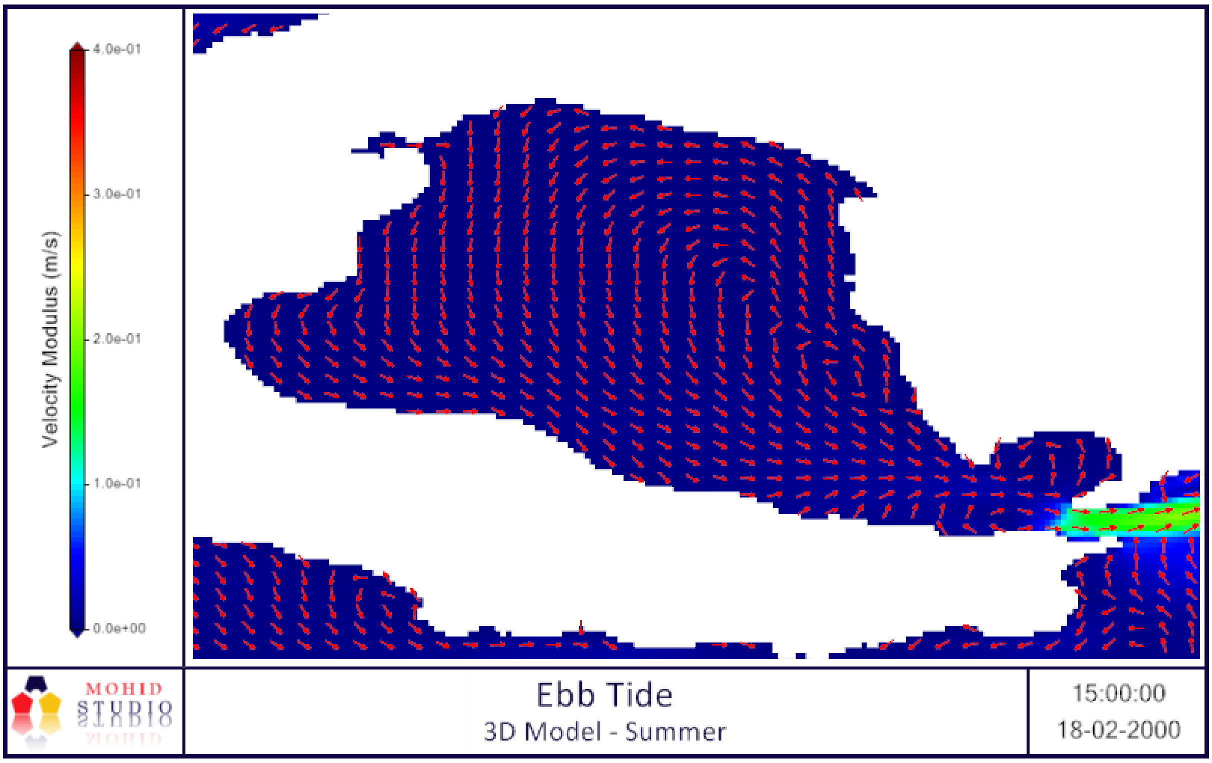

Figure 25 - 3D Model Ebb Tide representation: Near the surface velocities.

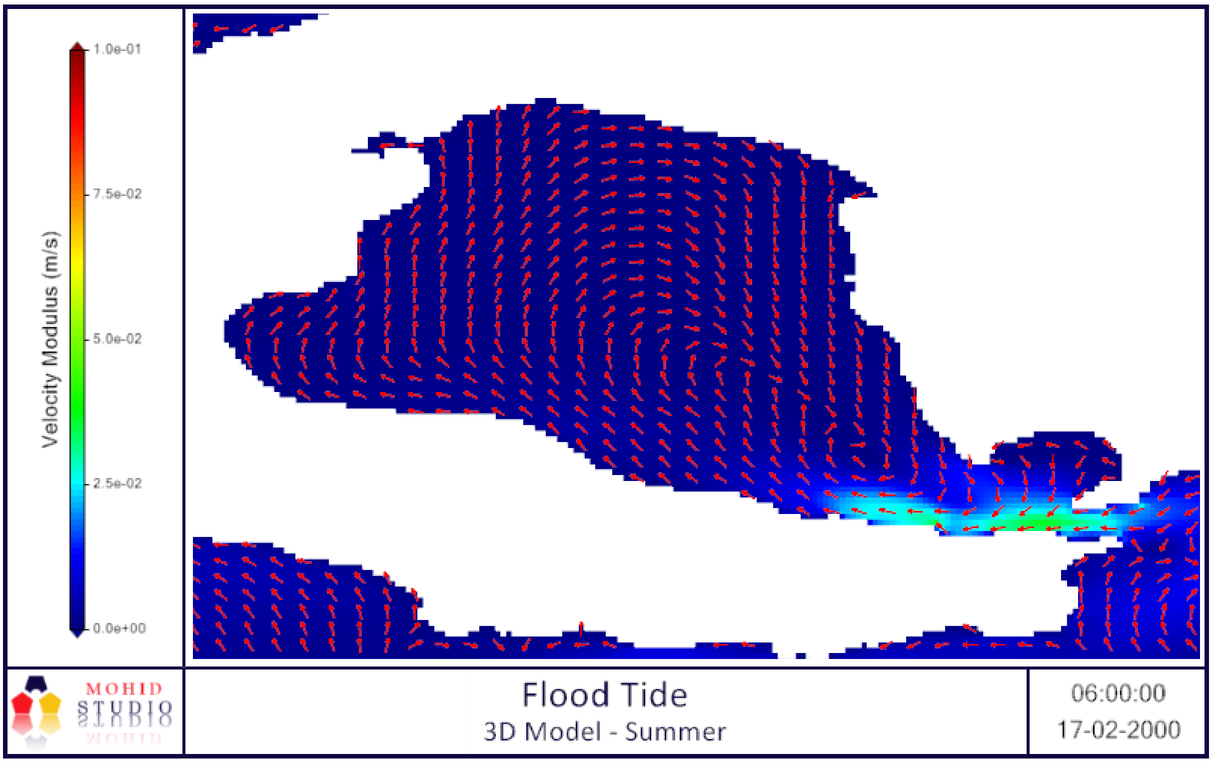

Figure 26 - 3D Model Flood Tide representation: Near the surface velocities.

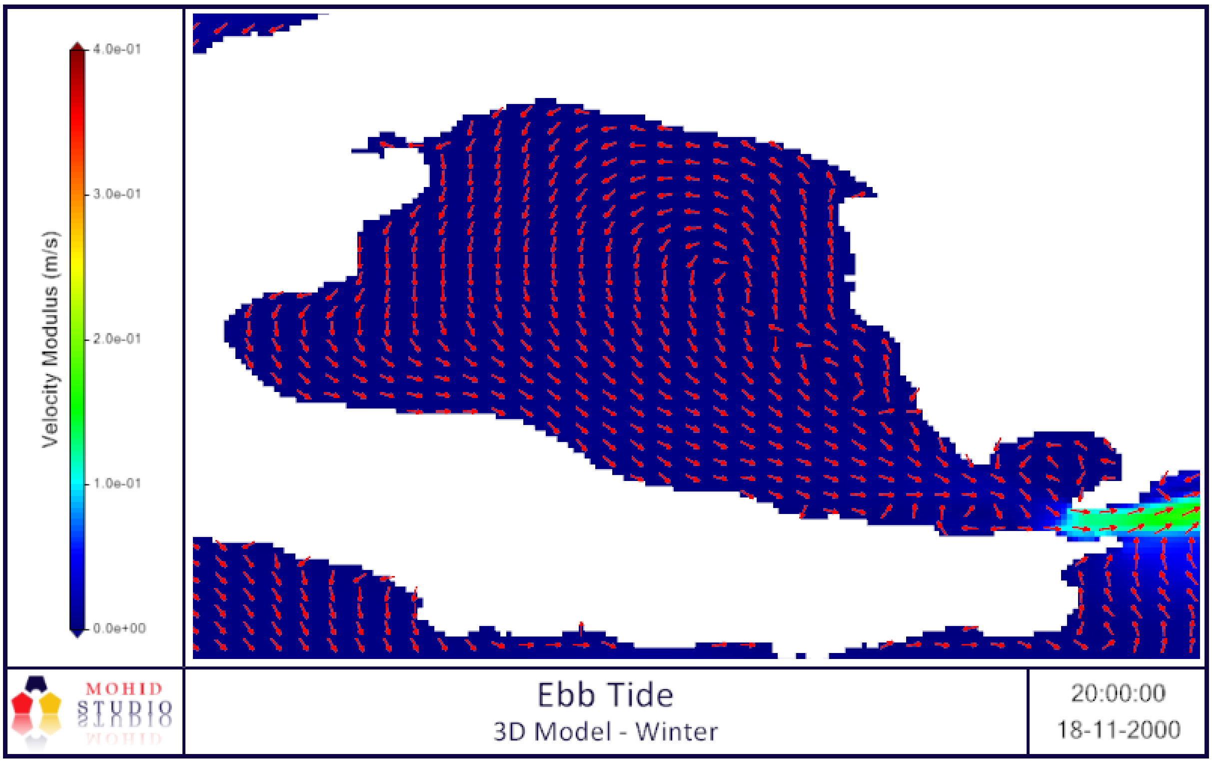

Figure 27 - 3D Model Ebb Tide representation: Near the surface velocities.

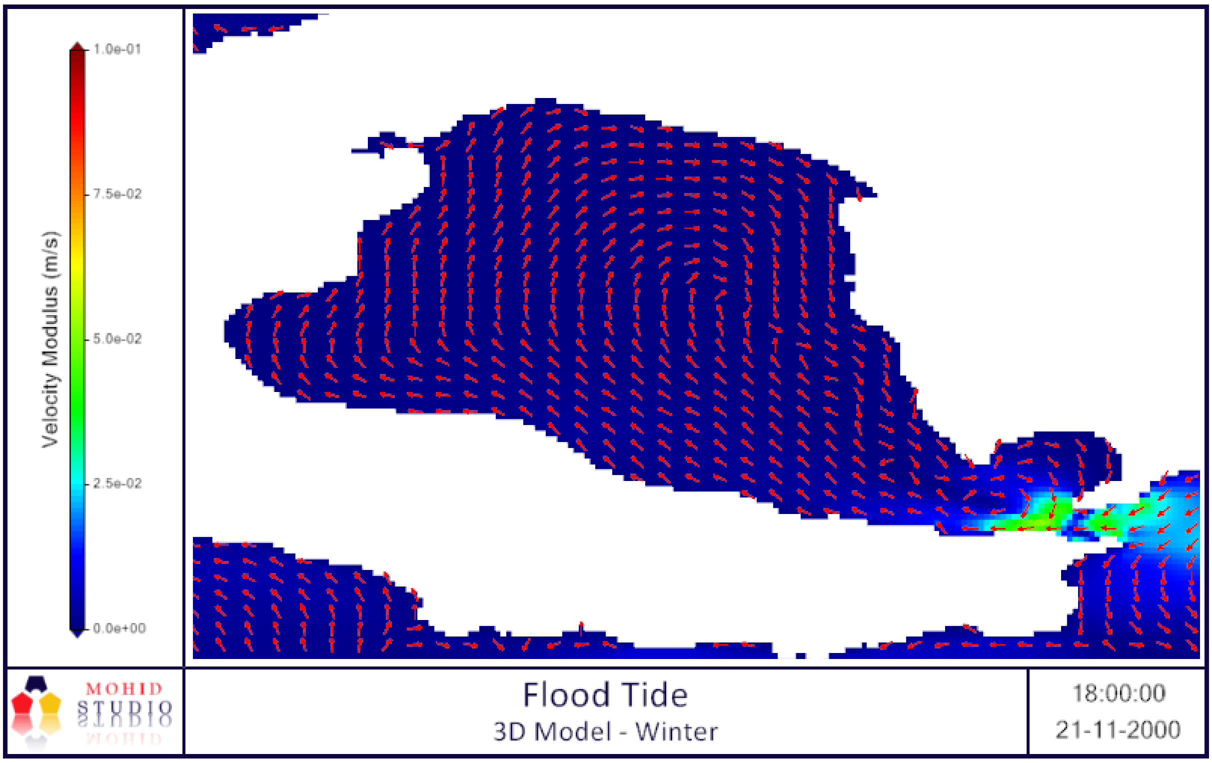

Figure 28 - 3D Model Flood Tide representation: Near the surface velocities.

5.1.2 Detailed Analysis

The following results describe a synoptic view over Port Foster dynamics. Two instants, one in the summer (February 2000) (Figure 29) and one in the winter (November 2000) (Figure 30) were selected for this purpose. The velocities presented are near surface, two meters below sea level.

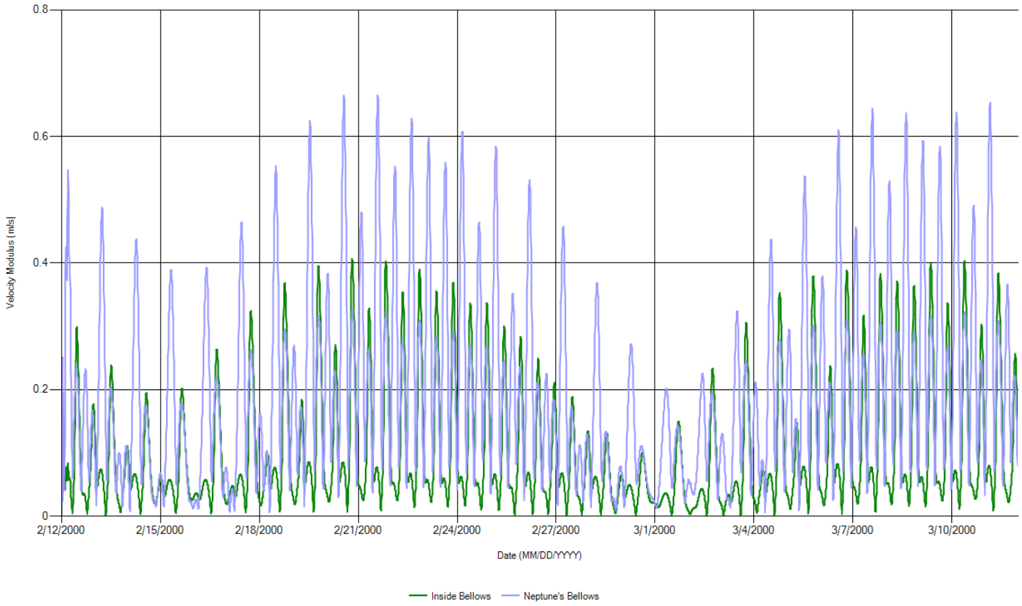

Figure 29 - Summer current velocities two meters below sea surface in two locations: Inside Bellows and Neptune's Bellows.

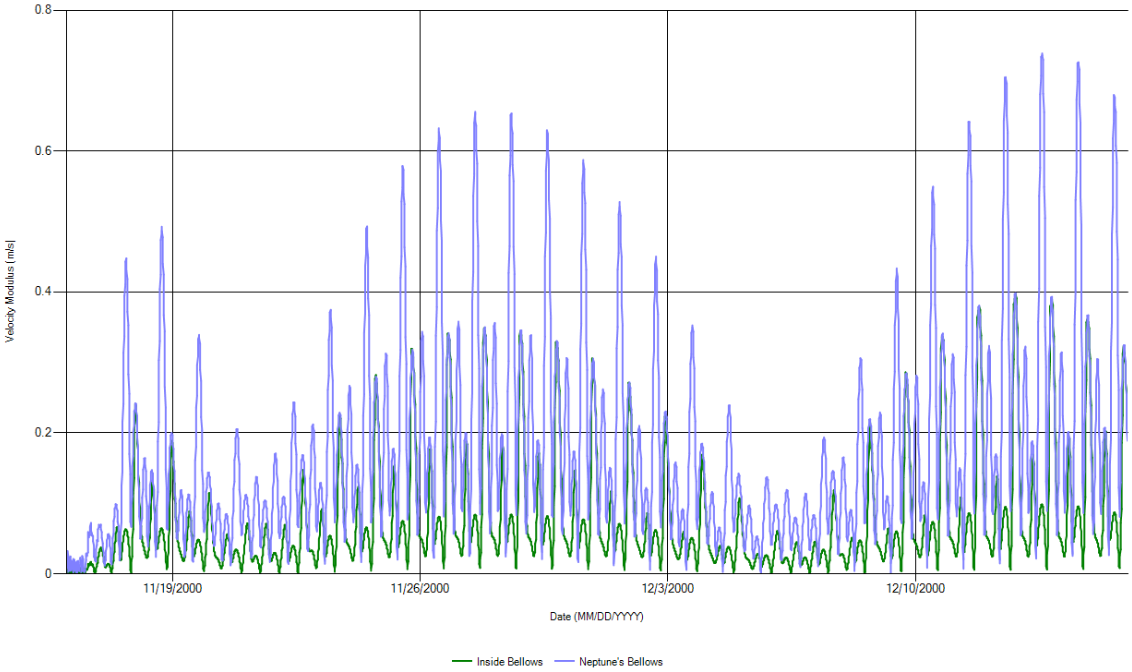

Figure 30 - Winter current velocities two meters below sea surface in two locations: Inside Bellows and Neptune's Bellows.

The velocities in both seasons vary similarly. In summer the stratification plays a major role, since the velocity Inside Bellows is sometimes higher then Neptune's Bellows velocities. Comparing the difference in amplitudes of the velocities between Neptune's and inside bellows, one can see that in summer this difference is smaller than in winter, concluding that in winter the velocities near the surface are affected by the water column mixture, slowing the tidal currents as they enter the bay.

Both winter and summer tidal currents are very similar in direction and velocity, however comparing the barotropic velocities with the ones from the 3D model, one can conclude that the stratification in Neptune's Bellows plays an important role in the currents velocity and direction, since the velocities, in general, have a slightly lower amplitude in the 3D model, visible in summer (Figure 31) and in winter (Figure 32).

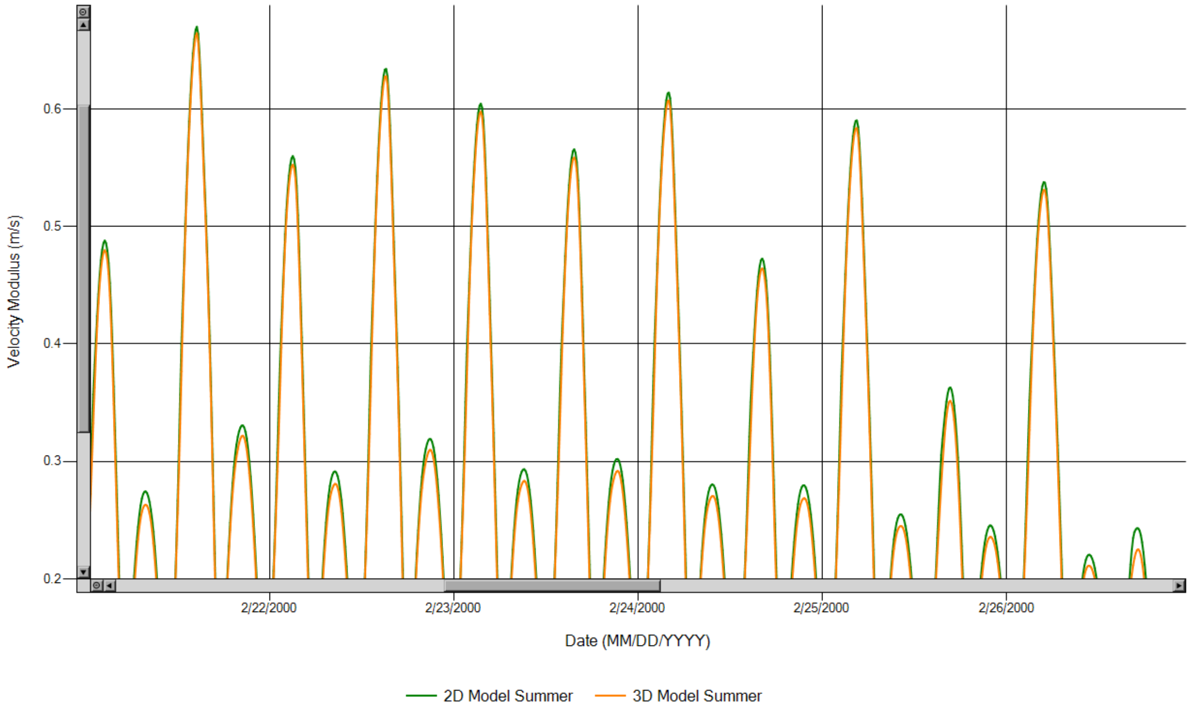

Figure 31 – Summer 2D and 3D model surface current velocities in Neptune’s Bellow’s.

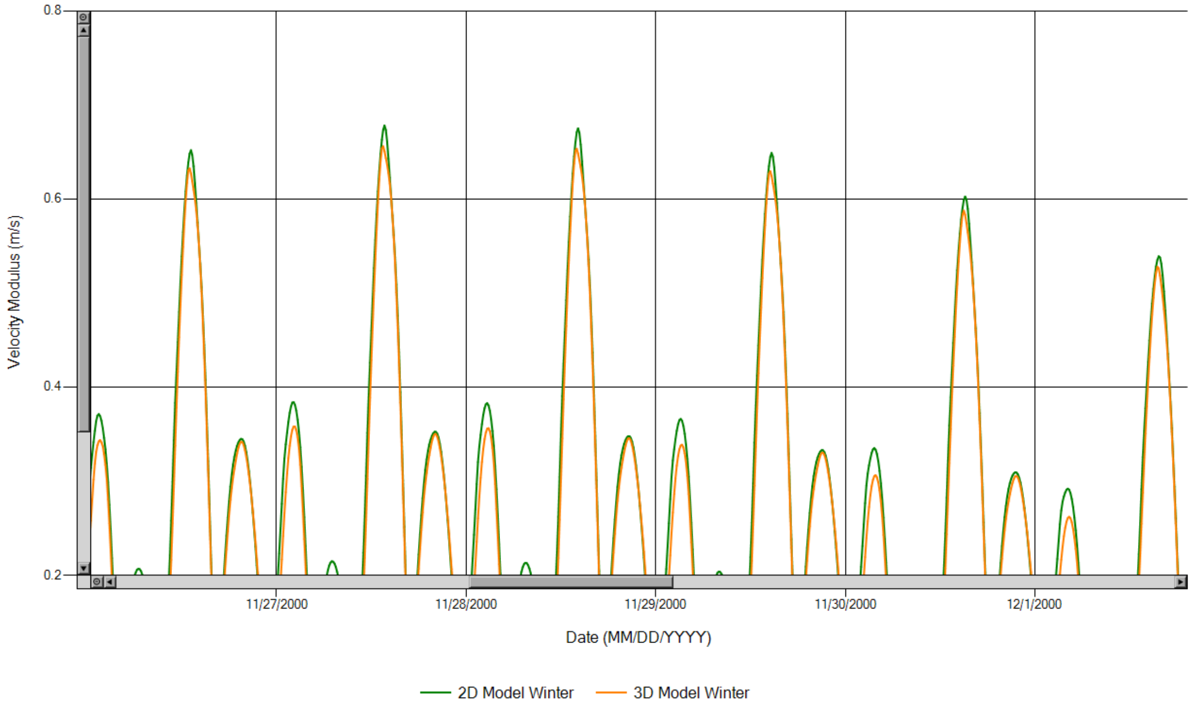

Figure 32 – Winter 2D and 3D model surface current velocities in Neptune’s Bellow’s.

Another place where it is clearly visible that the speed of the currents decreases from the 2D model to the 3D model is in Whaler's Bay (Figure 33 and 34).

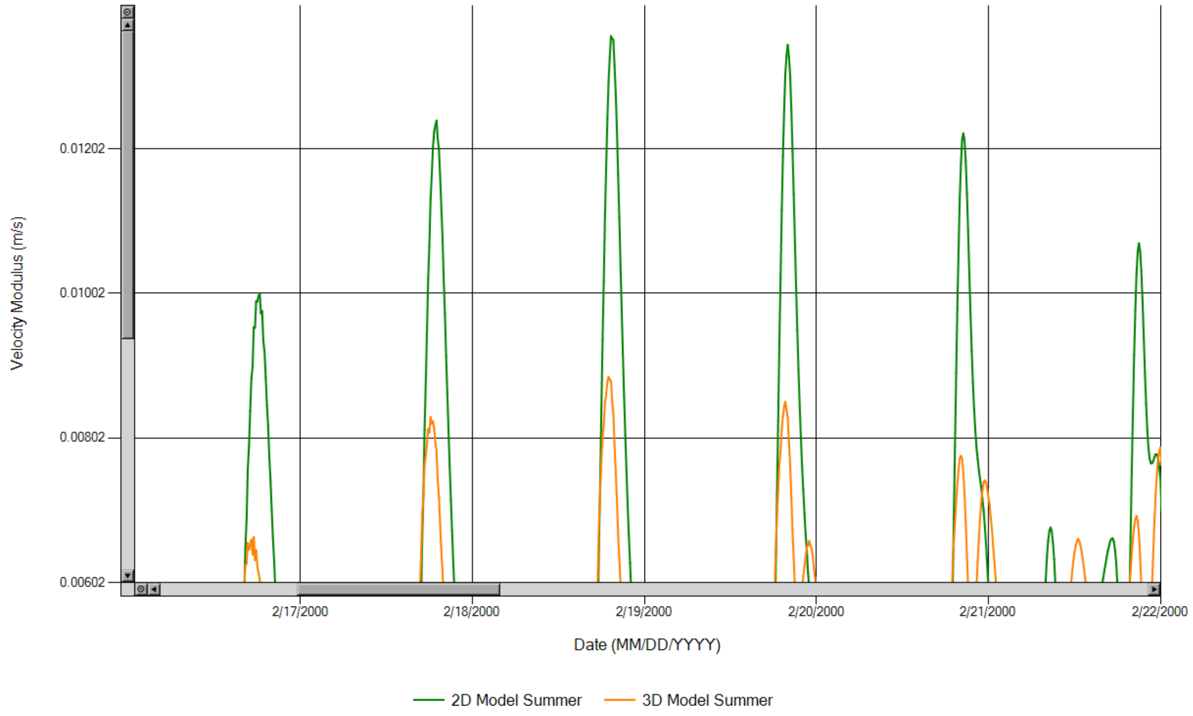

Figure 33 – Summer 2D and 3D model surface current velocities in Whaller's Bay.

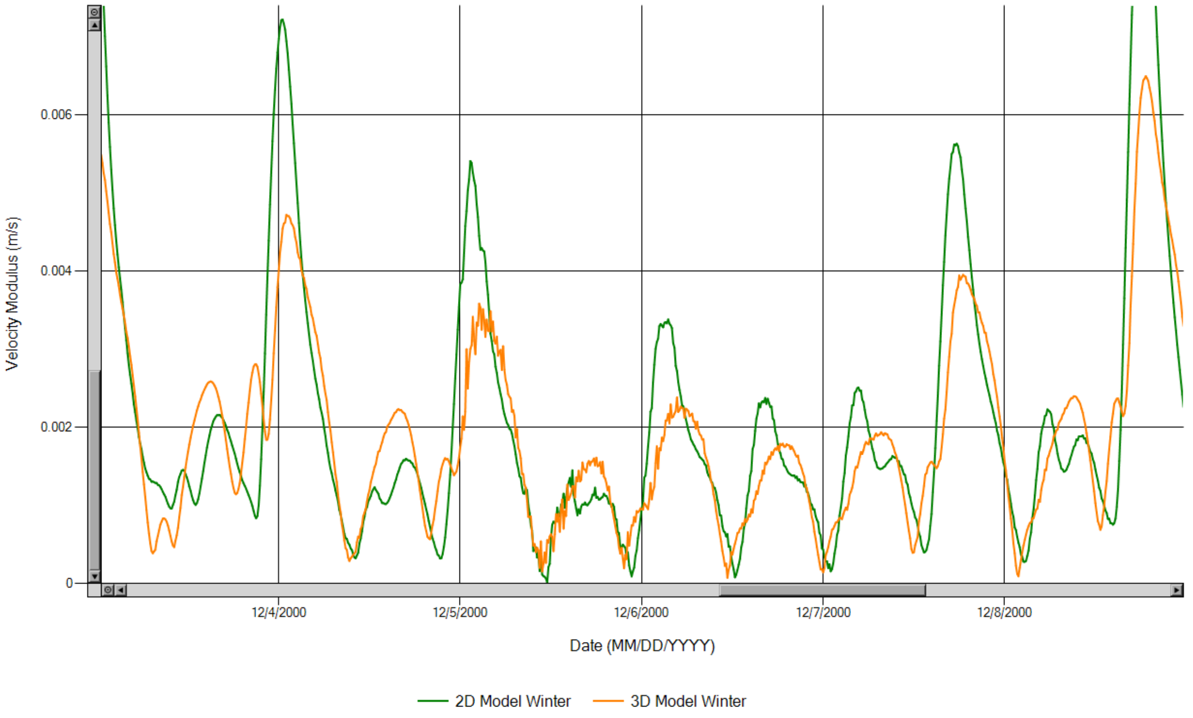

Figure 34 – Winter 2D and 3D model surface current velocities in Whaller's Bay.

Other locations, however, show that in general the amplitude of the velocities increased from the 2D model to the 3D model, as for example in Colatina (Figure 35 and 36).

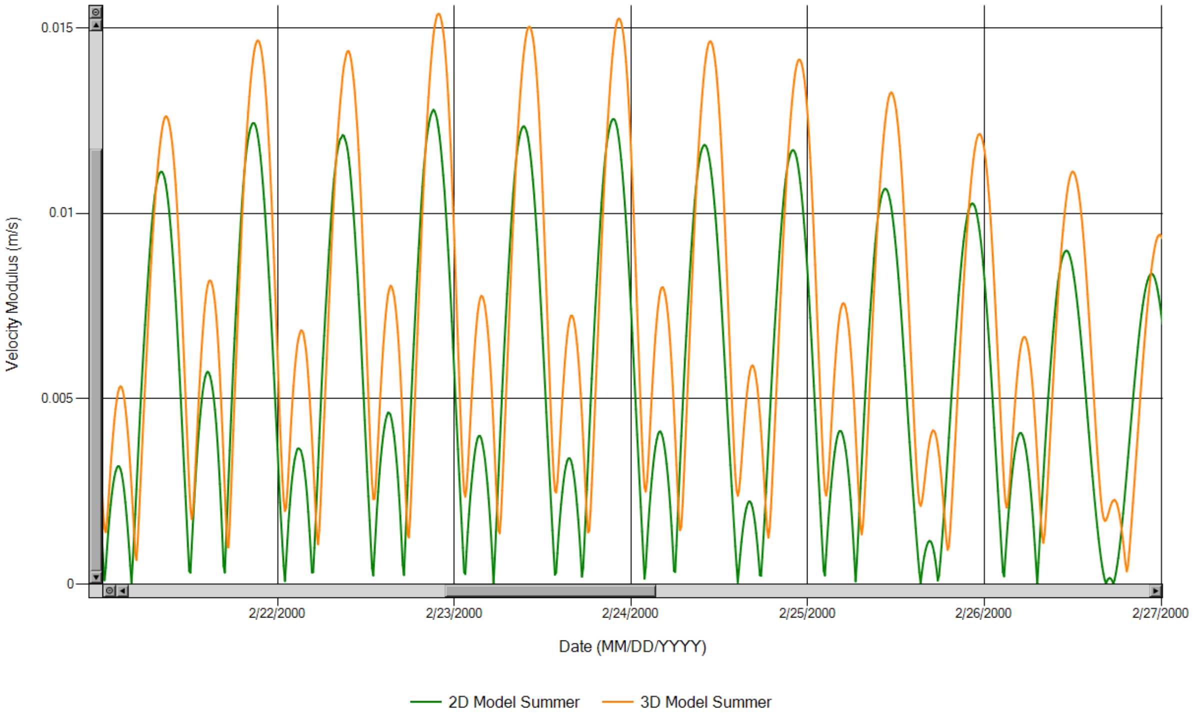

Figure 35 – Summer 2D and 3D model surface current velocities in Colatina.

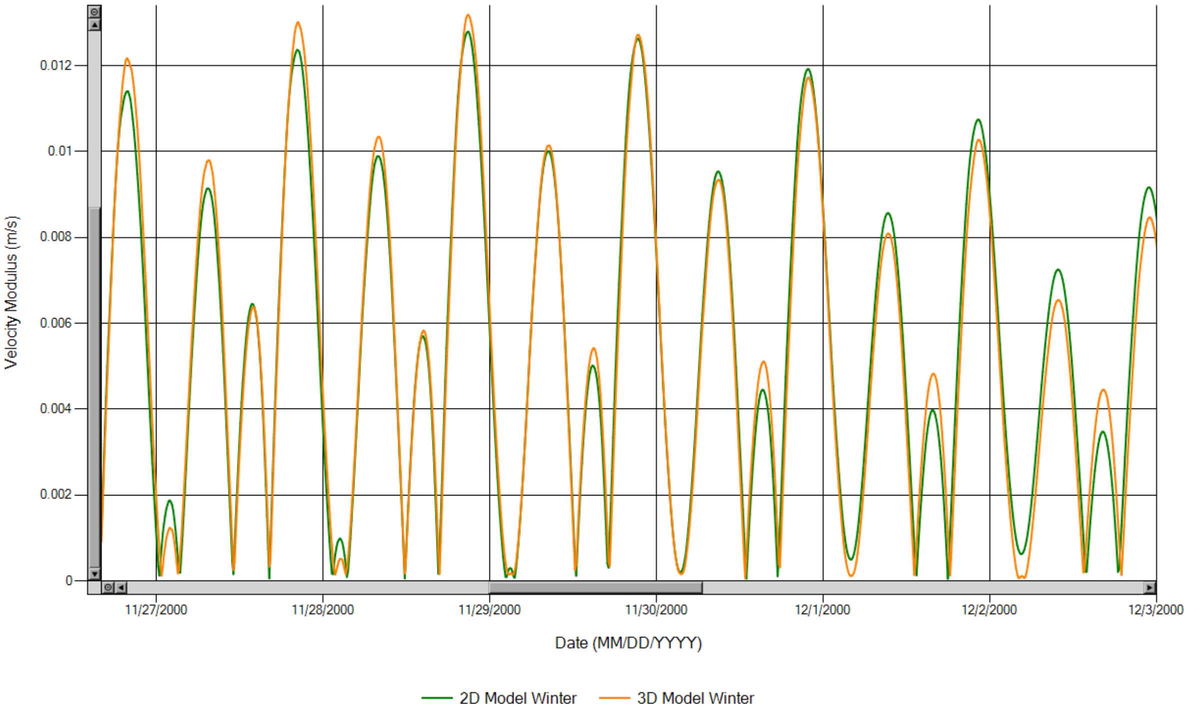

Figure 36 – Winter 2D and 3D model surface current velocities in Colatina.

The velocities near the bottom in all locations, except Neptune's Bellows, are close to zero meters per second. Other results also show that the velocities nearly didn't change in the center of Port Foster. The outputs for 1 month simulation for the results presented above can be consulted in the annex (Annex D).

Although the direction Inside Bellows is slightly different in both seasons when compared with the 3D model (Figures 37 and 38), one can conclude that stratification has more impact in summer than in winter, since in summer (Figure 38) there's an increase in the events registered near the surface.

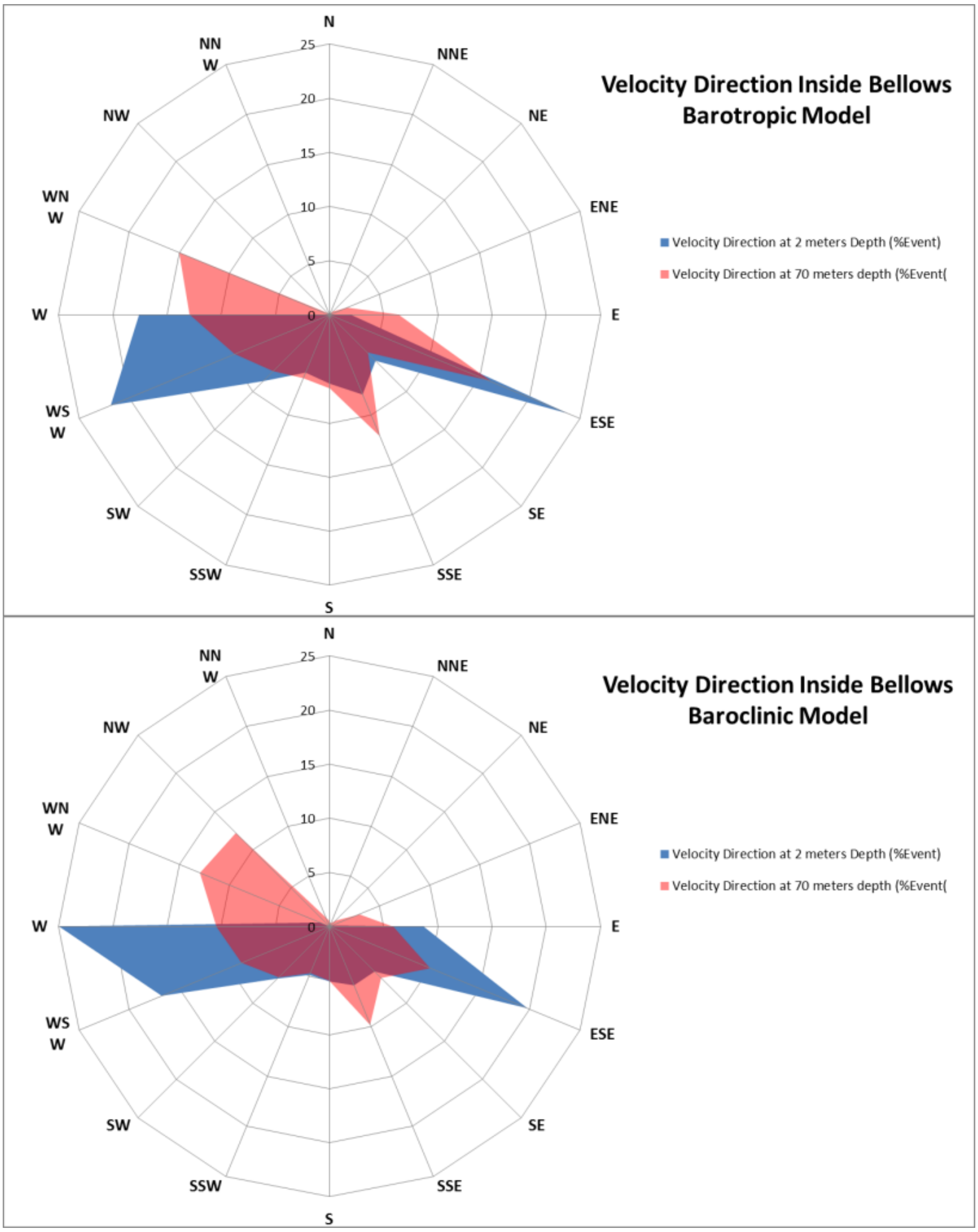

Figure 37 - Winter 3D velocity direction and magnitude Inside Bellows.

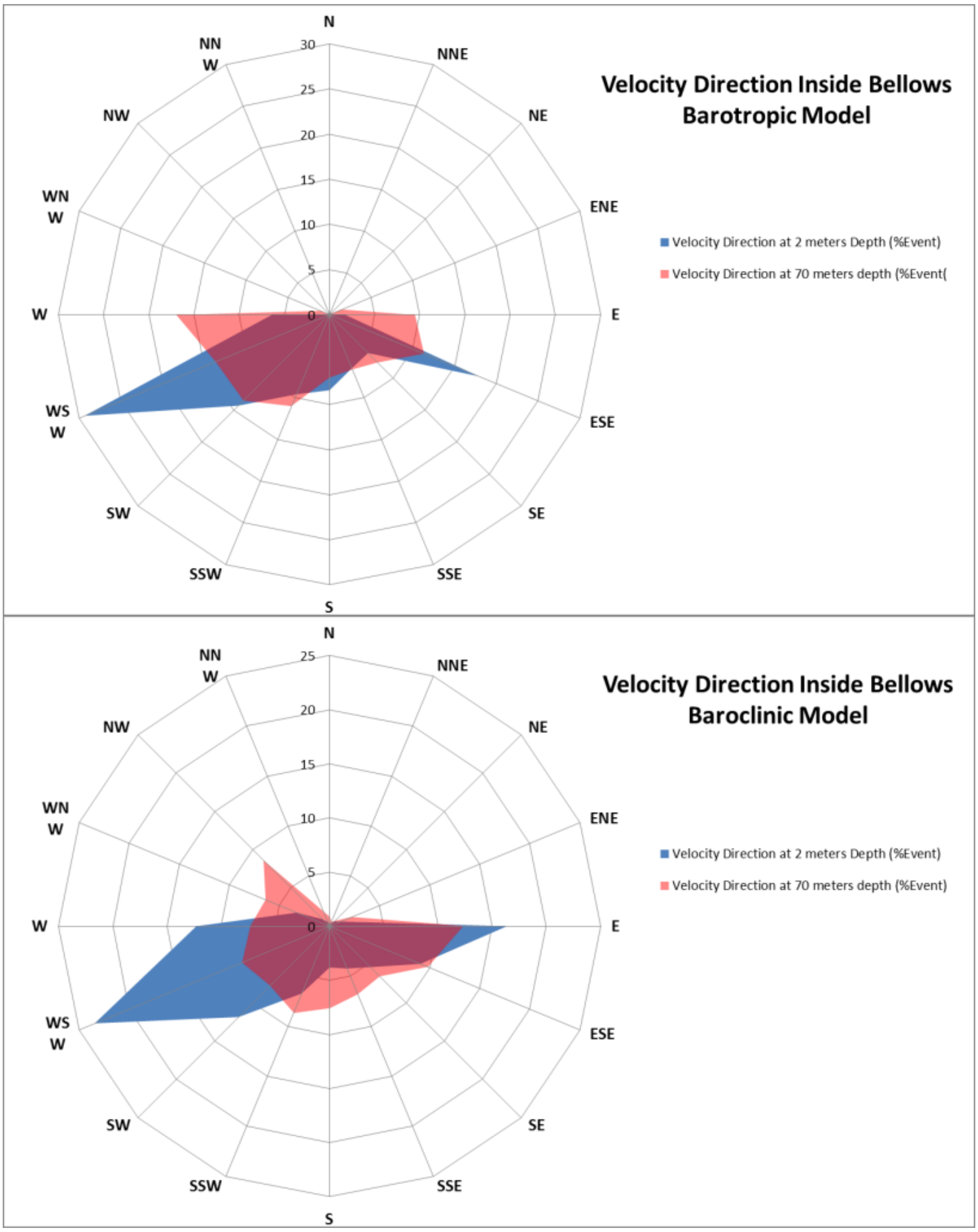

Figure 38 - Summer 3D velocity direction and magnitude Inside Bellows.

In another analysis, the Brunt-Väisälä frequency, also known as stratification frequency, was depicted for summer and winter inside Port Foster. The frequency quantifies the importance of stability, and it is a fundamental variable in the dynamics of a stratified flow. The thermocline (locations with a sharp change in temperature) in summer is located between 10 and 20 meters (Figure 39), while in winter is not really present, since the water column is well mixed (Figure 40).

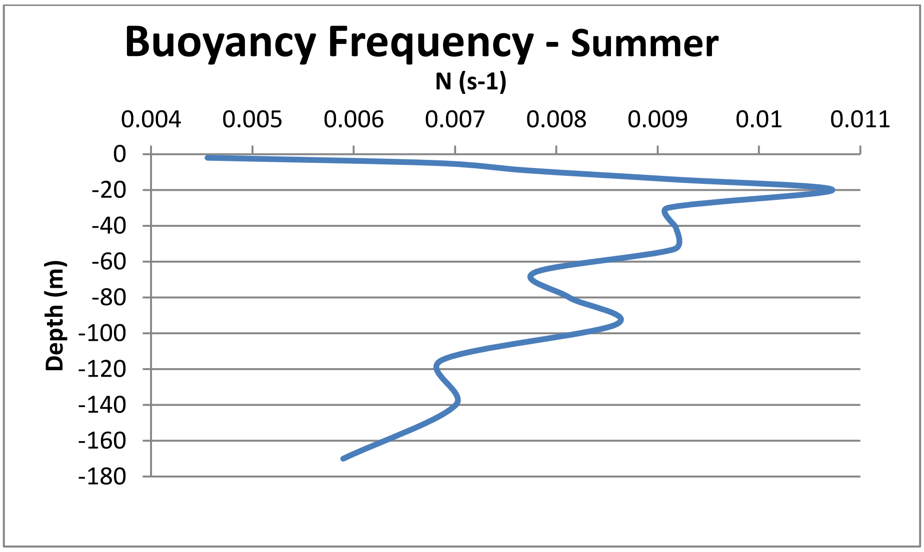

Figure 39 - Summer buoyancy frequency inside Port Foster.

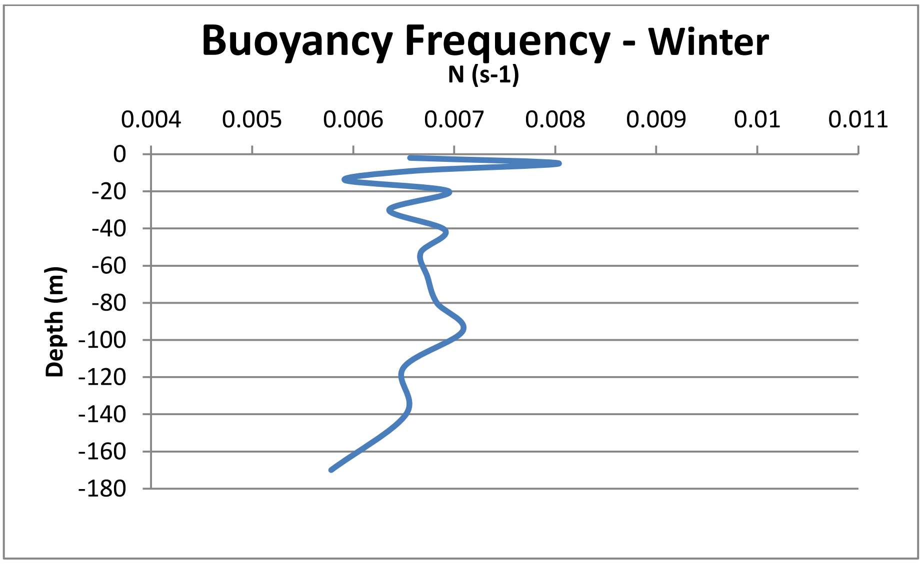

Figure 40 - Winter buoyancy frequency inside Port Foster.

Knowing the location of the thermocline is useful for future analysis, since it’s the most likely location for the generation of internal waves. Another important conclusion is that particles, such as mercury, are expected to stay above the thermocline in the summer because of the stratification. In winter, since the water column is well mixed they’re expected to be dispersed in the water column.

M2 Component

The M2, with the S2, O1 and K1 are responsible for more than 90% of the tidal energy. The M2 component can be also associated with the generation of internal tides in Neptune's Bellows (black rectangle depicted bellow, Figure 41 and 42).

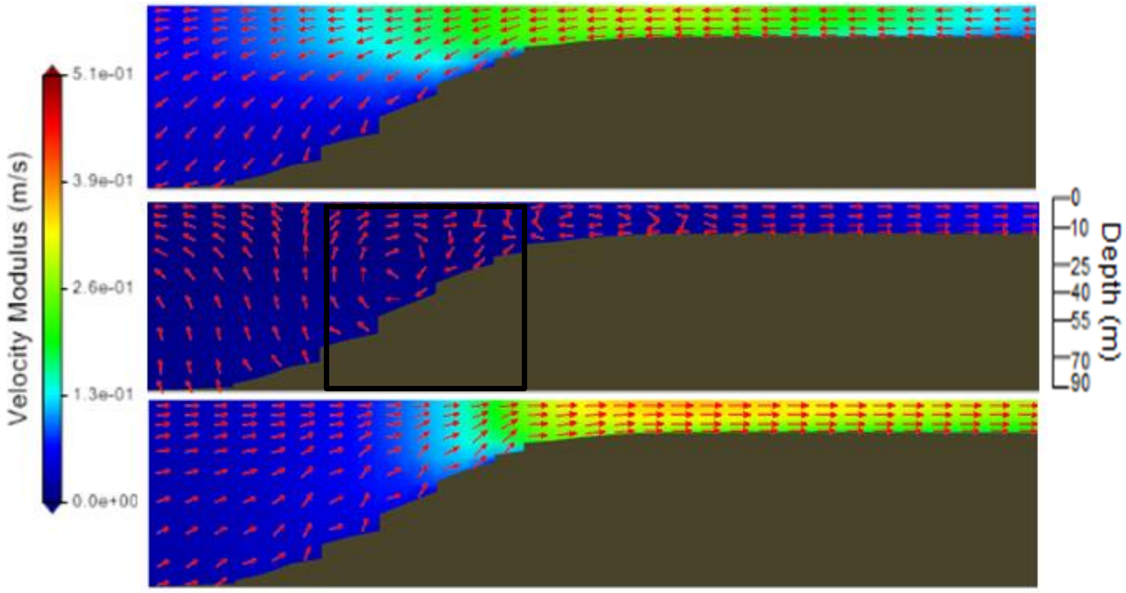

Figure 41 – Winter Tidal Velocity of the M2 component in Neptune's Bellows.

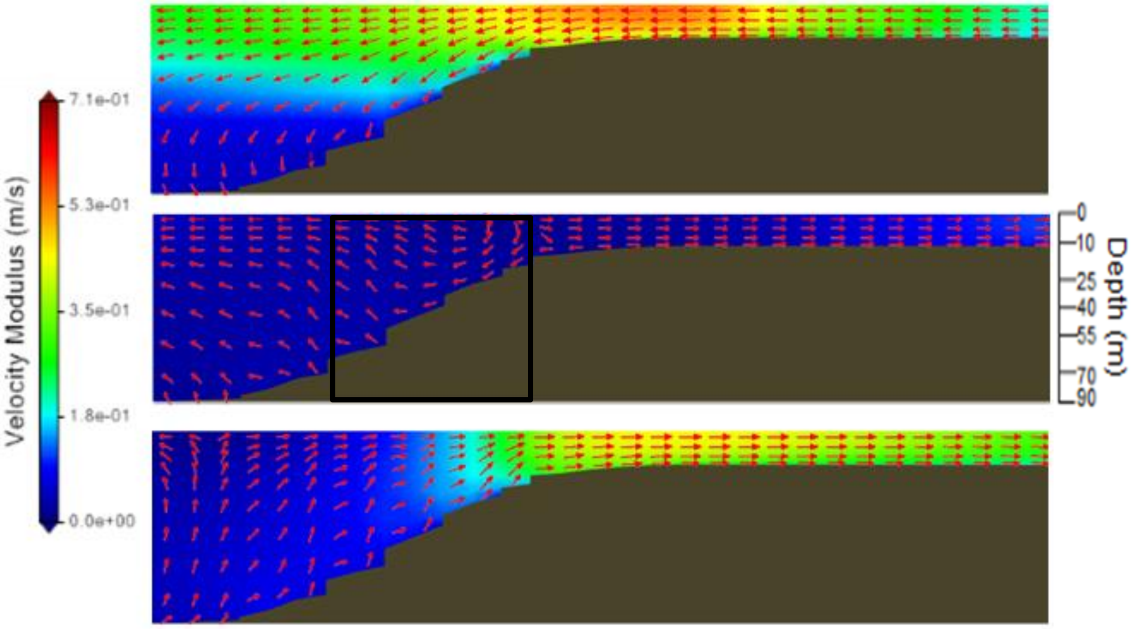

Figure 42 – Summer Tidal Velocity of the M2 component in Neptune's Bellows.

5.1.3 Internal Tides

In the study of internal tides it was important to know if they could be formed during Summer and Winter, and which components were most likely associated to its origin. As mentioned in 2.2.4 the frequency band for internal waves propagation is between the Coriolis and Buoyancy frequency, therefore the components that can be associated with internal waves generation in Neptune's Bellows are the ones above the black line plotted in Figure 43 (depicted from table 5 presented in Annex E).

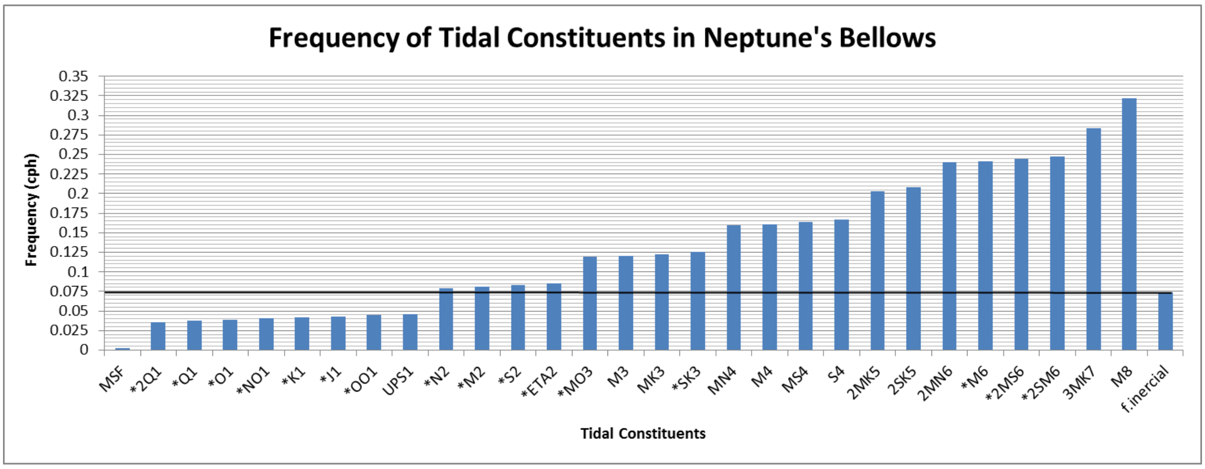

Figure 43 - Frequency of the tidal constituents in Neptune's Bellows.

An indication of the potential generation sites of internal tides, has well has the more important components related to their appearance, can be deduced from the linear internal wave theory, whereby the bottom slope (bs) is compared with the slope of the internal wave characteristics (c), as defined by (Baines 1982; Craig 1987):

$$c^2 = \frac{w^2 - f^2}{N^2 - w^2} \tag{13}$$

Where$f$, N, and w are the inertial, Brunt-Väisälä, and tidal frequencies, respectively.

Regions where the ratio α between bs and c is equal or higher than 1 are likely sites for internal tide generation. Where the ratio α is less than 1, it is not to be expected that internal tides should be generated. If α = 1, the internal tide generated will propagate along slope and if α > 1, it will propagate in an offshore direction (Pereira & Castro 2007).

The following graphs (figure 44, 45 and 46) depict the results using the approach mentioned above. The location is Neptune's Bellows, for both winter and summer situations. The components presented (M2, N2 and SK3) were the ones mentioned by Lenn et.al. (2003).

- **M2**

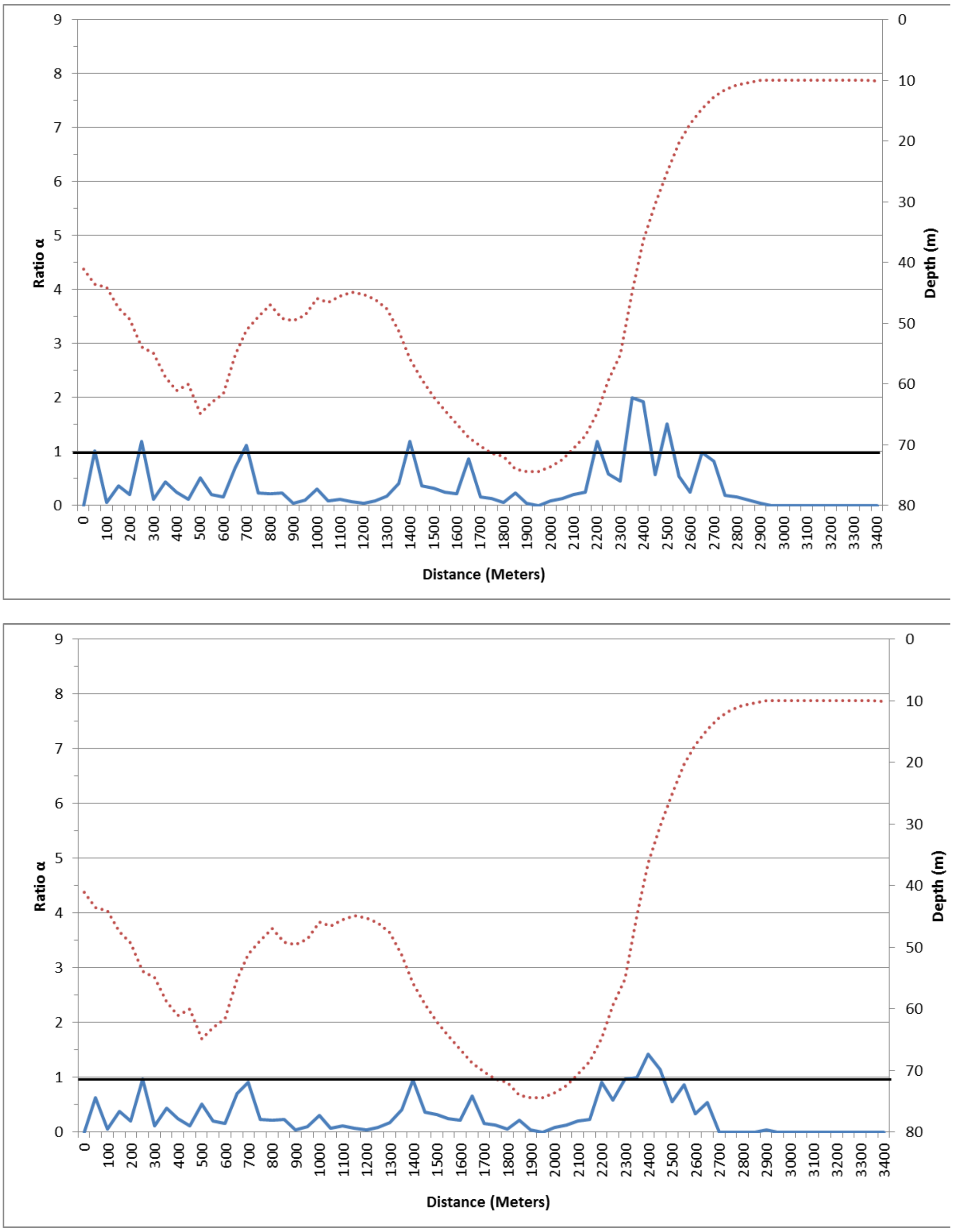

Figure 44 - Ratio α in blue, for summer (top) and winter (bottom) situations taking into account the M2 component at Neptune’s Bellows. The orange dotted line represents the bathymetry.

- **N2**

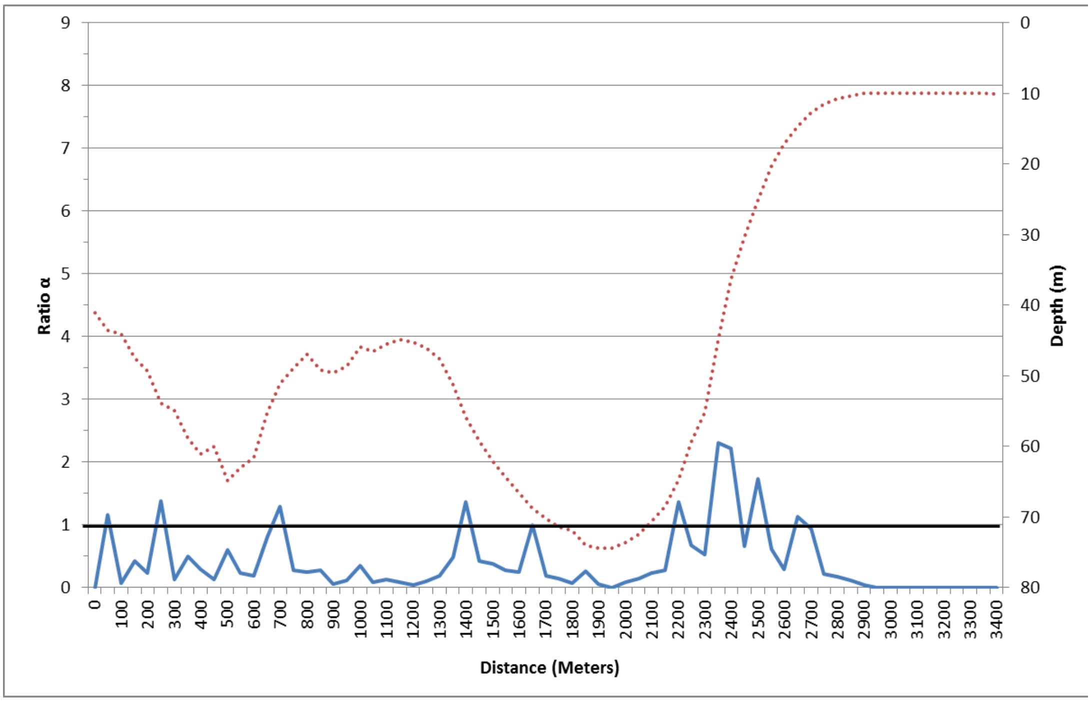

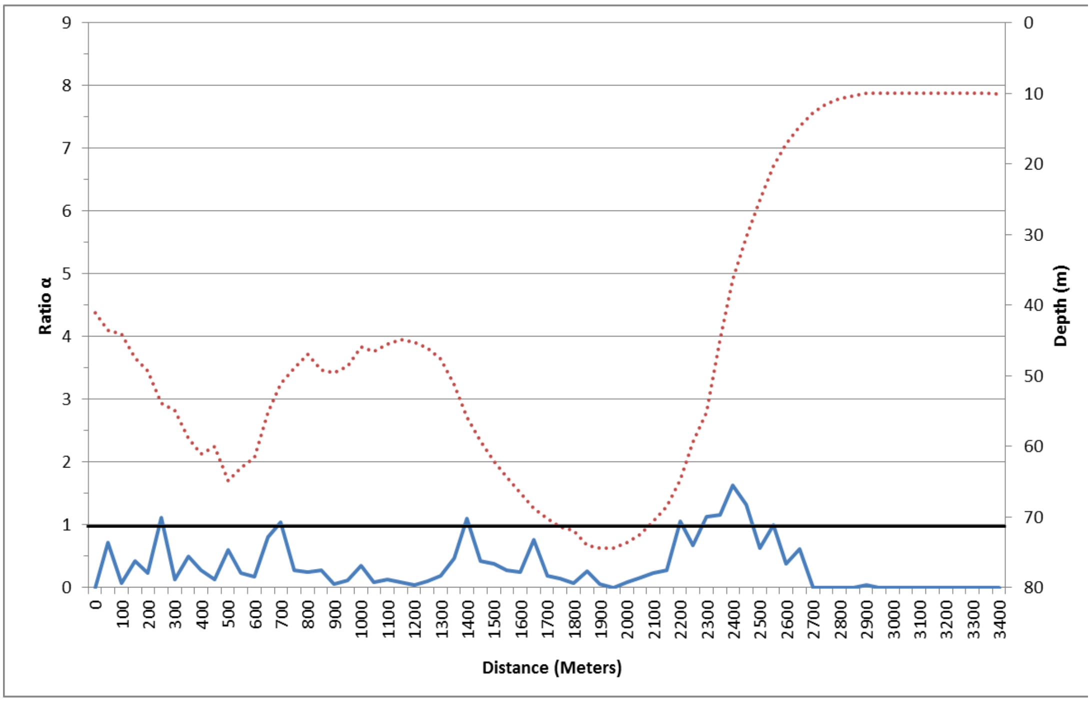

Figure 45 - Ratio α in blue, for summer (top) and winter (bottom) situations taking into account the N2 component at Neptune's Bellows. The orange dotted line represents the bathymetry.

- **SK3**

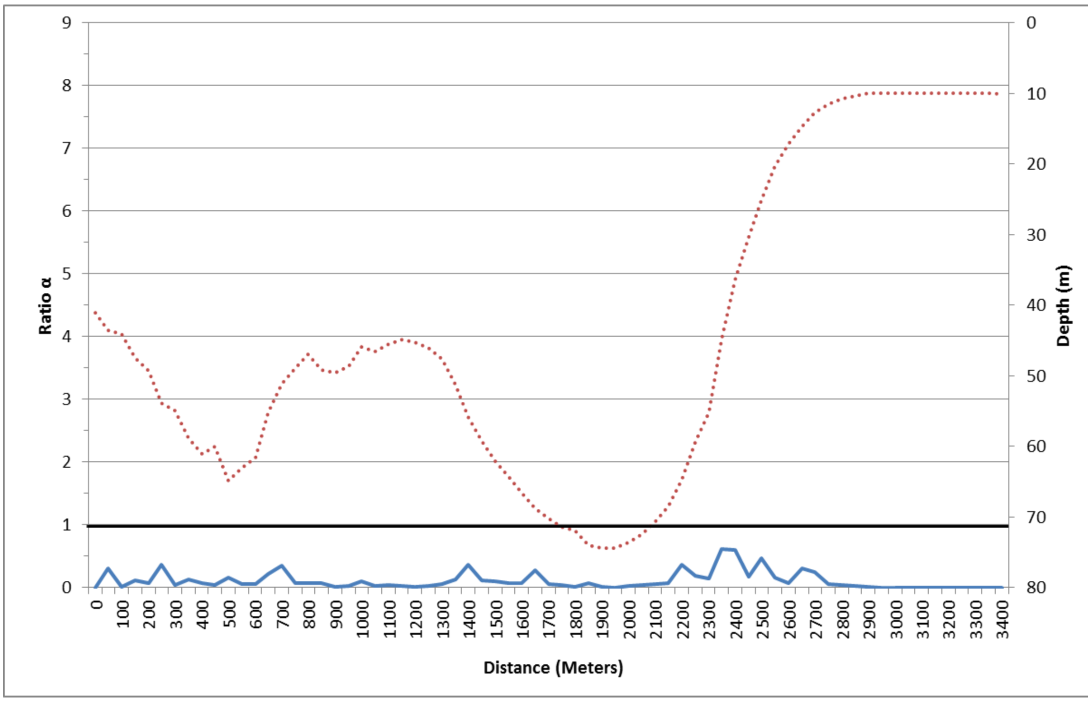

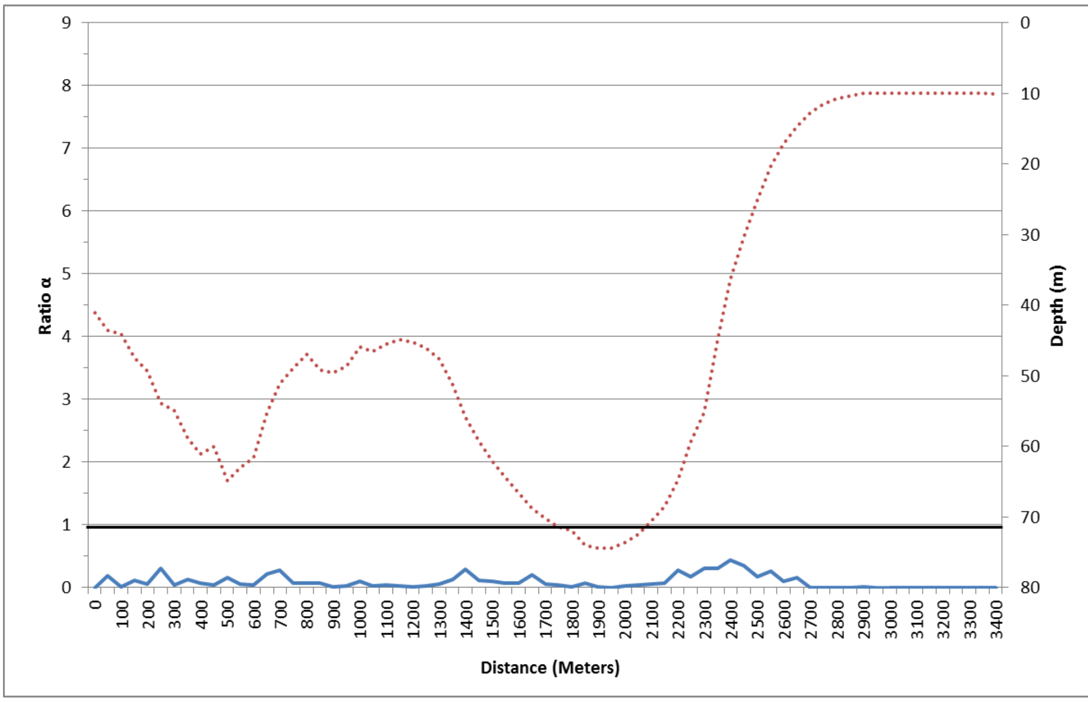

Figure 46 - Ratio α in blue, for summer (top) and winter (bottom) situations taking into account the SK3 component at Neptune's Bellows. The orange dotted line represents the bathymetry.

From figures 44 and 45, one can conclude that internal tides can be generated in summer and also in winter, due to temperature and salinity stratification, respectively. Other interesting aspect is that the components that have a higher period (M2 and N2), more close to the Coriolis frequency, were the ones that showed better potential to internal tides generation. Lastly, looking at figure 46, the SK3 component can be discarded since it has no influence.

5.1.4 Wind Results

Although the wind forcing was not applied in the model, the results from the wind roses are shown (figure 47).

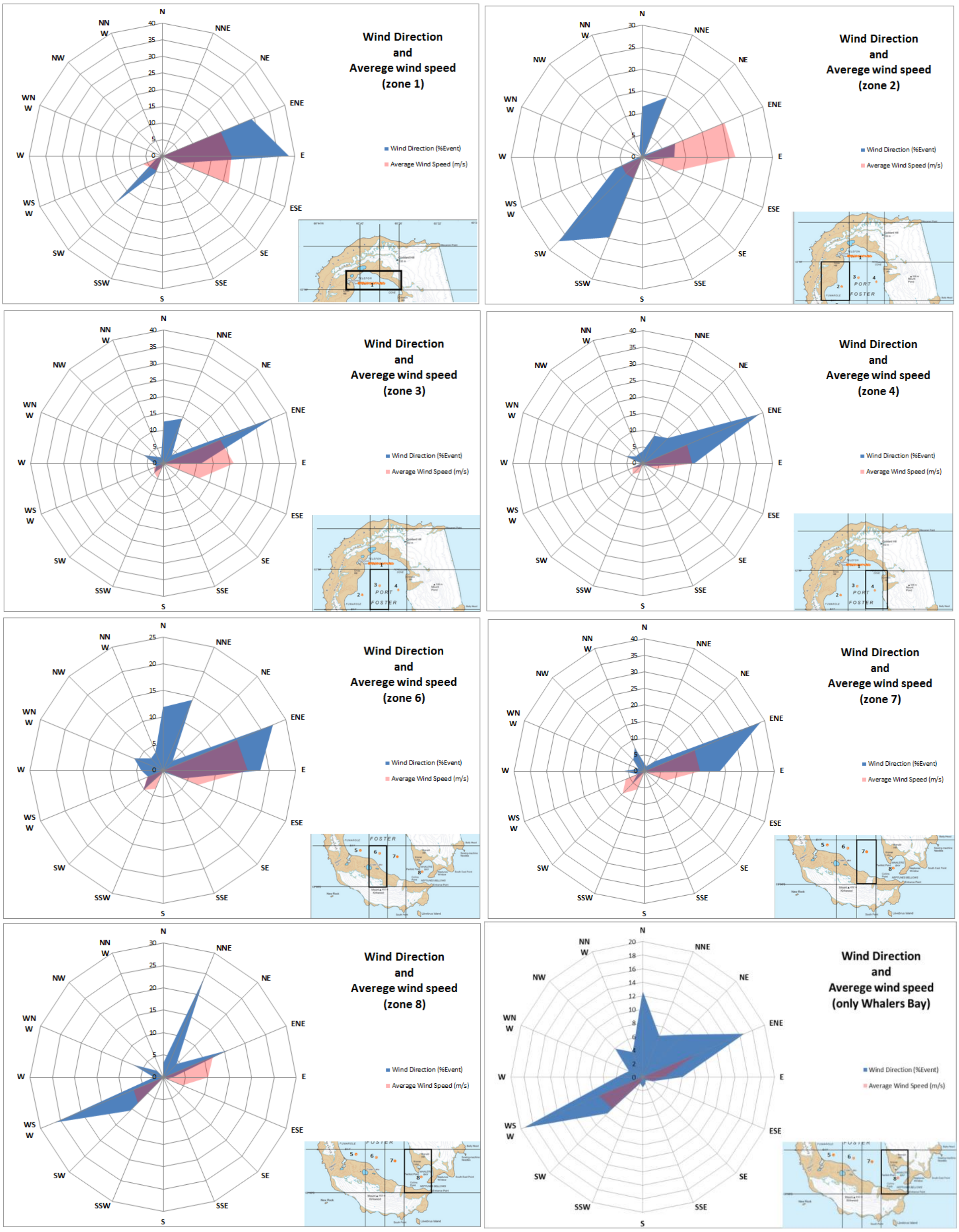

Figure 47 - Wind roses for Port Foster.

From figure 46, the conclusion that the topography has a major effect in how the wind circulates inside Port Foster can be confirmed, as well as the need of a microscale wind model to accurately apply the winds in the 3D model.

The results are more in agreement with the predominant winds detected at the Terrestrial Station (NE and SW), then those observed at Bellingshausen Station where the predominant direction is from W and NW.

5.2 Mercury Circulation

One of the main objectives of this work was too see how the tide influences the particles circulation within the bay and wheter the stratification plays a important role in their dispersion. The initial position of the lagragean tracers is presented in figure 48. The particles were released near sea surface.

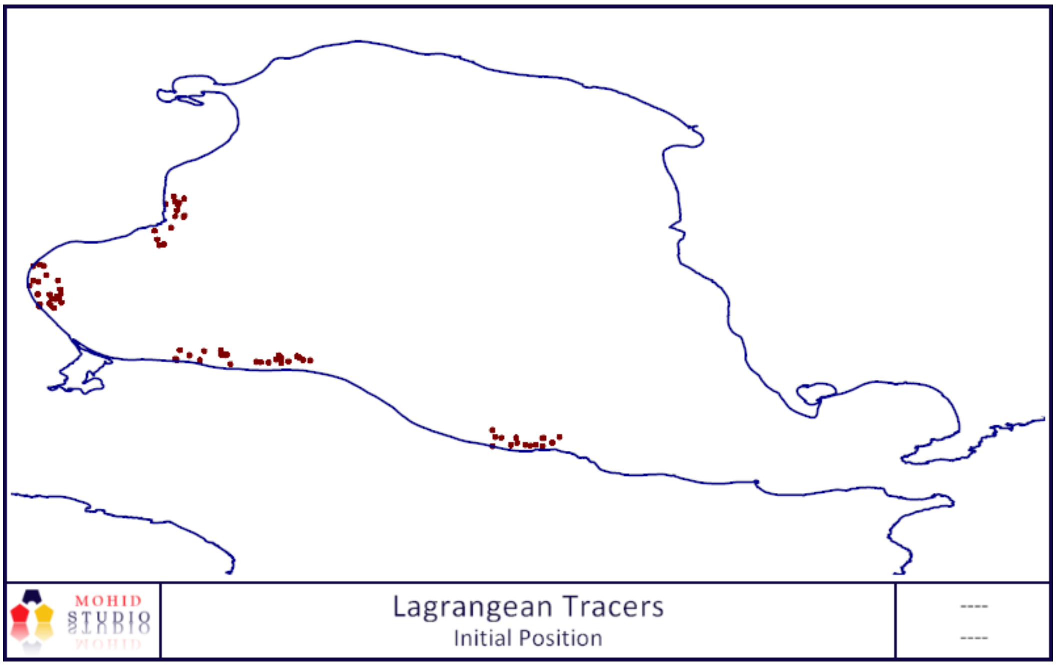

Figure 48 - Initial Position of the lagrangean tracers.

After one month simulation, the conclusions are that there is a poor rate exchange of water between Port Foster and the surroundings, the particles tend to accumulate in the west to north part of the bay due to the fact that the velocities gradually decrease from Neptune's Bellows to that region. The stratification as an effect on the residence time, since more particles were released when comparing the two outputs (figures 49 and 50). This result also shows that, notwithstanding the current velocities decrease in some areas from the 2D to the 3D simulation, in general the current velocities increased due to the stratification.

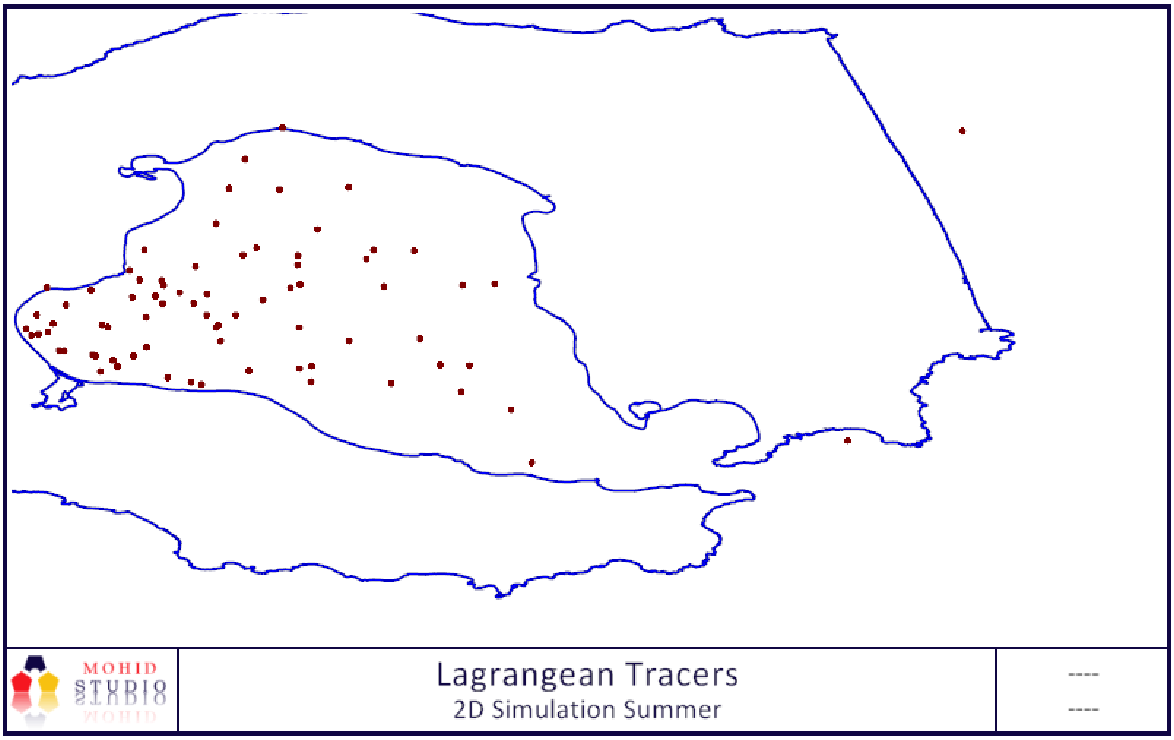

Figure 49 - 2D Model: Lagrangean tracers position after one month simulation.

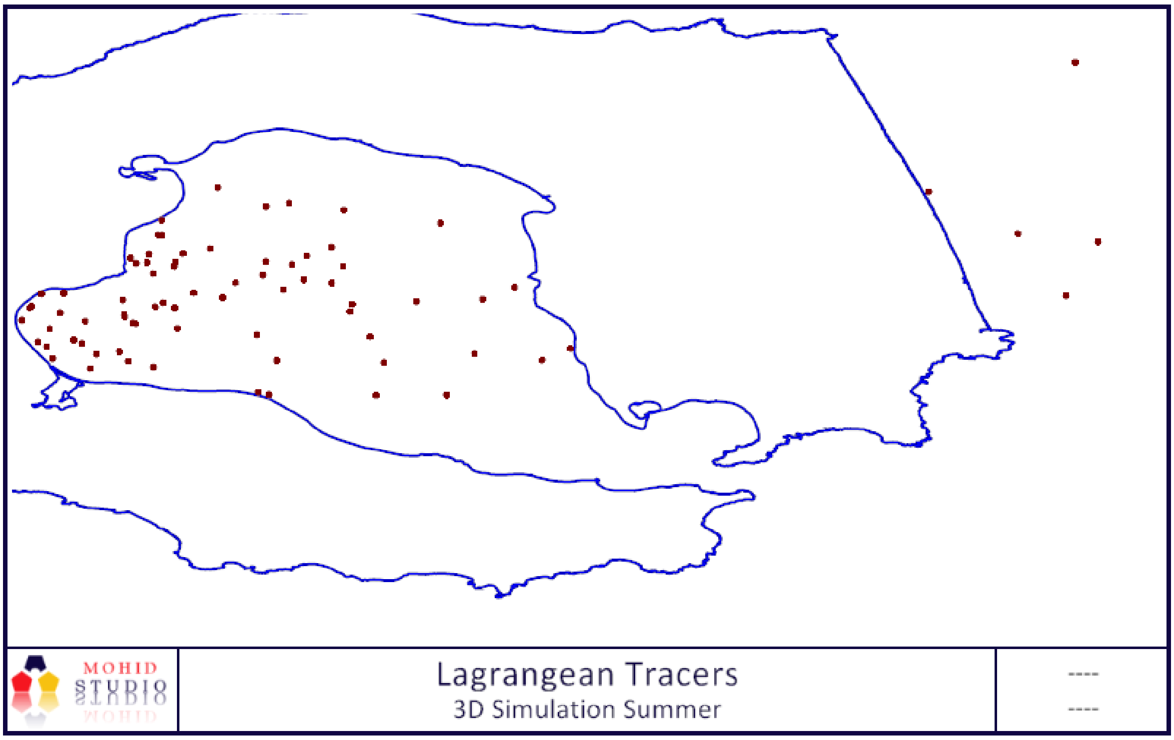

Figure 50 - 3D Model: Lagrangean tracers position after one month simulation.

A sequence of images from the output of the lagragean tracers simulation on the 2D Model can be consulted in annex (Annex F).

6. General Discussion

6.1 Conclusions

Deception Island is a place with many features still to be studied and one of them is the bay hydrodynamics. It was brought to attention that there has been an increase in some trace metals concentrations within the bay and no study has so far taken into account the sources, fluxes, pathways and bioavailability of mercury in Port Foster's ecosystem. The modelling exercise enables one to measure, predict and study changes of the system, therefore confirming published results and also contributing with new information.

The tidal model was validated with success, although a statistical analysis between the model results and the data collected by other researchers would also reinforce this validation. This analysis was not performed since the raw data was not available to be used. The hydrodynamic 2D Model also confirms known findings. The general circulation inside Port Foster is presented, showing the variation in water level, the ebb/flood tides and the residence time, with this one only taking into account tidal velocities and not the stratification within the bay.

A 3D simulation was performed. To the best of our knowledge, such analysis was never done before. A 3D simulation that takes into account the tides, the T-S profiles, radiation and winds is imperative, since in previous studies, questions were made about how elements circulate within the bay, what is the rate of accumulation of mercury and if the ecosystem is facing a rising threat.

The 3D model presented in this work only takes into account the fluid stratification, since the temperature and salinity profiles were considered steady. Due to the absence of data, the model couldn't be validated, limiting its ability to make predictions and allowing only to study processes.
Stratification played a bigger role in the summer, affecting both the magnitude of velocities and the direction of tidal currents to a lesser degree. In the winter, however, it only affected the magnitude of the velocities.

There's a strong evidence of the generation of internal waves in Neptune's Bellows in both seasons. The impact of the energy released in this process in Port Foster's water column is yet to be assessed. The M2 and N2 are the two main tidal components related to this phenomenon.

One of the most important findings is that Port Foster presents a large residence time, of almost 1.7 years. This finding, plus past studies with almost the same value, proves that the bay is a propitious place for mercury accumulation, therefore being a rising threat to the local ecosystem. Lagrangean tracers confirmed this conclusion.

On the many difficulties encountered one has to mention the availability and reliability of data, since the wind data available was proven to be not very reliable and the radiation data was scarce, preventing the application of these fluxes of energy and momentum in the model. Moreover, this was the first time the model was applied in the Antarctic region being somewhat a test to its robustness.

Although the complete model implementation was not finished, on the whole the objectives of the thesis were achieved, therefore creating the first step for a future full understanding of the bay hydrodynamics.

6.2 Future Proposals

Since this was the first application of the model in the Antarctic region, there is an important improvement that was noticed to be missing in MOHID, which is the inclusion of freezing and therefore the exchanges between solid and liquid water. This didn’t affect the 3D model, because due to the salinity water only freezes near -4°C.

To improve the model in the future, reliable data is needed. It is important to collect wind data in situ near the sea level and also hourly solar radiation. To improve the model it is important to know the precise location of the hot water sources in the bay and their influence in the temperature and salinity profiles.

For a future study of the internal tides impact on the water column and their visualization a non-hydrostatic simulation has to be done since the hydrostatic hypothesis is not valid in internal waves. Although MOHID already as an option for non-hydrostatic simulation, this option is only for schematic cases and therefore has to be improved.

References

Ahn, I. Y., Lee, S. H., Kim, K. T., Shim, J. H., Kim, D. Y. (1996). Baseline heavy metals concentrations in the Antarctic clam Laternula elliptica in Maxwell Bay, King George Island. Antarctica. Mar. Pollut. Bull. 32, 592 – 598.

Arnaud, P. M., Ramos-Espla, A. A., Ramos, A., Lopez, C. M., Olaso, I. & Ramil, F. (1998). Semi-quantitative study of macrobenthic fauna in the region of the South Shetland Islands and the Antarctic Peninsula. Polar Biology, 19, 160–166.

Arntz, W. E., Brey, T. & Gallardo, V. A. (1994). Antarctic zoobenthos. Oceanography and Marine Biology, 32, 241–304.

Baines, P. G. (1973). The generation of internal tides by fiat-bump topography, 20(February 1972), 179–205.

Baines, P. G. (1982). On internal tide generation models. *Deep-Sea Res. A,* 29, 307–338.

Baker, P., Roobol, M., McReath, M., Harvey, M., Davies, T. (1975). The geology of the South« Shetland Islands. Volcanic evolution of Deception Island: Introduction. British Antarctic Survey. British Antarctic Survey, Scientific Reports, vol. 78, pp. 3–15.

Baraldo, A., Rinaldi, C.A. (2000), Stratigraphy and structure of Deception Island, South Shetland Islands, Antarctica, Journal of South American Earth Sciences 13(2000) 785-796.

Baraldo, A., Rapalini, A. E., Bohnel, H. & Mena, M. (2003). Paleomagnetic study of Deception Island, South Shetland Islands, Antarctica. Geophysical Journal International, 153, 1–11.

Barbosa, A., Benzal, J., De León, A., & Moreno, J. (2012). Population decline of chinstrap penguins (Pygoscelis antarctica) on Deception Island, South Shetlands, Antarctica. Polar Biology, 35(9), 1453–1457.

Barclay, a. H., Wilcock, W. S. D. & Ibáñez, J. M. (2009). Bathymetric constraints on the tectonic and volcanic evolution of Deception Island Volcano, South Shetland Islands. *Antarctic Science*, 21(02), p.154-163.

Bargagli, R. (2000). Trace metals in Antarctica related to climate change and increasing human impact. Rev. Environ. Contam. Toxicol. 166, 129–173.

Barnes, D. K. A. (2000). Diversity, recruitment and competition on island shores at south polar localities compared with lower latitudes: encrusting community examples. Hydrobiologia, 440, 37–44.

Barnes, D. K. A., Linse, K., Enderlein, P., Smale, D. A. N., Fraser, K. P. P., & Brown, M. (2008). Marine richnes and gradients at Deception Island , Antarctica, 20(3), 271–279.

Basberg, B. L., & Headland, R. K. (2008). Discussion paper The 19th Century Antarctic Sealing Industry . Sources , Data and Economic Significance, (September).

Bernardes, B. (2007). Hydrodynamical and Ecological Modelling of the North Sea Dissertação para obtenção do Grau de Mestre em Engenharia do Ambiente. Instituto Superior Técnico, Universidade Técnica de Lisboa.

Bícego, M. C., Zanardi-Lamardo, E., Taniguchi, S., Martins, C. C., da Silva, D. A. M., Sasaki, S. T., Albergaria-Barbosa, A. C. R., Paolo, F. S., Weber, R. R., Montone, R. C., (2009). Results from a 15-year study on hydrocarbon concentrations in water and sediment from Admiralty Bay, King George Island, Antarctica. Antarctic Science. 21, 209–220.

Braunschweig, F., Leitao, P. C., Fernandes, L., Pina, P., Neves. (2002). The object oriented design of the integrated Water Modelling System, 1–12.

Cardoso, N. K. R., Souza, R. B., Comin, A. (2013). Avaliação do modelo WRF em relação à temperatura do ar e pressão atmosférica devido à passagem de uma frente fria sobre a Ilha Deception, Antárctica, Revista Ciência e Natura, Santa Maria, Edição especial, Dez.2013, 356-358.

Clapperton, C.M., (1969). The volcanic eruption at Deception Island, December 1967. British Antarctic Survey Bulletin 22, 83–90.

Coelho, H. S., Neves, R. R., Leitão, P. C., Martins, H. & Santos, A. P. (1999). The slope current along the western European margin: A numerical investigation. Boletin Instituto Espanol de Oceanografia. 15, 1998, pp. 61-72.

Coelho, A. H. H., Souza, R. B. (2011). Análise de Séries de tempo de dados meteo-oceanográficos na Ilha de Deception durante a operação Antártica 29.

Comin, A. N., Acevedo, O. C., Souza, R. B. (2012). Comparison Between in situ Thermodynamic Parameters and the WRF Model in high resolution out in Deception Island, Antarctica. Climate change, Impacts and Vulnerabilities in Brazil: Preparing the Brazilian Northeast for the future.

Comin, A. N. (2012). Sensibilidade às parametrizações físicas do Wrf nas previsões dos parâmetros atmosféricos em Shetland do Sul e Deception. Dissertação de Mestrado inserida no programa de pós-graduação em meteorologia, Centro de Ciências Naturais e Exatas, Universidade Federal de Santa Maria.

Craig, P. D. (1987). Solutions for the internal tide generation over coastal topography. *J. Mar. Res.,* 45, 83–105.

Cranmer, T. L., Ruhl, H. A., Baldwin, R. J. & Kaufmann, R. S. (2003). Spatial and temporal variation in the abundance, distribution and population structure of epibenthic megafauna in Port Foster, Deception Island. Deep-Sea Research II, 50, 1821–1842.

Curtosi, A., Pelletier, E., Vodopidez, C. L., Mac Cormack, W. P. (2007). Polycyclic aromatic hydrocarbons in soil and surface marine sediment near Jubany Station (Antarctica). Role of permafrost as low-permeability barrier. Sci. Total Environ. 383, 193–204.

Cushman-Roisin, B. (1996). Lower and Upper Bounds on Internal-Wave Frequencies in Stratified Rotating Fluids. Physical Review Letters, 77(24), 4903–4905.

Dayton, P. K. (1990). Polar benthos. In SMITH,W.O., ed. Polar oceanography. San Diego, CA: Academic Press, 631–685.

Deception Island Management Package (2015). Management Plan for Antarctic Specially Managed Area No .4 Deception Island , South Shetland Islands , Antarctica, (4), 1–13.

Decyk, V. K., Norton, C. D., Szymanski, B. K. (1997). "Expressing Object-Oriented Concepts in Fortran90", in ACM Fortran Forum.

Deheyn, D. D., Gendreau, P., Baldwin, R. J., Latz, M. I. (2005). Evidence for enhanced bioavailability of trace elements in the marine ecosystem of Deception Island, a volcano in Antarctica. Mar. Environ. Res. 60, 1–33.

Dibbern, J.Stephen. (2009). Fur Seals, whales and tourists: a commercial history of Deception Island, Antarctica, Polar Record, 46 (03), 210-21.

Dragani, W.C., Drabble, M.R., D'Onofrio, E.E & Mazio, C.A. (2014). Propagation and amplification of tide at the Bransfield and Gerlache straits, northwestern Antarctic Peninsula. Polar Geoscience, 17, 156–170.

Fernandes, R. (2005). Modelação Operacional no Estuário do Tejo. Dissertação para obtenção do grau de Mestre em Ecologia, Gestão e Modelação dos Recursos Marinhos, Instituto Superior Técnico, Universidade Técnica de Lisboa.

Foster, T. D., Foldvik, A., Middleton, J. H. (1987). Mixing and bottom water formation in the shelf break region of the southern Weddell Sea, Deep Sea Res., Part A, 34, 1771-1794.

Galindo-Zaldívar J., A. Jabaloy, A. Maldonado and C. Sanz de Galdeano (1996), Continental fragmentation along the South Scotia Ridge transcurrent plate boundary (NE Antarctic Peninsula), Tectonophysics, 259, 275-301.

Gallardo, V.A. & Castillo, J.G. (1968). Mass mortality in the benthic fauna of Port Foster resulting from the eruptions in Deception Island, (South Shetland Islands). Publicaciones Instituto Antartico Chileno, 16, 1–11.

Gallardo, V.A. & Castillo, J.G. (1970). Quantitative observations on the benthic macrofauna of Port Foster (Deception Island) and Chile Bay. (Greenwich Island). In HOLDGATE, M.W., ed. Antarctic ecology. London: Academic Press, 242–243.

Gallardo, V.A., Castillo, J.G., Retamal, M.A., Hermosilla, J. & Trucco, R. (1975). Benthic community studies in the South Shetland Islands. Antarctic Journal of the United States, 10(4), 135.

Gallardo, V.A., Castillo, J.G., Retamal, M.A. & Yanes, A. (1977). Quantitative studies on the soft-bottom macrobenthic animal communities of shallow Antarctic bays. In LLANO, G.A., ed. Adaptations within Antarctic ecosystems. Washington, DC: Smithsonian Institution, 361–387.

Glatts, R.C., Uhlman, A.H., Smith Jr., K.L., Baldwin, R.J. (2003). Long time-series monitoring of the ecosystem at Deception Island, Antarctica: description of instrumentation. Deep-Sea Research II.

González-Casado, J.M., J.L. Giner-Robles & J. López-Martínez (2000), Bransfield Basin, Antarctic Peninsula: not a normal backarc basin, Geology, 28, 1043-1046.

Gray, S.C., Sturz, A., Bruns, M., Marzan, R., Dougherty, D., Law, H., Brackett, J., Marcou, M. (2003). Composition and distribution of sediments and benthic foraminifera in a submerged caldera after 30 year of volcanic quiescence. Deep-Sea Research II.

Guerra, R., Fetter, E., Ceschim, L. M. M., Martins, C. C. (2011). Trace metals in sediment cores from Deception and Penguin Islands (South Shetland Islands, Antarctica). Mar. Pollut. Bull. 62, 2571–2575.

Hawkes, D. D. (1961), The geology of the South Shetland Islands: II. The geology and petrology of Deception Island, Falkland Islands Dependencies Survey Scientific Reports, No. 27, p.43.

Helland-Hansen, B., Nansen, F. (1909). The Norwegian Sea. Norw. Fish Mar. Invest. Rep. 2, (1), (2), 87-132.

Jerez, S., Motas, M., Palacios, M. J., Valera, F., Cuervo, J. J., Barbosa, A. (2011). Concentration of trace elements in feathers of three Antarctic penguins: geographical and interspecific differences.

Jerez, S., Motas, M., Benzal, J., Diaz, J., & Barbosa, A. (2013). Monitoring trace elements in Antarctic penguin chicks from South Shetland Islands, Antarctica. Marine Pollution Bulletin, 69(1-2), 67–75.

Jigena, B., Vidal, J., & Berrocoso, M. (2014). Determination of the mean sea level at Deception and Livingston islands, Antarctica. *Antarctic Science*, *27*(01), 101–102.

Jigena-Antelo, B., Vidal, J., & Berrocoso, M. (2015). Determination of the tide constituents at Livingston and Deception Islands (South Shetland Islands, Antarctica), using annual time series. Dyna, 82(191), 209–218.

Kaufmann, R.S., Fisher, E.C., Gill, W.H., King, A.L., Laubacher, M., Sullivan, B. (2003). Temporal patterns in the distribution, biomass and community structure of macrozooplankton and micronekton within Port Foster, Deception Island, Antarctica. Deep-Sea Research II, this issue (doi: 10.1016/S0967-0645(03)00092-4).

Kendall, K. A., Ruhl, H. A., & Wilson, R. C. (2003). Distribution and abundance of marine bird and pinniped populations within Port Foster, Deception Island, Antarctica. Deep Sea Research Part II: Topical Studies in Oceanography, 50(10-11), 1873–1888.

Kundu, P. K., Cohen, I.M., (2004). Fluid Mechanics Third Edition, Academic Press, 622-624.

Leendertsee, J., Liu, S. (1978). "A three-dimensional turbulent energy model for non-homogeneous estuaries and coastal sea systems", in: Nihoul J. (Eds.), Hydrodynamics of Estuaries and Fjords, Elsevier, Amsterdam, 387-405.

Leitão, P.C. (1996). "Modelo de dispersao lagrangeano tridimensional", Dissertacao para a obtencao do grau de Mestre em Ecologia, Gestao e Modelacao de Recursos Marinhos, Instituto Superior Tecnico, Lisboa.

Leitão, P. (2003). *Integração de Escalas e de processos na Modelação do Ambiente Marinho.* Tese de Doutoramento. Instituto Superior Técnico, Universidade Técnica de Lisboa.

Lenn, Y.-D., T. K. Chereskin, and R. C. Glatts. (2003). Seasonal to tidal variability in currents, stratification, and acoustic backscatter in an Antarctic ecosystem at Deception Island. Deep-Sea Res. II, 50, 1665-1684.

Levine, M. D., Padman, L., Muench, R. D., Morison, J. H. (1997). Internal waves and tides in the western Weddell Sea: Observations from Ice Station Weddell. Journal of Geophysical Research, Vol. 102(C1), 1073-1089.

Lim, H., Han, M., Seo, D., Kim, J., Lee, J., Park, H., Hur, J.-S., Cheong, Y., Heo, J., Yoon, H., Cho, J.-S. (2009). Heavy metal concentrations in the fruticose lichen usnea aurantiacoatra from King George Island, South Shetland Islands, West Antarctica. J. Korean Soc. Appl. Biol. Chem. 52, 503–508.

López-Martínez, J. & Serrano, E. (2002), Geomorphology of Deception Island. In López-Martínez, J., Smellie, J.L., Thomson, J.W. & Thomson, M.R.A. Eds. Geology and Geomorphology of Deception Island, 31-39. BAS Geomap Series, Sheets 6-A and 6-B. Cambridge: British Antarctic Survey.

Lovell, L. L. & Trego, K. D. (2003). The epibenthic megafaunal and benthic infaunal invertebrates of Port Foster, Deception Island (South Shetland Islands Antarctica). Deep-Sea Research II, 50, 1799–1819.

Lu, Z., Cai, M., Wang, J., Yang, H., He, J. (2012). Baseline values for metals in soils on Fildes Peninsula, King George Island, Antarctica: the extent of anthropogenic pollution. Environ. Monit. Assess. 184, 7013 – 7021.

Mão de Ferro, A. (2012), Fontes, transporte e especiação de elementos traço nos compartimentos ambientais da ilha Deception, Antártida. Msc Thesis in Environmental Engineering, Instituto Superior Técnico, Universidade Técnica de Lisboa.

Mão de Ferro, A., Mota, A. M., & Canário, J. (2013). Sources and transport of As, Cu, Cd and Pb in the environmental compartments of Deception Island, Antarctica. *Marine Pollution Bulletin*, *77* (1-2), 341 – 8.

Martí, J., Baraldo, A. (1990). Precaldera pyroclastic deposits of Deception Island (South Shetland Islands). Antarctic Science 2, 345–352.

MOHID Modelling System Description.

Molina, A., Pablo, M. A. De, & Ramos, M. (2013). 44th Lunar and Planetary Science Conference (2013) 44th Lunar and Planetary Science Conference (2013) (pp. 2–3).

Padman, L., Plueddemann, A. J., Muench, R. D., Pinkel, R. (1992). Diurnal tides near the Yermak Plateau, J. Geophys. Res., 97, 12,639-12,652.

Padman, L. (1995). Small-scale processes in the Arctic Ocean, in Arctic Oceanography: Marginal Ice Zones and Continental Shelves, Coastal and Estuarine Stud., vol. 49, edited by W.O. Smith Jr. and J.M. Grebmeier, pp. 97-129, AGU, Washington, D.C.

Pereira, A. F., Castro, B. M. (2007). Internal Tides in the Southwestern Atlantic off Brazil: Observations and Numerical Modelling. Journal of physical oceanography, 37, 1512-1517.

Pérez-López, R., Giner-Robles, J. L., Martínez-Díaz, J. J., Rodríguez-Pascua, M. A., Bejar, M., Paredes, C., and González-Casado, J. M. (2007). Active tectonics on Deception Island (West-Antarctica): A new approach by using the fractal anisotropy of lineaments, fault slip measurements and the caldera collapse shape, in Antarctica: A Keystone in a Changing World – Online Proceedings of the 10th ISAES, edited by A.K. Cooper and C.R. Raymond et al., USGS Open-File Report 2007-1047, Short Research Paper 086.

Purser, R. J., Leslie, L. M. (1988). A Semi-Implicit, Semi-Lagrangian Finite-Difference Scheme Using High-Order Spatial Differencing on a Nonstaggered Grid. 1988 American Meteorological Society, 1-12.

Retamal, M.A., Quintana, R. & Neira, F. (1982). Analisis cuali y cuantitativo de las comunidades bentonicas en Bahy´a Foster (Isla Decepcion) (XXXV Expedicion Antartica Chilena, enero 1981. Publication Instituto Antarctico Chileno Series Cientica, 29, 5–15.

Rey, J., Somoza, L., Martínez-Frías, J. (1995). Tectonic, volcanic, and hydrothermal event sequence on Deception Island (Antarctica). Geo-Marine Letters 15, 1–8.

Ribeiro, A. P., Figueira, R. C. L., Martins, C. C., Silva, C. R. A., França, E. J., Bícego, M. C., Mahiques, M. M., Montone, R. C. (2011). Arsenic and trace metal contents is sediment profiles from Admiralty Bay, King George Island, Antarctica. Mar. Pollut. Bull. 62, 192 – 196.

Ribeiro, A. P., Figueira, R. C. L., Martins, C. C., Silva, C. R. A., França, E. J., Bícego, M. C., Mahiques, M. M., Montone, R. C. (2011). Arsenic and trace metal contents is sediment profiles from Admiralty Bay, King George Island, Antarctica. Mar. Pollut. Bull. 62, 192 – 196.

Roobol, M. J. (1982). The volcanic hazard at Deception Island, South Shetland Islands. British Antarctic Survey Bulletin 51, 237–245.

Ruhl, H. A., Hastings, P. A., Zarubick, L. A., Jensen, R. M., & Zdzitowiecki, K. (2003). Fish populations of Port Foster, Deception Island, Antarctica and vicinity. *Deep Sea Research Part II: Topical Studies in Oceanography*, *50*(10-11), 1843–1858.

Santini, M. F., Souza, R. B., Stech, J. L., Souza, A. F. (2012). Interception: Monitoramento Meteo-Oceanográfico na Ilha Deception, Antártica, Edital 023 do CNPq/Proantar.

Santos, I. R., Silva-Filho, E. V., Schaefer, C. E., Albuquerque-Filho, M. R., Campos, L. S. (2005). Heavy metal contamination in coastal sediments and soils near the Brazilian Antarctic Station, King George Island. Mar. Pollut. Bull. 50, 185–194.

Smellie, J. L. (1988). Recent observations on the volcanic history of Deception Island, South Shetland Islands. *British Antarctic Survey Bulletin,* No. 81, 83-85.

Smellie, J. L. (1989). Deception Island. In: Dalziel, I. W. D. (ed.) Tectonics of the Scotia Arc, Antarctica. 28th International Geological Congress, Field Trip Guide Book. American Geophysical Union, Washington, DC, T180, 146–152.

Smellie, J. .L., López-Martínez, J., Rey, J. & Serrano, E. (1997). Geological and geomorphological maps of Deception Island, South Shetland Islands. In Rrccl, C.A., ed. TheAntarcticregion:geologrcal evolution and processes. Siena: Terra Antarctica Publications, 1195-1 198.

Smellie, J. L. (2001), Lithostratigraphy and volcanic evolution of Deception Island, South Shetland Islands. Antarctic Science, 13, p. 188–209.

Smellie, J. L. (2002). Geology. In: López-Martínez, J., Smellie, J.L., Thomson, J.W. & Thomson, M.R.A. Eds. Geology and Geomorphology of Deception Island, 11-30. BAS Geomap Series, Sheets 6-A and 6-B. Cambridge: British Antarctic Survey.

Smith Jr., K.L., Baldwin, R.J., Glatts, R.C., Chereskin, T.K., Ruhl, H.A., Lagun, V. (2003a). Weather, ice and snow conditions at Deception Island, Antarctica: long time series photographic monitoring. Deep-Sea Research II.

Smith Jr., K.L., Baldwin, R.J., Kaufmann, R.S., Sturz, A. (2003b). Ecosystem studies at Deception Island, Antarctica: an overview. Deep-Sea Research II.

Sturz, A. A., Gray, S. C., Dykes, K., King, A., Radtke, J. (2003). Seasonal changes of dissolved nutrients within and around Port Foster, Deception Island, Antarctica. Deep-Sea Research II, 50, 1685-1705.

Torrecillas, C. L., Berrocoso, D., Manuel, G. G., Alicia. (2006). The Multidisciplinary Scientific Information Support System(SIMAC) for Deception Island. Vol. XXVIII. Pag. 397-402. En: Antarctica: Contributions to Global Earth Sciences. Berlín, Alemania, Springer.

Torrecillas, C., Berrocoso, M., Pérez-López, R., & Torrecillas, M. D. (2012). Determination of volumetric variations and coastal changes due to historical volcanic eruptions using historical maps and remote-sensing at Deception Island (West-Antarctica). Geomorphology, 136(1), 6–14.

Trancoso, A. R., Saraiva, S., Fernandes, L., Pina, P., Leitão, P., Neves, R. (2005). Modelling macroalgae using a 3D hydrodynamic-ecological model in a shallow, temperate estuary. Ecological Modelling. 187, 2005, pp. 232–246.

Valencio, D. A., Mendia, J. E. & Vilas, J. F. (1979). Paleomagnetism and K–Arage of Mesozoic and Cenozoic igneous rocks from Antarctica. Earth and Planetary Science Letters, 45, 61–68.

Vaz, N., Dias, J. M., Leitão, P., Martins, I. (2005). Horizontal patterns of water temperature and salinity in an estuarine tidal channel: Ria de Aveiro. Ocean Dynamics. 2005, Vol. 55, pp. 416-429.

Vidal, J., Berrocoso, M., & Fernandez, A. (2010). Study of the tide in Deception and Livingston Islands (Antarctica). *Antarctic Science*, in press, 2010.

Vidal, J., Berrocoso, M., & Jigena, B. (2011). Hydrodynamic modelling of Port Foster, Deception Island (Antarctica).

Vidal, J., Berrocoso, M., & Ferna, A. (2012). Study of tides and sea levels at Deception and Livingston islands, Antarctica, 24(2), 193–201.

Vila, J., Ortiz, R., Correig, A. M., Garcia, A. (1992). Seismic activity on Deception Island, Terra Scientific Publishing Company, 449-56.

Annex

Annex A – Tide data file.

Tide.dat – File:

```
<begingauge>
NAME                       : NOVOPONTO
LONGITUDE                  : -60.0000 31.0000 48.0000
LATITUDE                   : -63.0000 0.000000 10.0000
METRIC_X                   : -60.5301
METRIC_Y                   : -63.0028
REF_LEVEL                  : 2.08000
TIME_REF                   : 0.000000
M2                         : 0.372007       -79.8200
S2                         : 0.217256       -13.5350
K1                         : 0.259546        62.0689
K2                         : 0.0504443      -14.9101
N2                         : 0.0431709      -107.238
2N2                        : 0.00243790      107.429
O1                         : 0.273164        48.0596
Q1                         : 0.0858477       61.8871
P1                         : 0.0605343       35.7315
M4                         : 0.000000        0.000000
Mf                         : 0.0228681      -160.102
Mm                         : 0.0124503      -170.390
Mtm                        : 0.00389392     -149.979
MSqm                       : 0.000530146    -151.472
<endgauge>
```

WaterProperties.dat – File:

```
OUTPUT_TIME               : 0 3600
TIME_SERIE                : 1
TIME_SERIE_LOCATION       : D:\...\TimeSeriesLoca.dat

<beginproperty>
DATA_ASSIMILATION         : 0
NAME                      : temperature
UNITS                     : ºC
DESCRIPTION               : Temperature profile at Neptune's Bellow.
FILE_IN_TIME              : NONE
INITIALIZATION_METHOD     : ASCII_FILE
FILENAME                  : D:\...\Tsummer-Final.dat
DEFAULTVALUE              : 1.5
REMAIN_CONSTANT           : 1
DISCHARGES                : 0
SURFACE_FLUXES            : 0
ADVECTION_DIFFUSION       : 0
!Null gradient = 4
BOUNDARY_CONDITION        : 4
OUTPUT_HDF                : 1
TIME_SERIE                : 1
<endproperty>

<beginproperty>
DATA_ASSIMILATION         : 0
NAME                      : salinity
UNITS                     : psu
DESCRIPTION               : Salinity Profile at Neptune's Bellow.
FILE_IN_TIME              : NONE
INITIALIZATION_METHOD     : ASCII_FILE
FILENAME                  : D:\...\SalinitySummer.dat
DEFAULTVALUE              : 34.4
REMAIN_CONSTANT           : 1
DISCHARGES                : 0
SURFACE_FLUXES            : 0
ADVECTION_DIFFUSION       : 0
!Null gradient = 4
BOUNDARY_CONDITION        : 4
OUTPUT_HDF                : 1
TIME_SERIE                : 1
<endproperty>
```

Annex C – Temperature and salinity profiles applied in the 3D model.

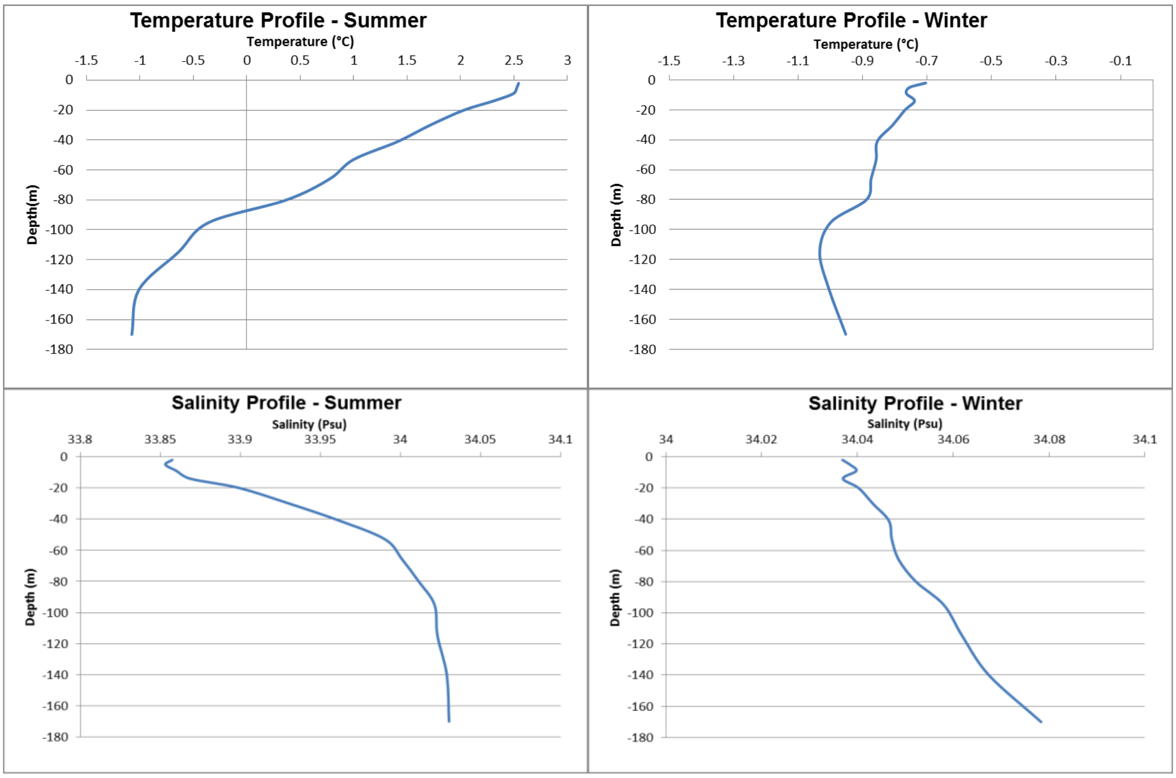

Figure 51 - T-S profiles applied inside Port Foster.

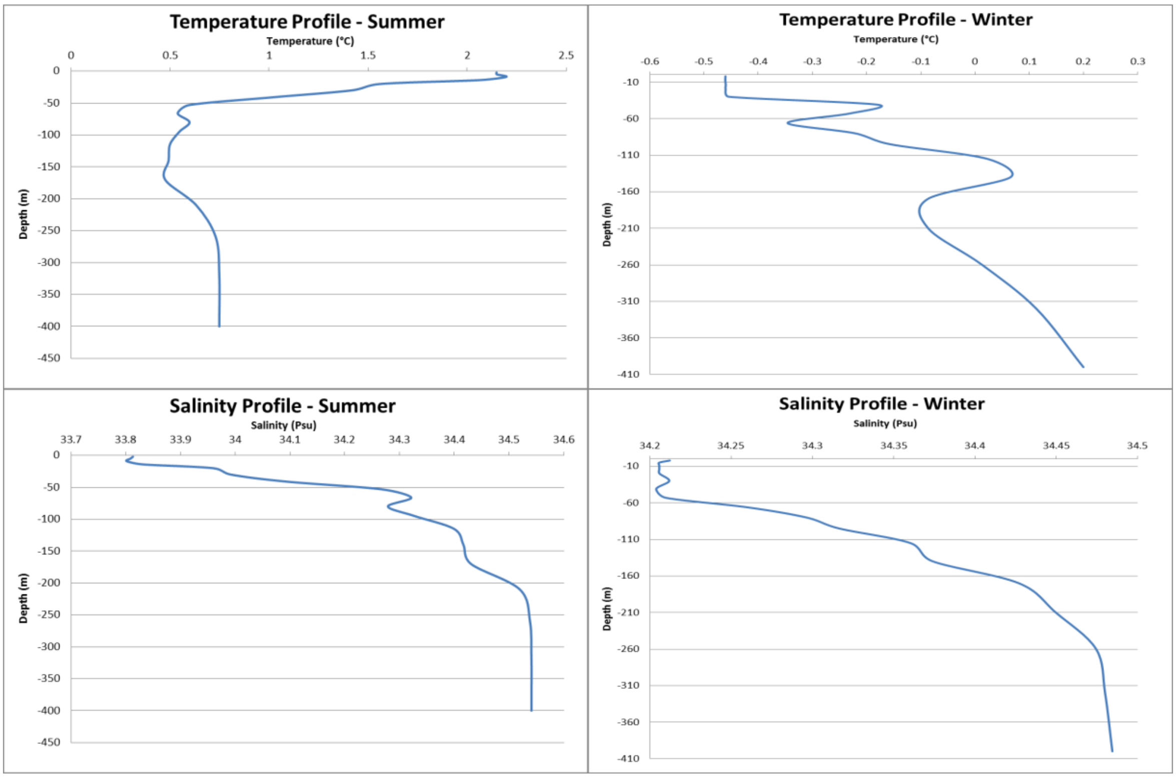

Figure 52 - T-S profiles applied outside Port Foster.

Annex D – Output for 1 month tidal velocity for both seasons in Neptune’s Bellows and colatina.

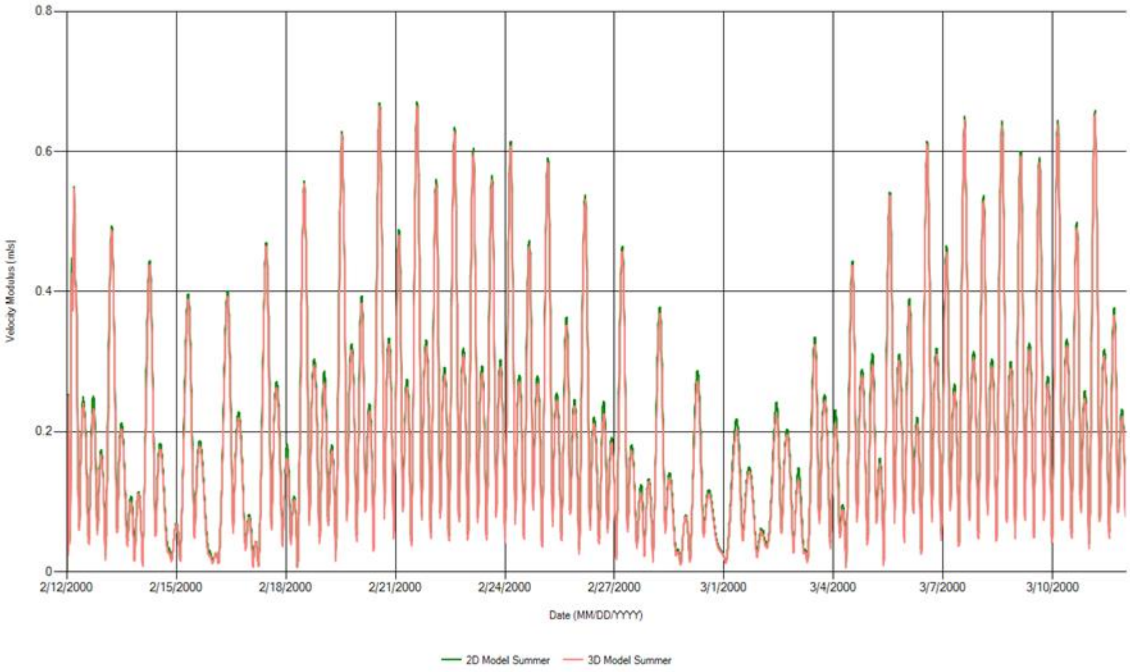

Figure 53 - Summer: 1 month tidal velocity simulation for both models in Neptune’s Bellows.

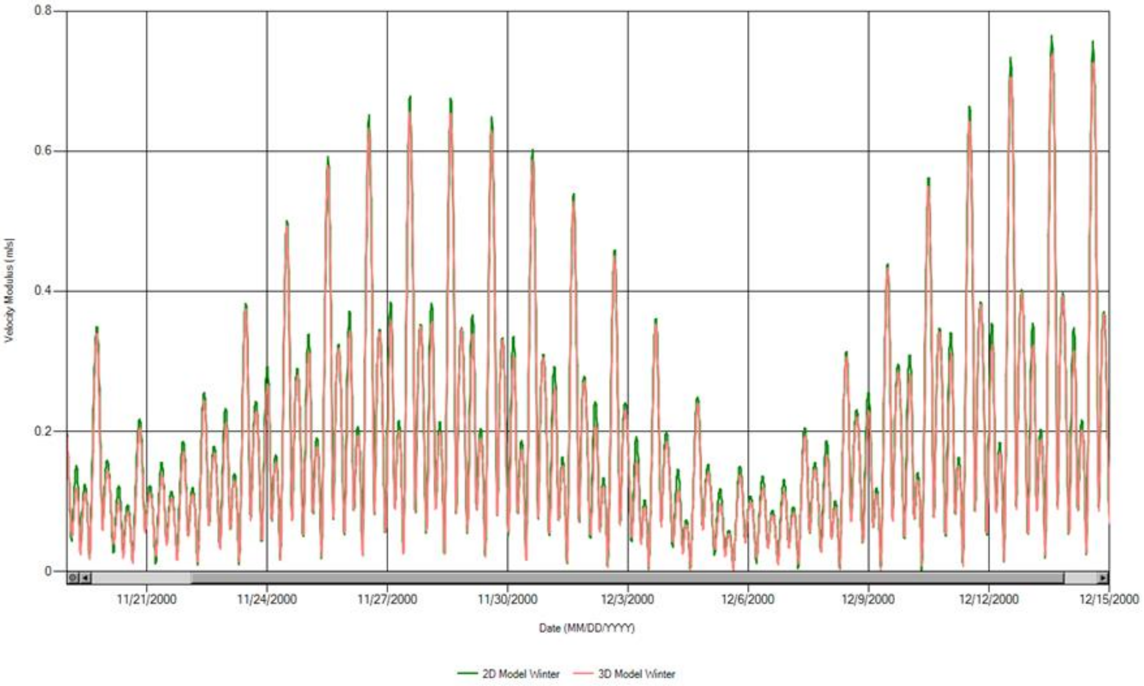

Figure 54 - Winter: 1 month tidal velocity simulation for both models in Neptune’s Bellows.

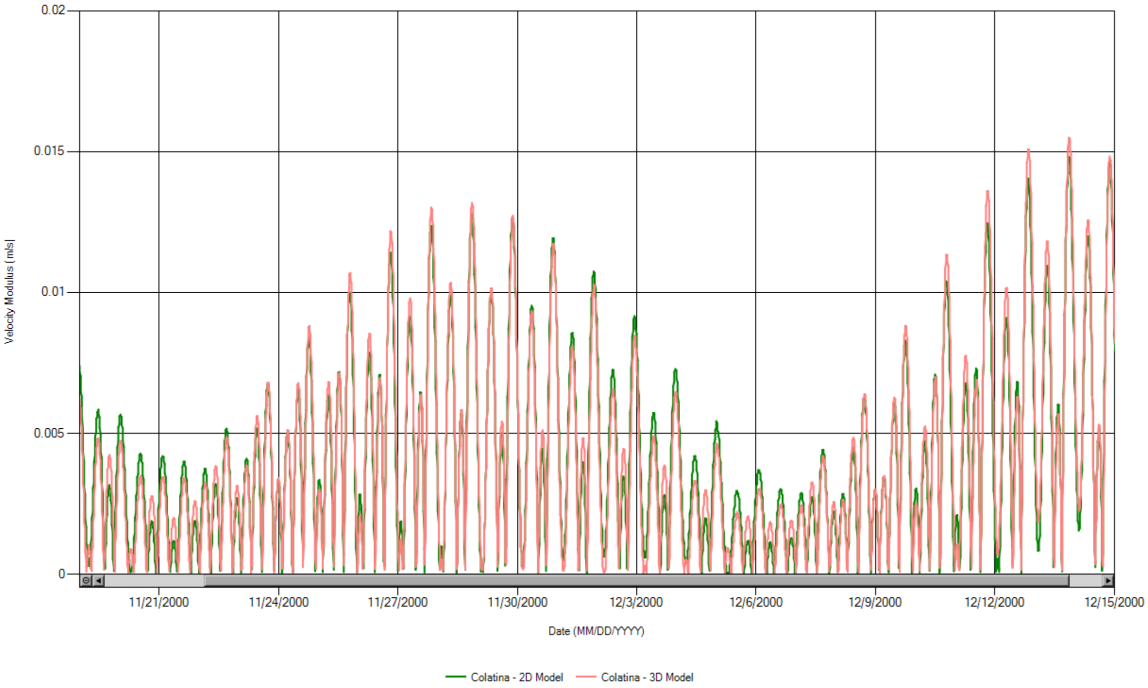

Figure 55 - Winter: 1 month tidal velocity simulation for both models in Colatina.

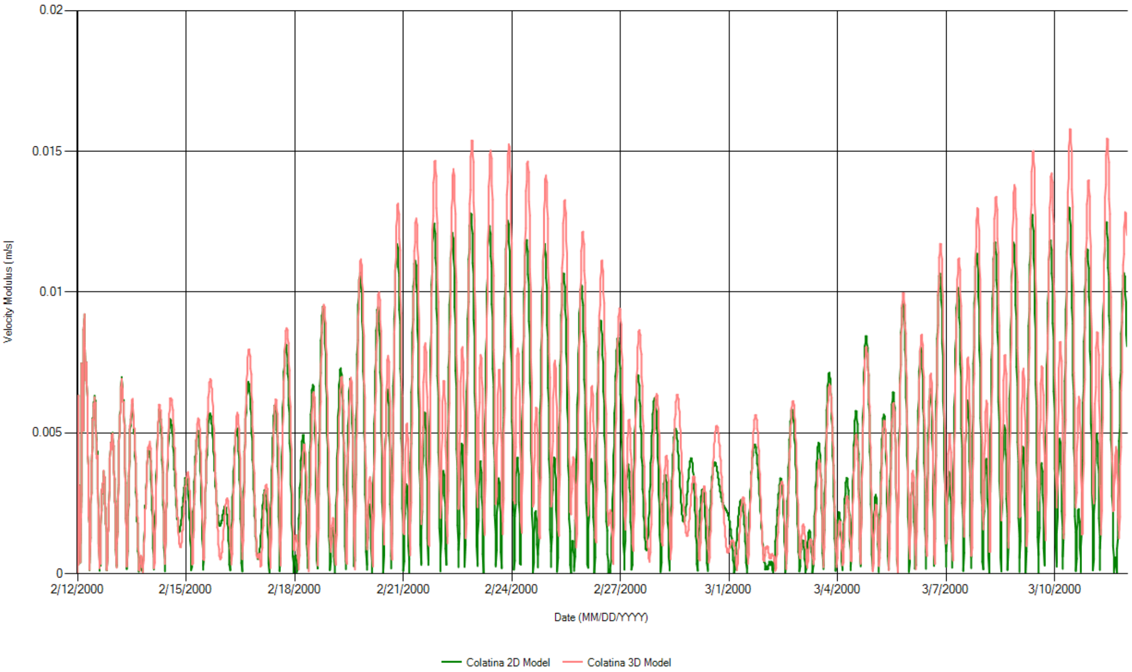

Figure 56 - Summer: 1 month tidal velocity simulation for both models in Colatina.

Annex E – T_tide output.

Table 5 – T_tide Output: Neptune’s Bellows tidal components.

tide	freq(cph)	amp	amp_err	pha	pha_err	snr	**P(Hour)**
MSF	0.002822	0.0003	0	80.38	115.7	0.36	354.3711
*2Q1	0.035706	0.001	0.001	183.62	29.79	3.8	28.0062
*Q1	0.037219	0.0846	0.001	64.73	0.37	1.90E+04	26.8684
*O1	0.038731	0.2738	0.001	49.06	0.11	2.40E+05	25.8193
*NO1	0.040269	0.0079	0.001	321.83	3.51	2.30E+02	24.8332
*K1	0.041781	0.3113	0.001	68.14	0.1	2.20E+05	23.9345
*J1	0.043293	0.0061	0.001	22.55	5.71	1.10E+02	23.0985
*OO1	0.044831	0.0013	0	27.47	26.01	7.3	22.3061
UPS1	0.046343	0.0003	0	122.61	97.55	0.43	21.5782
*N2	0.078999	0.0429	0.001	253.44	0.74	4.70E+03	12.6584
*M2	0.080511	0.3719	0.001	281.44	0.09	4.40E+05	12.4206
*S2	0.083333	0.206	0.001	359.98	0.16	1.30E+05	12.0000
*ETA2	0.085074	0.0045	0.001	96.55	7.37	54	11.7545
*MO3	0.119242	0.0009	0.001	229.13	31.43	3	8.3863
M3	0.120767	0.0006	0.001	92.22	61.95	0.96	8.2804
MK3	0.122292	0.0004	0.001	347.18	86.26	0.61	8.1771
*SK3	0.125114	0.0007	0.001	12.95	53.23	1.2	7.9927
MN4	0.159511	0.0003	0	348	108.49	0.37	6.2698
M4	0.161023	0.0002	0	340.8	121.69	0.29	6.2103
MS4	0.163845	0.0005	0.001	249.69	65.22	0.9	6.1033
S4	0.166667	0.0005	0.001	287.79	74.7	0.91	5.9999
2MK5	0.202804	0.0005	0.001	238.24	62	0.81	4.9309
2SK5	0.208447	0.0001	0	67.44	173.47	0.14	4.7974
2MN6	0.240022	0.0002	0	29.43	140.11	0.27	4.1663
*M6	0.241534	0.0005	0	61.79	54.78	1.3	4.1402
*2MS6	0.244356	0.001	0.001	141.49	29.19	3.3	4.0924
*2SM6	0.247178	0.0007	0.001	222.49	51.71	1.3	4.0457
3MK7	0.283315	0.0002	0	56.41	151.29	0.19	3.5296
M8	0.322046	0.0001	0	195.22	165.64	0.15	3.1056

Annex F – Lagrangean Tracers Output Sample.

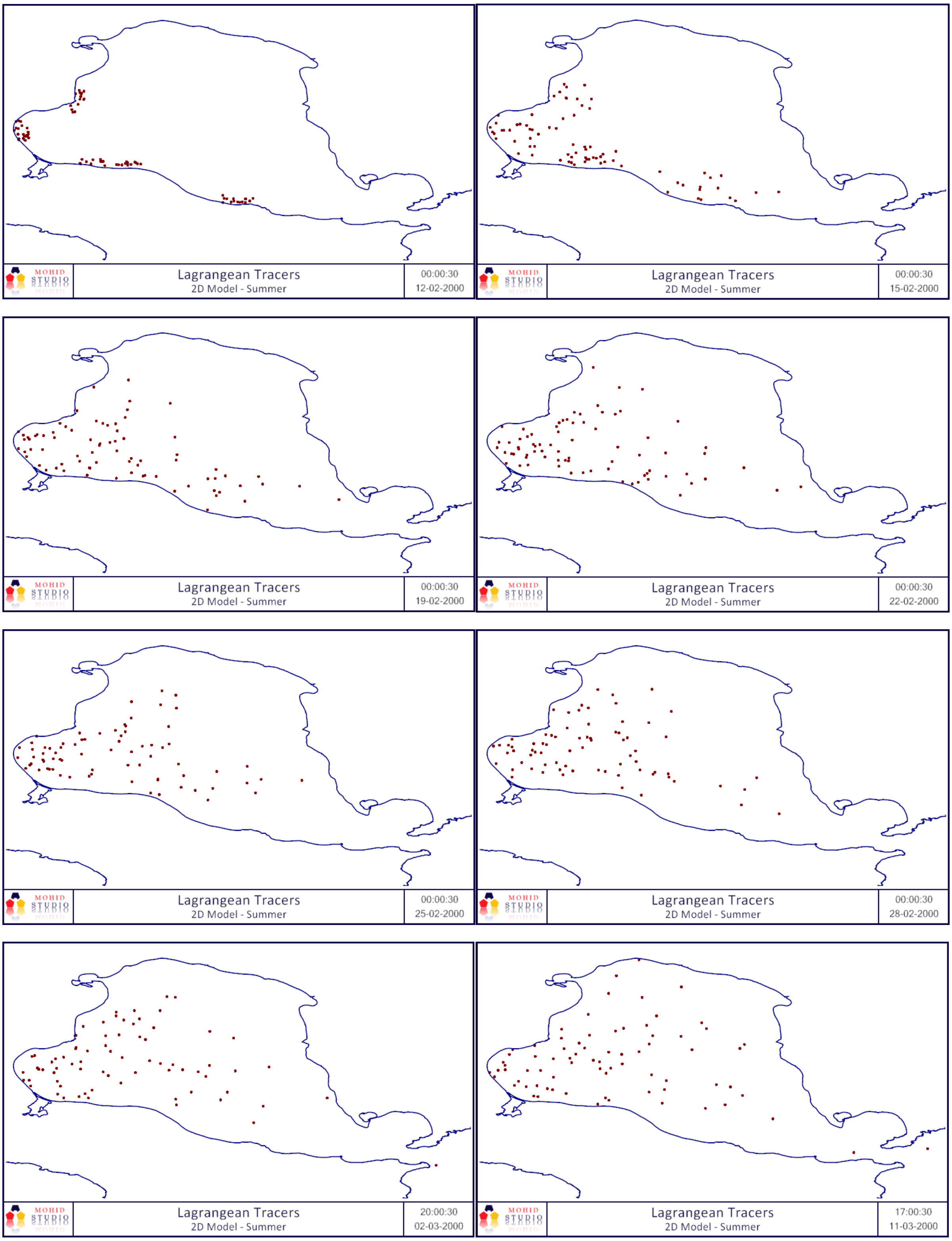

Figure 57 – Lagrangean Tracers output representation for 1 month of simulation.